

# **Single-dish polarimetry using a software-based polarization spectrometer**

March, 2015

Izumi Mizuno



## Nobeyama 45m radio telescope

Supervisor: Hiroyuki Nakanishi

Seiji Kameno

Masao Saito

Nario Kuno

A Ph.D. Dissertation Presented to  
Graduate School of Science and Engineering,  
School of Natural Science,  
Kagoshima University

---

This research was supported by  
Nobeyama radio observatory of Japan



## *Abstract*

This thesis mainly addresses the development of the software Polarization Spectrometer, PolariS and the optimization of the polarization calibration procedure to detect the Zeeman splitting of a CCS molecular emission line for magnetic field measurement toward pre star-forming cores. The magnetic field is a key parameter to understand the star-formation process with gravitational core collapse. There exists insufficient accumulation of reliable measurements of magnetic fields to date. For a gravitationally balanced magnetic field strength of  $100 \mu\text{G}$ , we expect the Zeeman shift of  $\sim 64\text{Hz}$  between two orthogonal circular polarizations. Hence our science goal is to detect the Zeeman split of the CCS molecular line at an accuracy of 12 Hz which corresponds to  $5\sigma$  for  $100 \mu\text{G}$ . Our science goal requires extremely accurate measurements of the Stokes V spectrum. To reduce systematic errors in Stokes V, we have built the Z45 receiver that is operational for dual linear polarization and the software-based polarization spectrometer, PolariS. PolariS offers an extremely high frequency resolution of 61 Hz for full-Stokes spectra to accommodate the required Zeeman shift of 64 Hz. We have installed these polarimetry devices on the Nobeyama 45-m radio telescope for commissioning and science observations. We verified instrumental configuration using SiO maser observations and we estimated instrumental polarization caused by D-term and an instrumental phase using unpolarized source and artificial linearly polarized source. Finally, we attempted to measure the Zeeman split of the CCS emission line toward a pre star-forming core in the Taurus Molecular Cloud-1 with a best accuracy of 35.4 Hz within a telescope time of only 7 hours. Thus we estimate that an observation time of 54 hours is necessary to achieve our science goal.

# Contents

<b>Contents</b>	iii
<b>List of Figures</b>	vi
<b>List of Tables</b>	viii
<b>Symbols</b>	ix
<b>1 Introduction</b>	1
1.1 Overview of star formation . . . . .	1
1.2 Theoretical models of star formation . . . . .	2
1.2.1 Magnetic-field-driven star formation (strong magnetic field) . . . . .	2
1.2.2 Turbulence-driven star formation (weak magnetic field) . . . . .	2
1.2.3 Magnetic-field- and turbulence-driven star formation . . . . .	3
1.2.4 Method for constraining these models . . . . .	3
1.3 Estimation method of the Zeeman effect . . . . .	3
1.4 Observational results of Zeeman splitting measurement . . . . .	4
1.5 Our research aim and the outline of this thesis . . . . .	6
<b>2 Stokes parameters—Polarization description</b>	8
2.1 Electromagnetic waves . . . . .	8
2.1.1 Expression of a wave properties . . . . .	10
2.2 Polarization radiation . . . . .	10
2.2.1 Linear polarization . . . . .	11
2.2.2 Circular polarization . . . . .	11
2.2.3 Elliptical polarization . . . . .	12
2.3 Stokes parameter . . . . .	13
2.3.1 Monochromatic wave . . . . .	13
2.3.2 Quasi-monochromatic waves . . . . .	16
<b>3 Measurement of circular polarization</b>	18
3.1 Introduction . . . . .	18
3.2 Polarimetry device . . . . .	18
3.3 Instrumental effects through signal processing . . . . .	19
3.3.1 Phase difference . . . . .	19
3.3.2 D-term . . . . .	20
3.4 Estimation of an antenna temperature of a radio source . . . . .	21
3.4.1 Antenna temperature . . . . .	22

3.4.2	Measurement of antenna temperature of a radio source . . . . .	24
3.5	Relation of receiving methods and Stokes V measurement accuracy . . . . .	26
3.5.1	Gain Amplitude Fluctuation . . . . .	26
3.5.2	D-term . . . . .	27
3.5.3	Instrumental phase . . . . .	28
3.5.4	Summary . . . . .	28
<b>4</b>	<b>Polarization spectrometer, PolariS</b>	<b>29</b>
4.1	Introduction . . . . .	29
4.1.1	Polarization spectrometer . . . . .	29
4.1.2	Requirements . . . . .	30
4.2	Design and Development . . . . .	31
4.2.1	Measurement of the Stokes Parameters . . . . .	34
4.3	Verification . . . . .	34
4.3.1	Spectral Resolution Function . . . . .	34
4.3.2	Linearity . . . . .	36
4.3.2.1	Line Intensity . . . . .	37
4.3.2.2	Total Power . . . . .	38
4.3.3	Stability . . . . .	39
4.3.3.1	Time-based Allan Variance (TAV) . . . . .	39
4.3.3.2	Bandpass stability . . . . .	40
4.3.3.3	Spectral Allan Variance (SAV) . . . . .	42
4.3.4	Sensitivity . . . . .	43
4.3.5	Cross-correlation . . . . .	44
4.4	Field Test Observations . . . . .	45
4.5	Discussion . . . . .	46
4.6	Summary . . . . .	49
<b>5</b>	<b>Polarization calibration for Stokes V measurement</b>	<b>51</b>
5.1	Introduction . . . . .	51
5.2	Schematic view of the system . . . . .	52
5.2.1	Signal processing . . . . .	52
5.2.2	Observation method using our polarimetry device at the NRO 45m	53
5.3	Verification of instrumental configuration . . . . .	53
5.3.1	Observations . . . . .	55
5.3.2	Results and discussion . . . . .	56
5.4	Phase calibration . . . . .	56
5.4.1	Method . . . . .	56
5.4.2	Verification result . . . . .	59
5.4.3	Discussion about phase verification . . . . .	60
5.5	D-term calibration . . . . .	61
5.5.1	Theory of D-term effect measurement to Stokes V . . . . .	62
5.5.2	Observation and Results . . . . .	63
5.5.3	Discussion about D-term calibration . . . . .	64
5.6	Test observation of CCS molecule . . . . .	64
5.6.1	Observations . . . . .	64
5.6.2	Phase calibration . . . . .	65

5.6.3	Result . . . . .	65
5.6.4	Evaluation of Stokes V . . . . .	66
5.6.5	Discussion about Zeeman test observation . . . . .	67
5.7	Summary . . . . .	68
<b>6</b>	<b>Conclusions and remarks</b>	<b>70</b>
6.0.1	What Was Revealed? . . . . .	70
6.0.2	What Are Uncompleted? . . . . .	71
6.1	Future Prospects . . . . .	72
6.1.1	Measurement of magnetic field strength of molecular cores using our polarimetry device . . . . .	72
6.1.2	Use of PolariS and our polarimetry in another radio telescopes . .	72
<b>A</b>	<b>Feed alignment</b>	<b>73</b>
A.1	Relation of Stokes parameter and the angle between feed direction and north pole . . . . .	73
A.2	Estimation of feed direction . . . . .	73
A.2.1	observation . . . . .	74
A.2.2	Results and discussion . . . . .	75
	<b>Bibliography</b>	<b>77</b>

# List of Figures

1.1	Energy level variation with normal Zeeman splitting . . . . .	5
1.2	Polarization property with normal Zeeman splitting . . . . .	5
1.3	Magnetic field strength along line of sight measured by OH and CN Zeeman splitting. . . . .	6
2.1	Linear polarization and circular polarization definition in the case where radio waves propagate into the paper. . . . .	17
3.1	Outline of a polarimetry device . . . . .	19
4.1	Schematic diagram of the signal flow of the polarization detection system.	32
4.2	Schematic diagram of the PolariS system and signal flow inside. . . . .	33
4.3	The verification configuration. . . . .	35
4.4	The spectral resolution of the PolariS. . . . .	36
4.5	Linearity of PolariS for line observation. . . . .	37
4.6	Linearity of PolariS for continuum observation. . . . .	38
4.7	Total power variation and the time-based allan variance. . . . .	40
4.8	Time variation of bandpass shape. . . . .	41
4.9	Whole 54000-s integrated bandpass, and variation of mean and SD values of 1800-s integrated bandpass. . . . .	42
4.10	Bandpass shapes and the spectral Allan variances. . . . .	43
4.11	Variation of the root-mean-square with integration time. . . . .	44
4.12	Variation of correlation coefficients and the phase taken by the PolariS. .	45
4.13	Power spectra and cross power spectra of SiO maser ( $J = 1 - 0$ ) emission lines toward R Leo. . . . .	46
4.14	Power spectra and cross power spectra of CCS emission line toward TMC-1 at the spectral resolution of 1.95 kHz. . . . .	47
5.1	Schematic view of our polarimetry device . . . . .	54
5.2	Observation flow using PolariS at the NRO 45m . . . . .	55
5.3	Full stokes spectra toward NML-Tau with $H = E_x$ , $V = E_y$ without linearly polarized angle calibration. . . . .	56
5.4	Polarization angle variation . . . . .	57
5.5	Configuration to introduce artificial linear continuum source to the receiver using wire grid. . . . .	58
5.6	Delay and phase difference during for 1 hour . . . . .	59
5.7	Correlation between phase and delay difference . . . . .	60
5.8	A example of a phase difference caused by a delay variation . . . . .	62
5.9	Map and the spectrum of CCS molecule at TMC-1 . . . . .	65

5.10	Delay and phase difference during TMC-1 observation . . . . .	66
5.11	Stokes $I$ and $V$ of CCS molecular line toward TMC-1 . . . . .	66
5.12	Smoothed Stokes $I$ and frequency derivative of the smoothed $I$ . . . . .	67
5.13	Observed Stokes $V$ toward TMC-1 and the fitting result. . . . .	68
A.1	Relation between the basis for general Stokes parameter and for detected electric field. . . . .	74
A.2	Received total power variations during Crab Nebula observation . . . . .	75
A.3	Full Stokes parameter and polarization angle of Crab nebula without $RA$ calibration. . . . .	76

# List of Tables

4.1	Specifications of PolariS	31
5.1	Observation information of NML-Tau	55
5.2	Observation of Jupiter	63
5.3	Calibration value of V for IF0	64
5.4	Calibration value of V for IF1	64
A.1	Observation information of NML tau	74

# Symbols

$A_x$ and $A_y$	Amplification factors in x- and y- polarizations
$\vec{B}$	Magnetic field
$\tilde{D}_x$ and $\tilde{D}_y$	Cross coupling of x-polarization signal into y and y into x
$\vec{E}$	Electric field
$\tilde{E}_x$ and $\tilde{E}_y$	Electric field of electro-magnetic wave along x and y axes
$E_x$ and $E_y$	Amplitude of $\tilde{E}_x$ and $\tilde{E}_y$
$E_{x\nu}$ and $E_{y\nu}$	Spectrum of $E_x$ and $E_y$ as a function of the frequency, $\nu$
$\vec{e}_x$ and $\vec{e}_y$	Unit vector along x and y axes
$\tilde{F}'_x$ and $\tilde{F}'_y$	Electric field at the spectrometer affected by D-term for x- and y- polarizations
$\tilde{F}'_{\text{ON},x}$ and $\tilde{F}'_{\text{ON},y}$	$\tilde{F}'_x$ and $\tilde{F}'_y$ when a telescope pointed at ON point
$\tilde{F}'_{\text{OFF},x}$ and $\tilde{F}'_{\text{OFF},y}$	$\tilde{F}'_x$ and $\tilde{F}'_y$ when a telescope pointed at OFF point
$\tilde{F}'_{\text{HOT},x}$ and $\tilde{F}'_{\text{HOT},y}$	$\tilde{F}'_x$ and $\tilde{F}'_y$ when a feed is covered with absorber
$\tilde{G}_x$ and $\tilde{G}_y$	Antenna gain of x- and y- polarizations
$G_x$ and $G_y$	Amplitude of $\tilde{G}_x$ and $\tilde{G}_y$
$H_{\text{xx}^*}$ and $H_{\text{yy}^*}$	$T_{\text{src}}^*$ affected by D-term of auto correlation components of x and y
$H_{\text{xy}^*}$	$T_{\text{src}}^*$ affected by D-term of cross correlation component
$H_{\text{yx}^*}$	Complex conjugate of $H_{\text{xy}^*}$
$H_{\text{RR}^*}$	$T_{\text{src}}^*$ affected by D-term of auto correlation components of R and L
$k$	Wave number in chapter 2
$t$	time
$T_s$	Time period passing though one cycle
$T_{\text{A,src}}$	Target source antenna temperature affected by atmosphere absorption and feed efficiency
$T_{\text{A,src}}^*$	Target source antenna temperature
$T_{\text{A,xx}^*,\text{src}}, T_{\text{A,yy}^*,\text{src}}$	$T_{\text{A,src}}$ of auto correlation of x and y polarizations
$T_{\text{A,xy}^*,\text{src}}$	$T_{\text{A,src}}$ of cross correlation component
$T_{\text{RX},x}$ and $T_{\text{RX},y}$	Receiver noise temperature in the total system for x- and y- polarizations
$T_{amb}$	Atmosphere temperature

$T_{atm}$	Absorber temperature
$T_{gnd}$	Ground temperature around telescope.
$\lambda$	Wavelength
$R, L$	Right hand circle and left hand circle
$\delta_k$	Phase at $Z = 0$ and $t = 0$ of wave with wave number equal to $k$
$\delta_\nu$	Phase at $Z = 0$ and $t = 0$ of wave with wave number equal to $\nu$
$\delta_x$ and $\delta_y$	Phase at $Z = 0$ and $t = 0$ of wave along x- and y- axes
$\delta_{x\nu}$ and $\delta_{y\nu}$	Phase spectrum at $Z = 0$ and $t = 0$ of wave along x- and y- axes
$\eta_x$ and $\eta_y$	Efficiency of a telescope dish of x- and y- polarizations
$\nu$	frequency
$\theta$	polarization angle
$\xi$	Angle between the north pole and angle of polarimetry device
$-\phi_x$ and $-\phi_y$	Phase of $\tilde{E}_x$ and $\tilde{E}_y$
$-\phi_R$ and $-\phi_L$	Phase of $\tilde{E}_R$ and $\tilde{E}_L$
$-\psi_{g,x}$ and $-\psi_{g,y}$	Phase of $\tilde{G}_x$ and $\tilde{G}_y$
$-\psi_{obs,x}$	Phase of $\tilde{F}'_x$ , it's equal to $-\phi_x - \psi_{g,x}$
$-\psi_{obs,y}$	Phase of $\tilde{F}'_y$ , it's equal to $-\phi_y - \psi_{g,y}$

# Chapter 1

## Introduction

### 1.1 Overview of star formation

The universe is composed of many galaxies which contain stars and an ISM (interstellar medium). The chemical evolution of a galaxy is progressed by its stars; heavy elements are synthesized within the stars and ejected by supernova explosions to ISM . A low mass star such as the sun exists as a main-sequence star for  $\sim 10^{10}$  years. On the other hand, high mass star lives only  $\sim 10^7$  years (e.g.,[26]). Hence it is important to understand star-formation considering the star-forming rate and what a star is made of.

We introduce the typical scenario. A star forms inside relatively dense concentrations of interstellar gas and dusts, also known as molecular clouds. A subtle fraction of the interstellar gas is ionized by cosmic rays and ultraviolet photons. The ISM is usually as cold as 10 - 20 K. Typical hydrogen number density of molecular cloud is  $n_{\text{H}} = \sim 10^{2-3} \text{ cm}^{-3}$ , and star formation begins when the denser parts of the cloud core,  $n_{\text{H}} = \sim 10^{4-6} \text{ cm}^{-3}$ , collapse by self gravity (e.g.,[14]) which heats accretion; such a gas and dust. The accretion; such a particle becomes eventually warm enough to emit luminous infrared and microwave radiations. At this stage the warm dense core steps forward to the stage of protostar. The protostar, at first, only has about 1% of its final mass. But the envelope of the star continues to grow as material is accreting. A few million years later, thermonuclear fusion begins in its protostellar core, then a strong stellar wind is produced so as to stop farther mass phase is called the T-Tauri phase. A star in the T-Tauri phase can lose up to 50% of its mass before settling down as a main sequence star on the Hertzsprung-Russell diagram [43].

We don't fully understand the early stage of star formation; contraction process in molecular clouds for forming protostars. There are mainly three theoretical models on

star-formation at the early stage [10] and magnetic field strength is the key parameter to characterize these models. To verify these theoretical models, it is important to measure the strengths of the magnetic field associated cores by observations, in particular the cores prior to the protostellar formation, that is, pre-protostellar cores, or prestellar cores. Although the magnetic field in diffuse gas and proto stellar core had been estimated using the Zeeman splitting of OH, HI and CN radicals (e.g.,[7, 18]), the measurement of the magnetic field in prestellar cores has yet to be made. This is why we initiated a project to measure the magnetic fields in the protostellar cores by building a new specialized device.

In this chapter, firstly, I will briefly summarize the theoretical core-collapse models. Secondly, I review the literatures about the methods and observations of magnetic-field measurements. Thirdly, I propose an optimal design for magnetic-field measurements to verify the theoretical models, with our science goals.

## 1.2 Theoretical models of star formation

In this section I will introduce three proposed theoretical models of core collapse of star formation. As stated, the magnetic field is the key parameter for their identification.

### 1.2.1 Magnetic-field-driven star formation (strong magnetic field)

In this model, the magnetic field plays a dominant role in the gravitational collapse in the cores. The critical mass,  $M_\Phi$ , that can be supported by the magnetic flux,  $\Phi$ , is given as,  $M_\Phi = \Phi/2\pi\sqrt{G}$  [34] where  $G$  is a gravitational constant. This model is valid under the situation in which a molecular cloud mass,  $M$ , is smaller than the critical mass,  $M_\Phi$ ,  $M < M_\Phi = \Phi/2\pi\sqrt{G}$  [34]. Here the magnetic field is sufficiently strong to counteract gravitational collapse. Because the magnetic field is frozen only into the ionized gas and dust, neutral gas and dust contract gravitationally through the magnetic field. The process is known as ambipolar diffusion (e.g.,[58]), through which magnetic flux leakage is driven. When the mass of the core exceeds the critical mass, ( $M > M_\Phi$ ), the core will collapse to form. During the collapse, the magnetic field is dragged inward and magnetic pressure become stronger but not strong enough to halt collapse.

### 1.2.2 Turbulence-driven star formation (weak magnetic field)

In this model, molecular cores are formed through compression by supersonic flows in clouds and the cores are assumed to be below supercritical  $M > M_\Phi = \Phi/2\pi\sqrt{G}$ [25].

The magnetic field plays a minor role in the core evolution compared to the case of a strong magnetic field model (see section 1.2.1). At first, super sonic turbulence suppresses gravitational contraction in the cores. However it dissipates faster than free-fall, therefore a star is formed on a free-fall time scale ( $\sim 10^6$  years) [12, 25]. Magnetic pressure cannot halt the collapse, it can dominate turbulent pressure in the late stage of collapse [10]. .

### 1.2.3 Magnetic-field- and turbulence-driven star formation

In the two models shown above, the role of the magnetic field in star formation is very different. Recently a hybrid model has proposed in [32]. This model assumes that supersonic flow compresses the ISM forming a molecular cloud with progressing ambipolar diffusion. The molecular clouds is valid under subcritical ( $M < M_\Phi$ ), but the magnetic field is small compared with the no turbulence case [32]. The turbulence enhances ambipolar diffusion which compresses gas and dust in the molecular clouds. Upon becoming supercritical, it starts to collapse [51].

### 1.2.4 Method for constraining these models

As shown in the above, in theoretical models, different magnetic field strength are expected in the initial core and subsequently lead to a difference in core evolution. Hence the estimation of magnetic field in prestellar cores is important to constrain these models. For strong magnetic fields, the cores are initially subcritical ( $M < M_\Phi$ ) and thus the magnetic field halts collapse. However for a weak magnetic field case, cores are supercritical ( $M > M_\Phi$ ) and collapse dynamically. The typical core radius and masses are  $\sim 0.1$  pc and  $\sim 10 M_\odot$ , respectively [37], and the gravitationally-balanced magnetic field strength would be  $\sim 100 \mu\text{G}$  [46]. Thus, measurements of  $\sim 100 \mu\text{G}$  magnetic fields in prestar-forming cores are crucial to discriminate different star formation scenarios.

## 1.3 Estimation method of the Zeeman effect

The magnetic field strength in the ISM is estimated by the Chandrasekhar-Fermi method and Zeeman effect. Chandrasekhar & Fermi (1953) proposed a method to measure magnetic field strengths using the dispersion of linear polarization direction; it is called the Chandrasekhar-Fermi method. Ionized gas and dust are frozen into the magnetic field, therefore their motions are aligned to the magnetic field direction by a Lorentz force. Hence from linear polarization directions one can find magnetic field directions. With

stronger magnetic measurements. Smaller dispersion of linear polarization directions appears. Crutcher et al. obtained the magnetic field strength in the plane of sky [9]. However this method is affected by error due to e.g. gas density [41]. On the other hand, we can estimate a magnetic field strength along a line of sight directly using Zeeman splitting measurements. Here we outline the magnetic field measurement method based on the Zeeman splitting measurement in detail with references to [6, 8, 15, 30, 42].

The Zeeman effect represents the splitting of spectral lines by a magnetic field. The splitting occurs due to the interaction of the magnetic moment of elements (atoms and molecules) with the magnetic field. The splitting frequency width is given by  $\Delta\nu = ZB$ , where  $Z$  is the Zeeman splitting factor depending on the elements.  $Z$  is large with an unpaired electron, and such elements called free radical. In the normal Zeeman splitting, spectrum radiation is split into three different components with a  $\pi$  component unshifted in frequency and two  $\sigma$  components shifted by  $\Delta\nu = \pm Z|B|$ . We show an example in Fig 1.1, 1.2. Where the  $\pi$  component is linearly polarized in the plane of the sky parallel to  $B$ .  $\sigma$  components are circular and linearly polarized in the plane of the sky parallel and vertical to  $B$ , hence if we can detect each circularly polarized and linearly polarized components, we can estimate the 3 dimensional magnetic field. Spectral lines spread due to Doppler broadening, depending on temperature. The spread width  $\delta\nu$  is generally larger than the Zeeman splitting ( $\delta\nu \gg \Delta\nu$ ). In such a case, linearly polarized components are typically about an order of magnitude weaker than circularly polarized components. Hence we only obtain the line of sight magnetic field component,  $B_{Los}$  by fitting a circularly polarized spectrum and deriving of total power spectrum as

$$V = \Delta\nu \frac{dI}{d\nu}, \quad (1.1)$$

where  $V$  and  $I$  are the circularly polarized and total power spectrum, and  $\Delta\nu = B_{Los}Z$ . Since  $V$  is proportional to  $\Delta\nu$ , a narrow spectral line is better to detect Zeeman split. In most cases,  $\delta\nu \gg \Delta\nu$ , so we generally only estimate an upper limit of the magnetic field. Statistically, we can estimate the total magnetic field strength as  $\langle B_{Los} \rangle = |B|/2$  assuming magnetic fields are randomly oriented with respect to the observed line of sight.

## 1.4 Observational results of Zeeman splitting measurement

As shown in section 1.2, magnetic field estimation in prestellar cores is important to understand the star forming process. To date a number of magnetic field measurement have been conducted in HI and OH lines e.g.,[16, 18, 53]. The HI and OH trace low- and intermediate- density regions with  $n_H = \sim 10^{2-4} \text{ cm}^{-3}$  and the strength has been

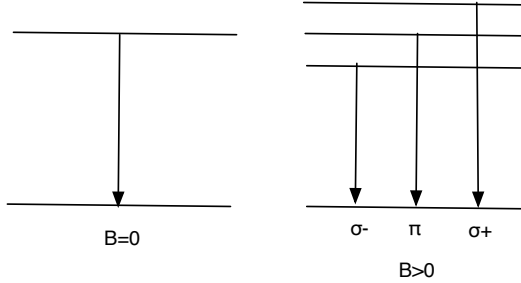


FIGURE 1.1: Energy level variation with normal Zeeman splitting  
(Left):A transition in the case of no magnetic field. (Right):A transition in the case of magnetic field.

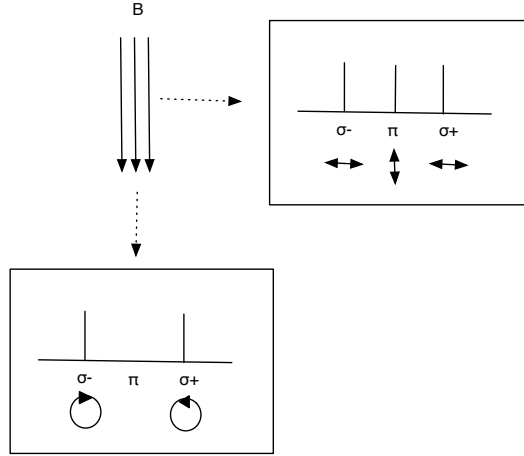


FIGURE 1.2: Polarization property with normal Zeeman splitting  
(Bottom):In case of magnetic field direction parallel to the line of sight. Each of the  $\sigma$  components are opposite circularly polarized. (Right):In the case of magnetic field direction perpendicular to the line of sight.  $\sigma$  and  $\pi$  components are linearly polarized and the polarization angles are perpendicular to each other. (originated from [30], with modification by the author)

observed with a comparatively large beam size. Hence it is difficult to discuss the magnetic field within a dense core in detail.

The 113 GHz lines of CN have been measured in [7, 13]. CN seems to be present mainly in a hotter ( $\sim 25$  K) and denser regions with  $n_H > \sim 10^5$  cm $^{-3}$  and such observations are strongly biased toward massive star-forming regions or protostellar cores at warm temperatures. As a result it is difficult to discuss prestellar cores in low mass star-formation. We show the main OH and CN survey results observed in [13, 53] in Fig. 1.3. A good tracer of dense cores in pre-stellar phase is CCS which is known to trace dense cores with  $n_H \sim 10^{4-5}$  cm $^{-3}$  in the early dark core stages, at a temperatures of 10 K [49]. This gives rise to intense and narrow emission lines in the millimeter-wave regime [23], and the Zeeman splitting factor is relatively large; 0.64 Hz/ $\mu$ G [45] at 45 GHz at the

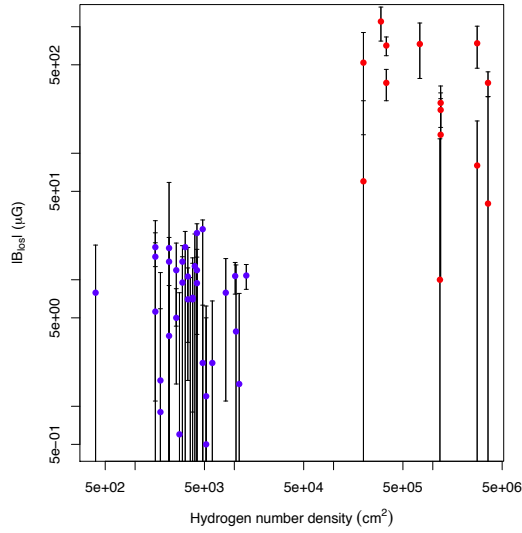


FIGURE 1.3: Magnetic field strength along line of sight measured by OH and CN Zeeman splitting.

The vertical axis indicate absolute magnetic field strength along line of sight. Colored points indicate measurement results and each bars indicate the  $1\sigma$  uncertainties. Red points is probed by CN in [13]. Blue points is probed by OH in [53].

$J_N = 4_3 - 3_2$  transition. Hence the CCS radical is thought to be a suitable probe to test star-formation models [33]. The Zeeman splitting detection of CCS toward prestellar cores is quite a difficult observation because of the Zeeman splitting is expected to be very subtle; the gravitationally-balanced magnetic field strength,  $\sim 100 \mu\text{G}$  will produce small 64 Hz shifts in the circular polarization spectrum of only few mK. Therefore, in spite of previous attempts [23, 44], no clear detection of the CCS Zeeman splitting has been reported. In previous studies, the two circularly polarized components were directly obtained. And in [23], only an upper limit ( $< 100 \mu\text{G}$ ) to the magnetic field strength along the line of sight in a core has been measured by a Zeeman splitting estimations in the CCS line, with 70 hrs observation time.

## 1.5 Our research aim and the outline of this thesis

Measurement of magnetic field strengths of  $100 \mu\text{G}$  in prestellar cores is important to constrain star forming scenarios (see section 1.2). It is desirable to employ the Zeeman splitting measurement of the CCS radical (see section 1.4). Hence we attempt to detect magnetic field strengths of  $100 \mu\text{G}$  in a prestellar core using the measurement of CCS Zeeman splitting. At  $100 \mu\text{G}$ , Zeeman splitting should be 64 Hz (see section 1.4). Hence our science goal is to measure 64 Hz Zeeman splitting in CCS molecule line with

a accuracy of  $5\sigma$  level. To achieve our science goal, we need a polarimetry device with a highly sensitive estimation of circular polarization and a high spectral resolution ( $64 < Hz$ ).

In the previous studies [23, 44], the two circularly polarized components were directly obtained. However a more high sensitive estimation of circular polarization can be obtained by cross-correlation between the two linearly polarized components. In the former, the polarization calibration tends to be more difficult because polarized components are affected more seriously by instrumental polarization (see chapter 3). Additionally to achieve a highly sensitive detection of CCS line, we need beam sizer smaller than a molecular core to avoid beam dispersion. We can resolve molecular core structures in nearby star forming regions with the Nobeyama radio 45 m telescope (NRO 45m) at 45.379 GHz using the  $J_N = 4_3 - 3_2$  transition of the CCS molecule. Hence we established a polarimetry device at the NRO 45m at 45 GHz band with linear polarized reception and 61 Hz spectral resolution ( $< 64Hz$ ). To operate the polarimetry device, we developed a polarization spectrometer, PolariS implementing auto- and cross- correlation spectra with 61 Hz spectral resolution and we connected PolariS to the dual linear polarization receiver Z45 at NRO 45m. Then we carried out test observations of CCS toward a pre star-forming core. The outline of this thesis is as follows. In chapter 2, we revisit the conventions of polarization description. In chapter 3, we summarize the systematic effects in polarization measurement and describe a method of accurate circular polarization (Stokes V) measurement. In chapter 4, we discuss the design, development, and commissioning of the polarization spectrometer (PolariS) for our science goal. In chapter 5, we report the calibration results of test polarization observations. In chapter 6, we conclude the thesis work and consider future prospects.

## Chapter 2

# Stokes parameters—Polarization description

Polarization is a physical property that characterizes the direction of the electric field of an electro-magnetic wave. Polarimetry often yields information that other method of observation cannot give. For most parts, magnetic fields and an asymmetric distribution of scattered radiation give rise to astronomical polarimetry. Hence properties of magnetic fields and scattering geometries are estimated using polarimetry. Polarimetry is the most direct method of detecting magnetic fields, which in astronomy range from  $10 \mu\text{G}$  in interstellar space to perhaps  $10^{18} \text{ G}$  in pulsars. The techniques used vary according to object [52]. The aim of our research is to measure the magnetic field in prestellar cores using the Zeeman splitting via polarization spectroscopy at radio frequencies (see section 1.3).

In this chapter, we aim to introduce the general polarization description using Stokes parameters. At first, we introduce the description of an electric field, polarization properties and characterize the polarization using Stokes parameters. The following definitions refer to [50], [29] and [52].

### 2.1 Electromagnetic waves

In 1864, Maxwell established electromagnetic wave process in Maxwell equations. Electromagnetic waves are transverse waves which propagates in the direction  $\vec{E} \times \vec{B}$ , where  $\vec{E}$  is the electric field and  $\vec{B}$  is magnetic field. The electric field is always perpendicular to the magnetic field. Assuming a vacuum space, we can write the wave function of the

electric field as

$$\nabla^2 \vec{E} = c^2 \frac{\partial^2}{\partial t^2} \vec{E}, \quad (2.1)$$

where  $c$  is the speed of light. We consider waves which propagate in only the  $z$  direction ( $\frac{\partial}{\partial x} = \frac{\partial}{\partial y} = 0$ ,  $\tilde{E}_z = 0$ ), equation 2.1 can be rewritten as

$$\frac{\partial^2 \tilde{E}_x}{\partial t^2} = c^2 \frac{\partial^2 \tilde{E}_x}{\partial z^2}, \quad (2.2)$$

$$\frac{\partial^2 \tilde{E}_y}{\partial t^2} = c^2 \frac{\partial^2 \tilde{E}_y}{\partial z^2}, \quad (2.3)$$

where  $\tilde{E}_x$  and  $\tilde{E}_y$  are  $x$  and  $y$  components of  $\vec{E}$ .

Equations 2.2 and 2.3 have a same form as

$$\frac{\partial^2 \Psi}{\partial t^2} - c^2 \frac{\partial^2 \Psi}{\partial z^2} = 0, \quad (2.4)$$

and its general solution is written as

$$\Psi(z, t) = F(z - ct) + G(z + ct). \quad (2.5)$$

$F(z - ct)$  and  $G(z + ct)$  describe progressive and regressive waves, respectively. The letter case is not considered anymore because in nature it doesn't exist.  $F(z - ct)$  can be expanded using particular solutions as

$$F_k(z - ct) = f_k \exp(ik(z - ct) + i\delta_k), \quad (2.6)$$

where  $k$  stands for the wave number, and  $f_k$  and  $\delta_k$  stand for the amplitude and phase at  $k$ , respectively. The real part of equation 2.6 expresses the electronic vector.

A more general wave function is written as

$$F_k(z - ct) = \int_{k=-\infty}^{\infty} f_k \exp(ik(z - ct) + i\delta_k) dk, \quad (2.7)$$

where  $k = 0, 1, 2, \dots$ . Equation 2.7 has form of a Fourier transform. From Euler's formula,

$$\exp(ik(z - ct) + i\delta_k) = \cos(k(z - ct) + i\delta_k) + i \sin(k(z - ct) + i\delta_k), \quad (2.8)$$

so the wave function is expressed as a sum of sinusoidal waves with phase,  $\phi = k(z - ct) + \delta_k$ .

We can rewrite the wave function using  $\nu = \frac{kc}{2\pi}$  (see section 2.1.1) as,

$$F_k(z - ct) = \int_{\nu=-\infty}^{\infty} f_{\nu} \exp \left( i2\pi\nu \left( \frac{z}{c} - t \right) + i\delta_{\nu} \right) d\nu, \quad (2.9)$$

where  $f_{\nu}$  is the wave amplitude at  $\nu$ . Hence solutions of equation 2.2 and 2.3 are

$$\tilde{E}_x = \int_{\nu=-\infty}^{\infty} E_{x\nu} \exp \left( i2\pi\nu \left( \frac{z}{c} - t \right) + i\delta_{x\nu} \right) d\nu, \quad (2.10)$$

$$\tilde{E}_y = \int_{\nu=-\infty}^{\infty} E_{y\nu} \exp \left( i2\pi\nu \left( \frac{z}{c} - t \right) + i\delta_{y\nu} \right) d\nu. \quad (2.11)$$

The electric vector,  $\vec{E}$  is equal to  $\tilde{E}_x \vec{e}_x + \tilde{E}_y \vec{e}_y$ , where  $\vec{e}_x$  and  $\vec{e}_y$  are the unit vectors in x- and y- direction.

### 2.1.1 Expression of a wave properties

We denote the wave parameters expressed in the wave function,  $f_k \exp(ik(z - ct) + i\delta_k)$ .

- $f_k$  is the amplitude of a wave.
- $k = \frac{\partial\phi}{\partial z}$  is called the wave number and indicates the phase differential per unit length.
- $\delta_k$  is a phase at  $t = 0$  and  $z = 0$ .
- $\lambda = \frac{2\pi}{k}$  is the wavelength.
- $T_s = \frac{2\pi}{kc}$  is the time period.
- $\nu = \frac{1}{T_s} = \frac{kc}{2\pi}$  and  $\omega = 2\pi\nu = kc$  are frequency and angular frequency, respectively.

## 2.2 Polarization radiation

Polarization is a physical property that characterizes the direction of electric field of electro-magnetic wave. There are three polarization patterns; a circle, a straight line, an ellipse, these are referred to as circular-, linear- and elliptical- polarization. Elliptical polarization is the general case of circular- plus linear- polarization.

A monochromatic wave is a 100% polarized signal and the electric field vector varies continuously and slowly. Astronomical signals are polychromatic signals. However to receive the signal, these signals generally pass through a narrow band filter, thus we acquire a quasi-monochromatic wave; the interval of frequency  $\Delta\nu$  is small compared with

the mean frequency. A polychromatic signal is the sum of many quasi-monochromatic signals. Such quasi-monochromatic waves look totally polarized in short timescales; shorter than  $1/\nu$ . However over much longer times amplitudes and phases change substantially and described as unpolarized, partially polarized and totally (100%) polarized. In the 100% polarized case, the electric vector of quasi-monochromatic and polychromatic signal does not vary continuously but the tip of electric field varies with a constant shape (circule, line or ellipse). An electric field can be resolved into two components at right angles to each other as shown in section 2.1. If the two electric field components vary randomly, without any lasting correlation between them in phase and amplitude, it is called an unpolarized signal. The partially polarized signal is the superposition of a 100% polarized and an unpolarized signal.

We describe the electric vector properties of 100% polarized signals in detail. The line of argument starts with an abstraction far removed from astronomy; a strictly monochromatic wave. It then proceeds to quasi-monochromatic and finally to polychromatic, partially polarized, which is the usual type of signal met with in astronomy.

### 2.2.1 Linear polarization

1. A monochromatic linearly polarized wave is the simplest concept. It has a transverse electric field with constant orientation, its electric vector at one point in space varying strictly sinusoidally with time. And the wave function has constant amplitude and frequency for all time.
2. We can conceptually convert this wave into one that is 100% linearly polarized but is quasi-monochromatic, by allowing the amplitude and phase to vary slowly and often randomly. If the vibration direction is same at all frequencies, it is still 100% polarized.
3. Fully or 100 % linear polarized polychromatic radiation is a superposition of 100 % linearly polarized quasi-monochromatic waves of many different frequencies and a common vibration angle. The electric vector is just a unique orientation of the otherwise often randomly vibration electric field vector.

### 2.2.2 Circular polarization

1. A monochromatic circular polarized wave can be seen as a combination of two orthogonal monochromatic linearly polarized waves of equal amplitude and differing by  $\pm 90^\circ$  in phase. The combined electric field vector has constant magnitude but

its orientation moves uniformly with time, making one resolution per wave period, rotating left or right according to sign of the phase difference.

2. In a quasi-monochromatic 100% circularly polarized wave, the tip of the electric field vector still moves around the circle, while the size of the circle also changes slowly. The signal is the superposition of two orthogonal quasi-monochromatic linearly polarized waves with  $90^\circ$  phase difference.
3. Polychromatic 100% polarized radiation is a super position of quasi-monochromatic waves of many different frequencies, but all circularly polarized in the same way. There is in general no stable phase relation between waves at different frequencies. Alternatively, viewing the total signal as a phase- and amplitude-modulated carrier wave, changes faster than in the quasi-monochromatic case. All the radiant energy is still associated with the circular motion of the field vector tip.

As noted in the monochromatic circular polarized case, left-hand-circle (L) and right-hand-circle (R) may be seen as a combination of two linearly polarized waves of equal amplitude with  $+90^\circ$  or  $-90^\circ$  phase difference. However R and L waves may themselves be used as the base for other polarization forms in the same way as two linear vibrations; two phase-correlated circular polarized waves of equal amplitude add to give linear polarization, the orientation of which depends on the (constant) phase difference between the R and L.

### 2.2.3 Elliptical polarization

The most general form of polarization is elliptical, for which the tip of the electric field vector executes an ellipse. The distinguishing parameters of the ellipse are orientation, axial ration and handedness; a linear and a circular polarization are special cases of this general form, and the elliptically polarization can be expressed as the summation of a linear- and a circular- polarization.

1. A monochromatic elliptically polarized wave may be visualized as the sum of two orthogonal unequal linearly polarized components with phase difference of  $\pm 90^\circ$ , or as the sum of two orthogonal linearly polarized components with a phase difference of something other than  $0^\circ$  or  $\pm 90^\circ$ . It is also possible to see elliptical polarizations as the sum of two unequal oppositely circularly polarized components with a constant phase difference between them.
2. Quasi-monochromatic 100% elliptically polarized radiation is obtained by allowing the size of the ellipse to vary slowly, with similar slow variations of the position

of the tip of the electric field vector within the ellipse. The ellipse pattern is a constant.

3. Polychromatic 100% elliptically polarized radiation is a sum of 100% polarized quasi-monochromatic components, all with the same elliptical polarization. The amplitude and phase varies randomly, however, the ellipse pattern is a constant.

## 2.3 Stokes parameter

In this section, we aim to introduce polarization descriptions using Stokes parameters. Stokes parameters have four quantities ( $I$ ,  $Q$ ,  $U$ ,  $V$ ) which all denote radiant energy per unit frequency interval, unit area. The absolute phase of wave does not enter into the definition. This representation of polarization was invented by Sir George Gabriel Stokes (1852) and it was revived and introduced into astronomy by Chandrasekhar (1946).

Electric fields are described as summation of some electric fields as shown in equation 2.7. Monochromatic waves are totally polarized, however, such waves are not observed (see section 2.2). Most of electric wave from space is unpolarized. The partially polarized case, expressed as the sum of an unpolarized and a polarized component, is thus important scientifically (see section 2.2).

First, to simplify, we show the Stokes parameter in the case of a monochromatic wave using the electric field definitions along x- and y- axes. We show the electric field definitions only along x- and y- axes in the linear frame (see section 2.1). In radio astrometry, however, an electric field definition in the circular frame is also used (see section 2.2.2). Hence in the next part, we introduce the two wave definitions (in linear and circular frames), and then, we introduce the general definitions of Stokes parameters in circular and linear frames.

### 2.3.1 Monochromatic wave

Monochromatic waves are fully polarized. We introduce the polarization description of the monochromatic wave using Stokes parameters.

We define a example of a monochromatic wave of frequency,  $\nu_0$  at  $z = 0$  as

$$\vec{E} = (E_{x\nu_0} \exp(i\delta_{x1}) \vec{e}_x + E_{y\nu_0} \exp(i\delta_{y1}) \vec{e}_y) \exp(-i2\pi t\nu_0), \quad (2.12)$$

where  $E_{x\nu_0}$ ,  $E_{y\nu_0}$  and  $\delta_{x1}$ ,  $\delta_{y1}$  are constant amplitudes and phases. Taking the real part of  $\vec{E}$ , we find the physical components of the electric field to be

$$\text{Re}(\vec{E}_{x\nu_0}) = E_{x\nu_0} \cos(i2\pi t\nu_0 - \delta_{x1}), \quad (2.13)$$

$$\text{Re}(\vec{E}_{y\nu_0}) = E_{y\nu_0} \cos(i2\pi t\nu_0 - \delta_{y1}). \quad (2.14)$$

The function,  $\text{Re}()$  refer to the real part.

We now introduce relations of wave plane properties and a totally polarized wave function. We show an example of a wave plane which trace out an ellipse in Fig. 2.1. We assume it's principal axes  $x'$  and  $y'$  tilt at an angle  $\chi$ . First of all, we define the wave equation on  $x'$ - and  $y'$ - axis as

$$\text{Re}(\vec{E}_{x\nu_0}') = E_0 \cos(\beta \cos(i2\pi t\nu_0)), \quad (2.15)$$

$$\text{Re}(\vec{E}_{y\nu_0}') = -E_0 \sin(\beta \sin(i2\pi t\nu_0)), \quad (2.16)$$

where  $-\pi/2 << \beta << \pi/2$ . The ellipse will be traced out in a clockwise sense for  $0 < \beta < \pi/2$  and counter clockwise sense for  $-\pi/2 < \beta < 0$ , as viewed by an observer toward whom the wave is propagating. In case of  $\beta = \pm\pi/4$ , the ellipse becomes a circle and it is called circular polarization. In case of  $\beta = 0$  or  $\pm\pi/2$ , the ellipse become a line and it is called linear polarization.

We make the connections between equation 2.13, 2.14 and 2.15, 2.16. We transform the  $x'$ - and  $y'$ - components, 2.15 and 2.16 to the  $x$ - and  $y$ - axes by rotating  $\chi$ . This yields

$$\text{Re}(\vec{E}_{x\nu_0}) = E_0 (\cos \beta \cos \chi \cos(i2\pi t\nu_0) + \sin \beta \sin \chi \sin(i2\pi t\nu_0)), \quad (2.17)$$

$$\text{Re}(\vec{E}_{y\nu_0}) = E_0 (\cos \beta \sin \chi \cos(i2\pi t\nu_0) - \sin \beta \cos \chi \sin(i2\pi t\nu_0)), \quad (2.18)$$

These are identical to eq. 2.13, 2.14 if we take

$$E_{x\nu_0} \cos \delta_{x1} = E_0 \cos \beta \cos \chi, \quad (2.19)$$

$$E_{x\nu_0} \sin \delta_{x1} = E_0 \sin \beta \sin \chi, \quad (2.20)$$

$$E_{y\nu_0} \cos \delta_{y1} = E_0 \cos \beta \sin \chi, \quad (2.21)$$

$$E_{y\nu_0} \sin \delta_{y1} = -E_0 \sin \beta \cos \chi. \quad (2.22)$$

Given parameters,  $E_{x\nu_0}$ ,  $E_{y\nu_0}$ ,  $\delta_{x1}$ ,  $\delta_{y1}$  can be derived for  $\beta$ ,  $E_0$  and  $\chi$  in equation 2.19 – 2.22.

Stokes parameters for monochromatic waves, which are defined by equations:

$$\begin{pmatrix} I \\ Q \\ U \\ V \end{pmatrix} = \begin{pmatrix} E_0^2 \\ E_0^2 \cos 2\beta \sin 2\chi \\ E_0^2 \cos 2\beta \sin 2\chi \\ E_0^2 \sin 2\beta \end{pmatrix} = \begin{pmatrix} E_{x\nu_0}^2 + E_{y\nu_0}^2 \\ E_{x\nu_0}^2 - E_{y\nu_0}^2 \\ 2E_{x\nu_0}E_{y\nu_0} \cos(\delta_{x1} - \delta_{y1}) \\ 2E_{x\nu_0}E_{y\nu_0} \sin(\delta_{x1} - \delta_{y1}) \end{pmatrix}. \quad (2.23)$$

Pure elliptical polarization is determined solely by three parameters:  $E_0$ ,  $\beta$  and  $\chi$ . Therefore there is one relation that exists between the four Stokes parameters and that is

$$I^2 = Q^2 + U^2 + V^2, \quad (2.24)$$

which means that the total radiation energy is polarized. A Stokes parameter description using two amplitudes and phases in 2.23 is used for general description and the definition is same as the general description shown in 2.28

$$\begin{pmatrix} I \\ Q \\ U \\ V \end{pmatrix} = \begin{pmatrix} E_{x\nu_0}^2 + E_{y\nu_0}^2 \\ E_{x\nu_0}^2 - E_{y\nu_0}^2 \\ 2E_{x\nu_0}E_{y\nu_0} \cos(\delta_{x1} - \delta_{y1}) \\ 2E_{x\nu_0}E_{y\nu_0} \sin(\delta_{x1} - \delta_{y1}) \end{pmatrix} = \begin{pmatrix} E_x^2 + E_x^2 \\ E_x^2 - E_x^2 \\ \tilde{E}_x^* \tilde{E}_y^* + \tilde{E}_y^* \tilde{E}_x^* \\ -i\tilde{E}_x^* \tilde{E}_y^* + i\tilde{E}_y^* \tilde{E}_x^* \end{pmatrix}, \quad (2.25)$$

where “\*” refers to the complex conjugate.

The meaning of the Stokes parameters are as follows:

- $I$  is nonnegative and describe the total intensity.
- $V$  is circular polarized intensity. The wave has right- or left-handed polarization when  $V$  is positive or negative, respectively;  $V = 0$  is the condition for linear polarization in case of monochromatic a wave.
- $Q$  and  $U$  are linear polarized intensity and total linear intensity is  $\sqrt{Q^2 + U^2}$ .  $Q$  is a difference between components along x- and y- axes and  $U$  is a difference between components along  $+45^\circ$  and  $-45^\circ$  from the x axis (see Fig. 2.1).  $\chi$  is the orientation of the elliptical polarization and linear polarization toward the x axis; called the polarization angle and it can be solved using Stokes  $Q$ ,  $U$  as  $\tan 2\chi = \frac{U}{Q}$
- $Q = U = 0$  is the condition for circular polarization in case of a monochromatic wave.

Hence the relation 2.24 indicates that the whole total intensity  $I$  is polarized.

### 2.3.2 Quasi-monochromatic waves

The monochromatic wave is totally polarized. However observed signals in radio telescopes are quasi-monochromatic waves (see section 2.2) and are described as unpolarized, partially polarized or totally polarized wave. Let us define Stokes parameters in (general) quasi-monochromatic wave. First we define orthogonal components for electric vectors. As shown in section 2.1, we define the electric wave with two linear polarized vectors along x and y axes. We can also describe an electric wave with summation of two orthogonal circular polarized vectors: righthand- and lefthand- circular polarizations. We define the base of righthand- and lefthand- circular polarizations as R and L, respectively. We now show the vectors xy and RL frame:

$$\vec{J}_{xy} = \begin{pmatrix} \tilde{E}_x \\ \tilde{E}_y \end{pmatrix} = \begin{pmatrix} E_x e^{-i\phi_x} \\ E_y e^{-i\phi_y} \end{pmatrix}, \quad (2.26)$$

where  $E_x$  and  $E_y$  are amplitudes and  $\phi_x$  and  $\phi_y$  are phases and

$$\vec{J}_{RL} = \begin{pmatrix} \tilde{E}_R \\ \tilde{E}_L \end{pmatrix} = \begin{pmatrix} E_R e^{-i\phi_R} \\ E_L e^{-i\phi_L} \end{pmatrix}, \quad (2.27)$$

where  $E_R$  and  $E_L$  are amplitudes and  $\phi_R$  and  $\phi_L$  are phases, respectively. In the case of a quasi-monochromatic wave, the amplitudes and phases in equation 2.26 and 2.27 vary substantially compared to monochromatic waves. Observed components are processed by a spectrometer and recorded as an output value; in the spectrometer, electronic waves apply auto- and cross- correlation and time-averaging as  $\langle E_x E_y^* \rangle$ ,  $\langle E_x E_x^* \rangle$ , and so on, where brackets  $\langle \rangle$  refer to the time average. And Stokes parameter are described using their values. In linear frame,

$$\begin{pmatrix} I \\ Q \\ U \\ V \end{pmatrix} = \begin{pmatrix} 1 & 0 & 0 & 1 \\ 1 & 0 & 0 & -1 \\ 0 & 1 & 1 & 0 \\ 0 & -i & i & 0 \end{pmatrix} \begin{pmatrix} \langle E_x^2 \rangle \\ \langle \tilde{E}_x \tilde{E}_y^* \rangle \\ \langle \tilde{E}_y \tilde{E}_x^* \rangle \\ \langle E_y^2 \rangle \end{pmatrix}. \quad (2.28)$$

In circular frame,

$$\begin{pmatrix} I \\ Q \\ U \\ V \end{pmatrix} = \begin{pmatrix} 1 & 0 & 0 & 1 \\ 0 & 1 & 1 & 0 \\ 0 & i & -i & 0 \\ -1 & 0 & 0 & 1 \end{pmatrix} \begin{pmatrix} \langle E_R^2 \rangle \\ \langle \tilde{E}_R \tilde{E}_L^* \rangle \\ \langle \tilde{E}_L \tilde{E}_R^* \rangle \\ \langle E_L^2 \rangle \end{pmatrix}. \quad (2.29)$$

$\sqrt{Q^2 + U^2 + V^2}$  describes the total polarized wave power. In quasi monochromatic wave, total radio energy  $I$  is not always polarized ( $I \geq \sqrt{Q^2 + U^2 + V^2}$ ); from Schewartz inequality,  $\langle E_x E_y \rangle \geq \langle E_x E_{y^*} \rangle$  and  $\langle E_R E_R \rangle \geq \langle E_R E_{L^*} \rangle$ , we can easily find the relation. At the other extreme, there are completely unpolarized waves, where the between phases of orthogonal polarizations has no permanent relation and where there is no preferred orientation so that between orthogonal auto-correlation components are same. In this case,  $Q = U = V = 0$ . Polarization rate is defined as the ratio of  $I$  to  $Q, U, V$ ; intermediate polarization rate is  $\sqrt{Q^2 + U^2 + V^2}/I$ , intermediate linear polarization rate is  $\sqrt{Q^2 + U^2}/I$  and intermediate circular polarization rate is  $V/I$ .

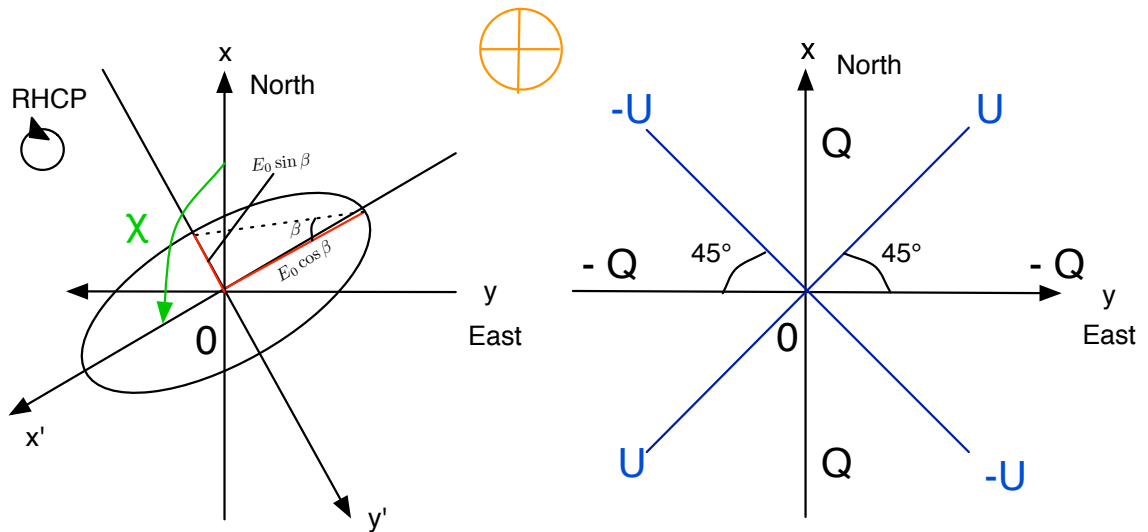


FIGURE 2.1: Linear polarization and circular polarization definition in the case where radio waves propagate into the paper.

(Left):A polarization ellipse.  $\chi$  is the polarization angle. (Right):Stokes Q and U components.

# Chapter 3

## Measurement of circular polarization

### 3.1 Introduction

Our aim is to estimate accurate Stokes  $V$  spectra for measurement of Zeeman shift in CCS molecular line. In this chapter we introduce a polarimetry (especially Stokes  $V$  measurement) in radio regime. In a general polarimetry in single dish radio observation, an instrumental polarization is added by some aspects:(1) D-term, (2)instrumental phase in cross correlation and (3)gain variation. And each effect to Stokes  $V$  is different between two reception ways (circular and linear reception). In the following section, we quantify the observed wave and discuss which reception is desirable for measurement of the Stokes  $V$ . Firstly, we introduce a general radio polarimetry device. Secondly, we show the instrumental effects through signal processing. Thirdly, we define an antenna temperature and show a method of the antenna temperature measurement of a radio source. Finally, we summarize the instrumental effects to Stokes  $V$ .

### 3.2 Polarimetry device

In radio polarimetry using a general single dish, radio signal is processed as follows.

1. Radio waves is concentrated by optics consisted with a dish and a feed horn.
2. the concentrated signals are separated two orthogonal polarizations, x and y or R and L by a OMT (orthomode transducer).

3. The polarizations are individually propagated and proceed by some components; (a) amplifiers in order to decrease the random noise owing to signal procedure, (b) band-pass filters which select range of frequencies to optimize signal processing of other components, (c) down converters which convert observed signal frequency to more lower frequency using a mixer with aid of a monochromatic wave that is called Lo (Local) signal.
4. In ADC (analog to digital converter), each polarization is individually converted to analog signal.
5. In a polarization spectrometer, auto and cross correlation of two orthogonal polarizations are calculated. We show the example of a signal procedure in Fig. 3.1.

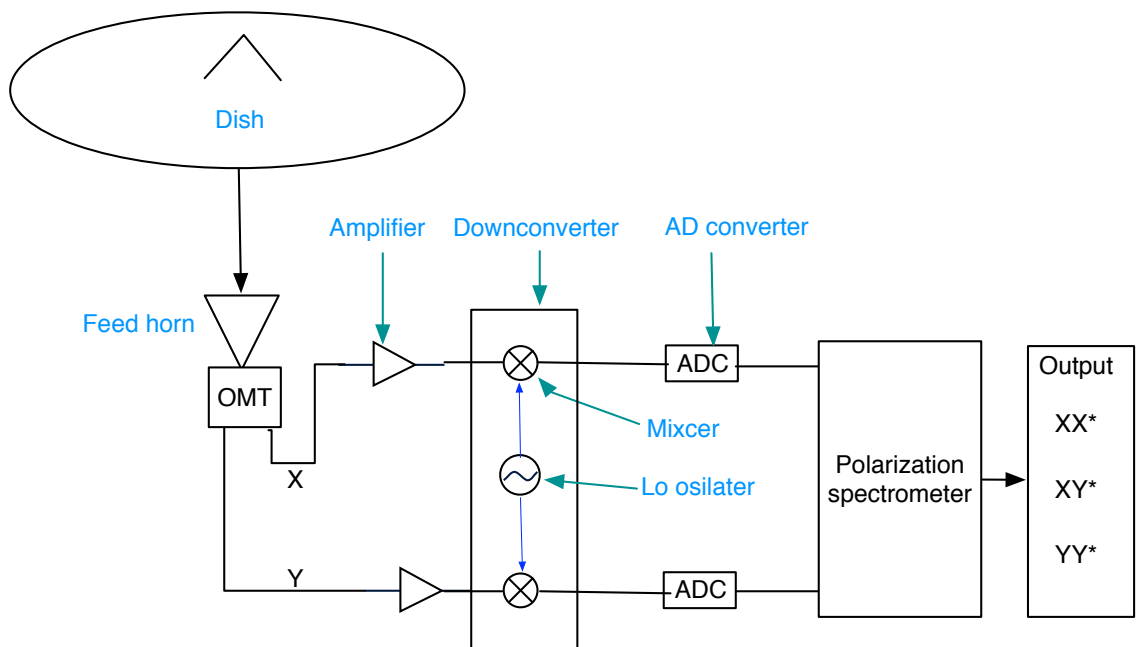


FIGURE 3.1: Outline of a polarimetry device

### 3.3 Instrumental effects through signal processing

#### 3.3.1 Phase difference

Phases of each polarization has systematic errors through signal processing. Therefore phases of cross correlation spectra between the two polarizations have instrumental phases. We show the property of instrumental phases of a cross correlation spectrum.

1. A difference of propagation length,  $\Delta L$ , between two orthogonal polarizations add a slope to the cross correlation phase spectrum. In cross correlation phase,  $\Delta L$

cause  $2\pi\nu\frac{\Delta L}{c}$  [rad]; assign  $z$  to  $\Delta L$  in equation 2.9. We define  $\frac{\Delta L}{c} = \tau_{\Delta L}$ , and it's called delay.

2. A phase difference of local signals between two orthogonal polarizations,  $\psi_a$  [rad] occur a phase shift of  $\psi_a$  [rad].
3. Non-linearity of equipments (e.g. down-converter, filter) warp phase characters of two polarizations. The phase shifts are large in the band edge. We define phase shifts in the cross correlation phase spectrum as  $\psi_{b,\nu}$ ; is function of frequency.

We define the phase of x polarization affected systematic errors is  $\psi_{\text{obs},x} = \phi_x + \psi_{g,x}$ , where  $\psi_{g,x}$  is an instrumental phase. In y, R and L polarization, we replace x to y, R and L, respectively. And an instrumental cross correlation phase,  $\psi_{g,x} - \psi_{g,y}$  can be described using the definition shown above as  $\psi_{g,x} - \psi_{g,y} = \psi_a + 2\pi\nu\tau_{\Delta L} + \psi_{b,\nu}$ .

### 3.3.2 D-term

In a general radio receiver, a radio signal is separate two polarizations (R-,L- or x-,y-polarization) as shown in section 3.2. Each separated signal, however, contain another polarization due to imperfection of systems (e.g. imperfect symmetry of optics and imperfect deviation). We denote the percentage of the leakage to x- and y- polarizations are  $D_x$  and  $D_y$  which is called D-term. Each separated signal at a spectrometer for x- and y- polarizations,  $F'_x$  and  $F'_y$  are express as

$$\tilde{F}'_x = A_x \exp(-i\psi_{g,x}) \left( \tilde{E}_x + \tilde{D}_x \tilde{E}_y - \tilde{D}_y \tilde{E}_x \right), \quad (3.1)$$

$$\tilde{F}'_y = A_y \exp(-i\psi_{g,y}) \left( \tilde{E}_y + \tilde{D}_y \tilde{E}_x - \tilde{D}_x \tilde{E}_y \right), \quad (3.2)$$

where  $A_x$  and  $A_y$  are amplification factors of the polarimetry device. Decreasing powers,  $-\tilde{D}_y \tilde{E}_x$  and  $-\tilde{D}_x \tilde{E}_y$  only affect to auto correlation and the effect is enough small compared to the pure auto correlation. Therefore generally the term is ignored like

$$\tilde{F}'_x = A_x \exp(-i\psi_{g,x}) \left( \tilde{E}_x + \tilde{D}_x \tilde{E}_y \right), \quad (3.3)$$

$$\tilde{F}'_y = A_y \exp(-i\psi_{g,y}) \left( \tilde{E}_y + \tilde{D}_y \tilde{E}_x \right). \quad (3.4)$$

D-term is typically small as few % [4]. So we ignore terms with 2nd order in D-term, then the auto correlation and the cross correlation expand as

$$\begin{aligned}\langle \tilde{F}'_x \tilde{F}'_x^* \rangle &= A_x^2 (\tilde{E}_x + \tilde{D}_x \tilde{E}_y)(\tilde{E}_x^* + \tilde{D}_x^* \tilde{E}_y^*) \\ &= A_x^2 \left( \langle \tilde{E}_x \tilde{E}_x^* \rangle + \tilde{D}_x^* \langle \tilde{E}_x \tilde{E}_y^* \rangle + \tilde{D}_x \langle \tilde{E}_y \tilde{E}_x^* \rangle + \tilde{D}_x \tilde{D}_x^* \langle \tilde{E}_y \tilde{E}_y^* \rangle \right) \\ &\sim A_x^2 \left( \langle \tilde{E}_x \tilde{E}_x^* \rangle + \tilde{D}_x^* \langle \tilde{E}_x \tilde{E}_y^* \rangle + \tilde{D}_x \langle \tilde{E}_y \tilde{E}_x^* \rangle \right),\end{aligned}\quad (3.5)$$

$$\begin{aligned}\langle \tilde{F}'_y \tilde{F}'_y^* \rangle &= A_y^2 (\tilde{E}_y + \tilde{D}_y \tilde{E}_x)(\tilde{E}_y^* + \tilde{D}_y^* \tilde{E}_x^*) \\ &= A_y^2 \left( \langle \tilde{E}_y \tilde{E}_y^* \rangle + \tilde{D}_y^* \langle \tilde{E}_y \tilde{E}_x^* \rangle + \tilde{D}_y \langle \tilde{E}_x \tilde{E}_y^* \rangle + \tilde{D}_y \tilde{D}_y^* \langle \tilde{E}_x \tilde{E}_x^* \rangle \right) \\ &\sim A_y^2 \left( \langle \tilde{E}_y \tilde{E}_y^* \rangle + \tilde{D}_y^* \langle \tilde{E}_y \tilde{E}_x^* \rangle + \tilde{D}_y \langle \tilde{E}_x \tilde{E}_y^* \rangle \right),\end{aligned}\quad (3.6)$$

$$\begin{aligned}\langle \tilde{F}'_x \tilde{F}'_y^* \rangle &= A_x A_y \exp(-i\psi_{g,x} + i\psi_{g,y})(\tilde{E}_x + \tilde{D}_x \tilde{E}_y)(\tilde{E}_y^* + \tilde{D}_y^* \tilde{E}_x^*) \\ &= A_x A_y \exp(-i\psi_{g,x} + i\psi_{g,y}) \left( \langle \tilde{E}_x \tilde{E}_y^* \rangle + \tilde{D}_y^* \langle \tilde{E}_x \tilde{E}_x^* \rangle + \tilde{D}_x \langle \tilde{E}_y \tilde{E}_y^* \rangle + \tilde{D}_x \tilde{D}_y^* \langle \tilde{E}_y \tilde{E}_x^* \rangle \right) \\ &\sim A_x A_y \exp(-i\psi_{g,x} + i\psi_{g,y}) \left( \langle \tilde{E}_x \tilde{E}_y^* \rangle + \tilde{D}_y^* \langle \tilde{E}_x \tilde{E}_x^* \rangle + \tilde{D}_x \langle \tilde{E}_y \tilde{E}_y^* \rangle \right)\end{aligned}\quad (3.7)$$

$$\begin{aligned}\langle \tilde{F}'_y \tilde{F}'_x^* \rangle &= A_y A_x \exp(-i\psi_{g,y} + i\psi_{g,x})(\tilde{E}_y + \tilde{D}_y \tilde{E}_x)(\tilde{E}_x^* + \tilde{D}_x^* \tilde{E}_y^*) \\ &= A_y A_x \exp(-i\psi_{g,y} + i\psi_{g,x}) \left( \langle \tilde{E}_y \tilde{E}_x^* \rangle + \tilde{D}_x^* \langle \tilde{E}_y \tilde{E}_y^* \rangle + \tilde{D}_y \langle \tilde{E}_x \tilde{E}_x^* \rangle + \tilde{D}_y \tilde{D}_x^* \langle \tilde{E}_x \tilde{E}_y^* \rangle \right) \\ &\sim A_y A_x \exp(-i\psi_{g,y} + i\psi_{g,x}) \left( \langle \tilde{E}_y \tilde{E}_x^* \rangle + \tilde{D}_x^* \langle \tilde{E}_y \tilde{E}_y^* \rangle + \tilde{D}_y \langle \tilde{E}_x \tilde{E}_x^* \rangle \right).\end{aligned}\quad (3.8)$$

In case of R, L receptions, we replace x, y to R, L.

### 3.4 Estimation of an antenna temperature of a radio source

In radio astronomy, energies of radio waves obtained using a radio telescope express in temperature and the temperature is called antenna temperature. In this chapter, we aim to show the estimation method of an antenna temperature of a radio source. In a traditional study, antenna temperature in auto correlation of unpolarized source and a estimation method for the antenna temperature unaffected by D-term of radio source using chopper wheel method is well defined [40]. However it wasn't well summarized about a polarized source, cross correlation and D-term effects in an estimated antenna temperature. We conceptionally convert the antenna temperature definition of the previous work into for a polarized source and for a cross correlation, and we summarize estimation methods of antenna temperatures of radio source affected by D-term effect for auto- and cross correlation using the chopper wheel method. In the following sections, at first, we show the relation of antenna temperatures and electric fields, and then show the measurement method of antenna temperatures of radio source.

### 3.4.1 Antenna temperature

We introduce a concept of antenna temperature. From Maxwell equations, an energy density of radiative electromagnetic field constituted by electric field ( $\tilde{E}$ ) and magnetic field ( $\tilde{B}$ ) along with the corresponding  $\tilde{E}$  are written as

$$S = \tilde{E}(t) \times \tilde{B}(t) = \tilde{E}(t)\tilde{E}(t)^*/Z, \quad (3.9)$$

where  $Z$  is an impedance in vacuum, and the energy density,  $S$  is called a pointing vector. Hence the power into a receiver for x- and y- polarizations,  $W_x$  and  $W_y$ , are expressed as

$$W_x = \frac{Ae}{Z} \iint_{4\pi} \tilde{E}_x \tilde{E}_x^* \tilde{P}_n(\theta, \psi) d\Omega, \quad (3.10)$$

$$W_y = \frac{Ae}{Z} \iint_{4\pi} \tilde{E}_y \tilde{E}_y^* \tilde{P}_n(\theta, \psi) d\Omega, \quad (3.11)$$

where  $Ae$  is an effective aperture,  $\theta$  and  $\phi$  are angle in spherical coordinate system;  $\theta$  is measured from a main beam center of an antenna,  $P_n(\theta, \phi)$  is normalized power pattern of the antenna, and  $\Omega$  is solid angle ( $\Omega = \sin \theta d\theta d\phi$ ).

From the equation 3.10 and 3.11, the whole inputted power,  $W$  is

$$W = W_x + W_y \quad (3.12)$$

Using the Nyquist theorem, we can introduce an antenna temperature  $T_A$  as

$$W = kT_A. \quad (3.13)$$

This definition of the antenna temperature relates the output (input) of the antenna to the power of a matched resistor. And  $W_x$  and  $W_y$  are written as

$$W_x = \frac{1}{2}kT_{A,xx^*}, \quad (3.14)$$

$$W_y = \frac{1}{2}kT_{A,yy^*}, \quad (3.15)$$

where  $T_{A,xx^*}$  and  $T_{A,yy^*}$  are antenna temperature for x- and y- polarizations. In case of unpolarized radiation,  $T_{A,xx^*} = T_{A,yy^*}$ , and from 3.12 and 3.15, the total input power is written as

$$W = W_x + W_y = kT_{A,xx^*} = kT_{A,yy^*}. \quad (3.16)$$

Substituting equation 3.14 and 3.15 into equation 3.10 and 3.11 respectively,  $T_{A,xx^*}$  and  $T_{A,yy^*}$  are

$$T_{A,xx^*} = \frac{2Ae}{kZ} \iint_{4\pi} \tilde{E}_x \tilde{E}_x^* \tilde{P}_n(\theta, \psi) d\Omega, \quad (3.17)$$

$$T_{A,yy^*} = \frac{2Ae}{kZ} \iint_{4\pi} \tilde{E}_y \tilde{E}_y^* \tilde{P}_n(\theta, \psi) d\Omega. \quad (3.18)$$

In equation 3.17, 3.18 ! ! auto correlation electric field for x- and y- polarizations convert to the antenna temperature. In a cross correlation component, though the similar discussion, we can define an (complex) antenna temperature as

$$\tilde{T}_{A,xy^*} = \frac{2Ae}{kZ} \iint_{4\pi} \tilde{E}_x \tilde{E}_y^* \times \tilde{P}_n(\theta, \psi) d\Omega. \quad (3.19)$$

Here, we consider a radiation following black body radiation. An energy density of a black body radiation with  $h\nu/kT \ll 1$  (where h is Planck constant) follow the Rayleigh-Jeans law,

$$S(T_B) = \frac{2kT_B}{\lambda^2}, \quad (3.20)$$

where  $k$  is the Boltzmann constant and  $T_B$  is a temperature of the black body;  $T_B$  is called a brightness temperature. From equation 3.9 and 3.20,

$$\tilde{E} \tilde{E}^* / Z = \frac{2kT_B}{\lambda^2}. \quad (3.21)$$

Hence substituting equation 3.21 into 3.17,  $T_{A,x}$  is written as

$$\tilde{T}_{A,xx^*} = \frac{Ae}{\lambda^2} \iint_{4\pi} T_B \times \tilde{P}_n(\theta, \psi) d\Omega. \quad (3.22)$$

In a traditional radio study, the relation of  $\lambda$ ,  $P_n$  and  $A_e$  are defined as

$$\lambda^2 = A_e \iint_{4\pi} P_n(\theta, \phi) d\Omega, \quad (3.23)$$

and the equation indicates beam pattern is sharper with larger antenna and shorter wave length.

From equation 3.21 and 3.17,  $T_{A,x}$  is rewritten as

$$\tilde{T}_{A,xx^*} = \frac{T_B \iint_{4\pi} \tilde{P}_n(\theta, \psi) d\Omega}{\iint_{4\pi} P_n(\theta, \phi) d\Omega}, \quad (3.24)$$

which describe a convolution of the brightness temperature with the beam pattern of telescope. If the electric field is constant over the whole beam,  $T_A = T_B$ .

### 3.4.2 Measurement of antenna temperature of a radio source

We explain a usual estimation of an antenna temperature of a radio source using the chopper wheel method. At first, we define an antenna temperature of the radio source received in a feed horn from the radio source through the earth's atmosphere,  $T_{A,\text{src}}$  is

$$T_{A,\text{src}} = \eta T_{\text{src}}^* \exp(-\tau \sec Z), \quad (3.25)$$

where  $\eta$  is a feed efficiency,  $Z$  is zenith angle ( $90^\circ - EL$ ) and  $\tau$  is optical depth,  $T_{A,\text{src}}^*$  is commonly referred to as the corrected antenna temperature; but it is really a forward beam brightness temperature because of lack of consideration about effective aperture of dish.

We explain an estimation method of  $T_{A,\text{src}}^*$ . In a single-dish radio observation, a atmosphere has a large influence and can change rapidly, so we must often make accurate corrections. Additionally receiver noises and a signal from ground around telescope also have a influence; radiation around ground propagate to a telescope because of imperfection of antenna optics and the effect is called spillover. We give an analysis of the calibration procedure using chopper wheel method. The procedure consists of: (1) the measurement of receiver output when the feed horn is directed toward radio source, ON point , (2) the measurement of receiver output when the feed horn is directed toward cold sky, OFF point, and (3) the measurement of the receiver output when an absorver. We show the results of (1), (2), (3) using equation 3.5–3.8 and 3.17–3.19.

Signals from blank sky, grand, receiver noise are unpolarized. Hence result of (1), the auto- and cross- correlation of the receiver signals while measuring the ON point are

$$\begin{aligned} \langle \tilde{F}'_{\text{ON},x} \tilde{F}'^*_{\text{ON},x} \rangle &= \tilde{G}_x \tilde{G}_x^* [T_{A,xx^*,\text{src}} + T_{\text{RX},x} + (1 - \eta) T_{\text{gnd}} + \eta (1 - \exp(-\tau \sec Z)) T_{\text{atm},A,x} \\ &\quad + \tilde{D}_x^* \tilde{T}_{A,xy^*,\text{src}} + \tilde{D}_x \tilde{T}_{A,xy^*,\text{src}}^*], \end{aligned} \quad (3.26)$$

$$\begin{aligned} \langle \tilde{F}'_{\text{ON},x} \tilde{F}'^*_{\text{ON},y} \rangle &= \tilde{G}_x \tilde{G}_y \tilde{T}_{A,xy^*,\text{src}} \\ &\quad + \tilde{G}_x \tilde{G}_y^* [\tilde{D}_y^* (T_{A,xx^*,\text{src}} + T_{\text{RX},x} + (1 - \eta) T_{\text{gnd}} + \eta (1 - \exp(-\tau \sec Z)) T_{\text{atm}}) \\ &\quad + \tilde{D}_x (T_{A,yy^*,\text{src}} + T_{\text{RX},y} + (1 - \eta) T_{\text{gnd}} + \eta (1 - \exp(-\tau \sec Z)) T_{\text{atm},A,y})], \end{aligned} \quad (3.27)$$

**where:**  $T_{A,xx^*,\text{src}}$  and  $T_{A,yy^*,\text{src}}$  are  $T_{A,\text{src}}^*$  for x- and y- polarizations,

$\tilde{T}_{A,xy^*,\text{src}}$  is  $T_{A,\text{src}}^*$  for a cross correlation component between x- and y-polarization;  
 $T_{A,\text{src}}^* = T_{A,xy^*,\text{src}} \exp(-i\phi_x)$  where  $T_{A,xy^*,\text{src}}$  is a amplitude,

$$\tilde{G}_x = G_x \exp(-i\psi_{g,x}); G_x = A_x/kZ,$$

$$\tilde{G}_y = G_y \exp(-i\psi_{g,y}); G_y = A_y/kZ,$$

$T_{\text{RX},x}$  and  $T_{\text{RX},y}$  are the receiver noise temperature for x and y,

$T_{\text{amb}}$  is a temperature on the ground around the telescope,

$T_{\text{atm}}$  is a temperature of atmosphere.

Results of (2), the auto and cross correlation while measuring the OFF point are written as

$$\begin{aligned} \langle \tilde{F}'_{\text{OFF},x} \tilde{F}'^*_{\text{OFF},x} \rangle &= \tilde{G}_x \tilde{G}_x^* [T_{\text{RX},x} + (1 - \eta) T_{\text{gnd}} \\ &\quad + \eta (1 - \exp(-\tau \sec Z)) T_{\text{atm}}], \end{aligned} \quad (3.28)$$

$$\begin{aligned} \langle \tilde{F}'_{\text{OFF},x} \tilde{F}'^*_{\text{OFF},y} \rangle &= \tilde{G}_x \tilde{G}_y^* \left[ \tilde{D}_y^* (T_{\text{RX,A},x} + (1 - \eta) T_{\text{gnd}} + \eta (1 - \exp(-\tau \sec Z)) T_{\text{atm}}) \right. \\ &\quad \left. + \tilde{D}_x (T_{\text{RX,A},y} + (1 - \eta) T_{\text{gnd}} + \eta (1 - \exp(-\tau \sec Z)) T_{\text{atm}}) \right]. \end{aligned} \quad (3.29)$$

Absorbers are unpolarized source. Hence results of (3), the auto and cross correlation when an absorber which the temperature is  $T_{\text{amb}}$  puts over a receiver are written as

$$\langle \tilde{F}'_{\text{HOT},x} \tilde{F}'^*_{\text{HOT},x} \rangle = \tilde{G}_x \tilde{G}_x^* [T_{\text{RX},x} + T_{\text{amb}}], \quad (3.30)$$

and

$$\langle \tilde{F}'_{\text{HOT},x} \tilde{F}'^*_{\text{HOT},y} \rangle = \tilde{G}_x \tilde{G}_x^* \left[ \tilde{D}_y^* (T_{\text{RX},x} + T_{\text{amb}}) + \tilde{D}_x (T_{\text{RX},y} + T_{\text{amb},y}) \right]. \quad (3.31)$$

Assuming  $T_{\text{amb}} = T_{\text{gnd}} = T_{\text{atm}}$ , we can estimate  $T_{\text{A,src}}^*$ s affected by D-term of auto correlation component for x polarization:  $H_{\text{xx}*}$  and cross correlation component:  $H_{\text{xy}*}$  from equation 3.26– 3.31 as

$$\begin{aligned} H_{\text{xx}*} &= T_{\text{amb}} \frac{\langle \tilde{F}'_{\text{ON},x} \tilde{F}'^*_{\text{ON},x} \rangle - \langle \tilde{F}'_{\text{OFF},x} \tilde{F}'^*_{\text{OFF},x} \rangle}{\langle \tilde{F}'_{\text{HOT},x} \tilde{F}'^*_{\text{HOT},x} \rangle - \langle \tilde{F}'_{\text{OFF},x} \tilde{F}'^*_{\text{OFF},x} \rangle} \\ &= \frac{T_{\text{A,xx*,src}} \exp(\tau \sec Z) + \tilde{D}_x^* \tilde{T}_{\text{A,xy*,src}} + \tilde{D}_x \tilde{T}_{\text{A,xy*,src}}^*}{\eta} \\ &= T_{\text{A,xx*,src}}^* + \tilde{D}_x^* \tilde{T}_{\text{A,xy*,src}}^* + \tilde{D}_x \tilde{T}_{\text{A,xy*,src}}^{**}, \end{aligned} \quad (3.32)$$

where  $T_{A,xx^*,\text{src}}^*$  is a  $T_{A,\text{src}}^*$  of auto correlation component for x polarization. and

$$\begin{aligned} H_{xy^*} &= T_{\text{amb}} \frac{\left\langle \tilde{F}'_{\text{ON},x} \tilde{F}'_{\text{ON},y}^* \right\rangle - \left\langle \tilde{F}'_{\text{OFF},x} \tilde{F}'_{\text{OFF},y}^* \right\rangle}{\sqrt{\left\langle \tilde{F}'_{\text{HOT},x} \tilde{F}'_{\text{HOT},x}^* \right\rangle - \left\langle \tilde{F}'_{\text{OFF},x} \tilde{F}'_{\text{OFF},x}^* \right\rangle} \sqrt{\left\langle \tilde{F}'_{\text{HOT},y} \tilde{F}'_{\text{HOT},y}^* \right\rangle - \left\langle \tilde{F}'_{\text{OFF},y} \tilde{F}'_{\text{OFF},y}^* \right\rangle}} \\ &= \frac{T_{A,xy^*,\text{src}} \exp(\tau \sec Z) + \tilde{D}_y^* \tilde{T}_{A,xx^*,\text{src}} - \tilde{D}_x \tilde{T}_{A,yy^*,\text{src}}}{\eta} \\ &= \tilde{T}_{A,xy^*,\text{src}}^* + \tilde{D}_y^* \tilde{T}_{A,xx^*,\text{src}}^* - \tilde{D}_x \tilde{T}_{A,yy^*,\text{src}}^*, \end{aligned} \quad (3.33)$$

where  $\tilde{T}_{A,xy^*,\text{src}}^*$  is a  $T_{\text{src}}^*$  of cross correlation component. And in the same way, for autocorrelation of y polarization;  $H_{yy^*}$  and the other cross correlation component:  $H_{yx^*}$  is written as

$$H_{yy^*} = T_{A,yy^*,\text{src}}^* + \tilde{D}_y^* \tilde{T}_{A,xy^*,\text{src}}^* + \tilde{D}_y \tilde{T}_{A,xy^*,\text{src}}^{**}, \quad (3.34)$$

$$H_{yx^*} = \tilde{T}_{A,xy^*,\text{src}}^{**} + \tilde{D}_x^* \tilde{T}_{A,yy^*,\text{src}}^* - \tilde{D}_y \tilde{T}_{A,xx^*,\text{src}}^* \quad (3.35)$$

In case of a R, L reception, we replace x, y to R, L.

### 3.5 Relation of receiving methods and Stokes V measurement accuracy

Stokes V is affected instrumental effects; gain amplitude fluctuation, D-term and instrumental phase in cross-correlation. The influences to Stokes V measurement is differ between linear- and circular- reception. We show the influences and discuss which reception better to accurate Stokes V measurement.

#### 3.5.1 Gain Amplitude Fluctuation

Radio signals amplified and decayed in instrumental process and the factor is amplitude of gains,  $G_x$  and  $G_y$  (see in section 3.4). We discuss the effect of the gain amplitude variation.

We assume the gain amplitudes change between OFF and ON scan. We express the gain amplitudes during observation of OFF and absorver is  $G_x$  and  $G_y$  for x- and y-polarization; this is the same definition in section 3.4.2. We express gain amplitude during observation of ON is  $G_x + \Delta G$  and  $G_y + \Delta G$  for x- and y-polarization;  $\Delta G$  is an amount of change. In such case, the antena temperature of a radio source for auto and cross correlation component using the similar estimation of equation 3.32 and 3.33 are

written as

$$H_{xx} + T_{\text{amb}} \frac{\Delta G^2 \langle \tilde{F}'_{\text{ON},x} \tilde{F}'^*_{\text{ON},x} \rangle}{G_x G_x \langle \tilde{F}'_{\text{HOT},x} \tilde{F}'^*_{\text{HOT},x} \rangle - \langle \tilde{F}'_{\text{OFF},x} \tilde{F}'^*_{\text{OFF},x} \rangle}, \quad (3.36)$$

$$H_{xy^*} + T_{\text{amb}} \frac{\Delta G^2 \langle \tilde{F}'_{\text{ON},x} \tilde{F}'^*_{\text{ON},y} \rangle}{G_x G_y \sqrt{\langle \tilde{F}'_{\text{HOT},x} \tilde{F}'^*_{\text{HOT},x} \rangle - \langle \tilde{F}'_{\text{OFF},x} \tilde{F}'^*_{\text{OFF},x} \rangle} \sqrt{\langle \tilde{F}'_{\text{HOT},y} \tilde{F}'^*_{\text{HOT},y} \rangle - \langle \tilde{F}'_{\text{OFF},y} \tilde{F}'^*_{\text{OFF},y} \rangle}} \quad (3.37)$$

As shown above in observed signals are almost unpolarized and in generally,  $\langle \tilde{F}'_{\text{ON},x} \tilde{F}'^*_{\text{ON},x} \rangle$  is over 100 times larger than  $\langle \tilde{F}'_{\text{ON},x} \tilde{F}'^*_{\text{ON},y} \rangle$ . Hence the effect of  $\Delta G$  of the auto correlation component is far larger than the cross correlation component. Gain amplitudes variate with some aspects (eg. variation of temperature and fluctuations of currents to amplifiers). And the prediction of the variation is difficult. Hence the calibration of gain amplitude variation is difficult.

Stokes V measurement of R, L and x, y reception are using auto and cross correlation, respectively. So in x, y reception is better than R, L reception in Stokes V measurement.

### 3.5.2 D-term

From equations 3.32– 3.35, estimated StokesV which is affected by D-term in a circular and linear reception,  $V'_{\text{src},R,L}$  and  $V'_{\text{src},x,y}$ , are written in 3.38 and 3.39. D-term typically is not so variable, therefore we can calibrate the effect. We show the method in section 5.5.

$$\begin{aligned} V'_{\text{src},R,L} &= H_{LL^*} - H_{RR^*} \\ &= T_{A,RR^*,\text{src}}^* + (\tilde{D}_R^* \tilde{T}_{A,RL^*,\text{src}}^* + \tilde{D}_R \tilde{T}_{A,RL^*,\text{src}}^{**}) - (T_{A,LL^*,\text{src}}^* + \tilde{D}_L^* \tilde{T}_{A,RL^*,\text{src}}^* + \tilde{D}_L \tilde{T}_{A,RL^*,\text{src}}^{**}) \\ &= V_{\text{src}} + (\tilde{D}_R^* - \tilde{D}_L) \tilde{T}_{A,RL^*,\text{src}}^* + (\tilde{D}_R^* - \tilde{D}_L) \tilde{T}_{A,RL^*,\text{src}}^{**}, \end{aligned} \quad (3.38)$$

where  $V_{\text{src},R,L}$  is an observed Stokes V affected by D-term in a R, L reception and  $V_{\text{src}}$  is a pure stokes V.

$$\begin{aligned} V'_{\text{src},x,y} &= -iH_{xy^*} + iH_{yx^*} \\ &= -i(\tilde{T}_{A,xy^*,\text{src}}^* + \tilde{D}_y^* T_{A,xx^*,\text{src}}^* + \tilde{D}_x T_{A,yy^*,\text{src}}^*) + i(\tilde{T}_{A,xy^*,\text{src}}^{**} + \tilde{D}_y T_{A,xx^*,\text{src}}^* + \tilde{D}_x^* T_{A,yy^*,\text{src}}^*) \\ &= V + i((-\tilde{D}_x + \tilde{D}_x^*) T_{A,yy^*,\text{src}}^* + (\tilde{D}_y - \tilde{D}_y^*) T_{A,xx^*,\text{src}}^*) \\ &= V + 2\text{Im}(\tilde{D}_x) T_{A,yy^*,\text{src}}^* - 2\text{Im}(\tilde{D}_y) T_{A,xx^*,\text{src}}^*, \end{aligned} \quad (3.39)$$

where the function,  $\text{Im}()$  refer a imaginary part and  $V_{\text{src},x,y}$  is an observed Stokes V affected by D-term in a x,y reception.

### 3.5.3 Instrumental phase

Cross correlation phases are changed owing to instrumental effects (see section 3.3.1). The effect causes systematic error to Stokes V estimated in linear reception. As shown in equation 2.29, in a linear polarization reception, Stokes  $U, V$  is expressed as

$$\begin{aligned} U &= \langle \tilde{E}_x \tilde{E}_y^* \rangle + \langle \tilde{E}_y \tilde{E}_x^* \rangle, \\ V &= -i \langle \tilde{E}_x \tilde{E}_y^* \rangle + i \langle \tilde{E}_y \tilde{E}_x^* \rangle. \end{aligned}$$

When we multiply  $i$  to the equation for  $U$  and add the equation for  $Q$  then,

$$2 \langle \tilde{E}_x \tilde{E}_y^* \rangle = U + iV. \quad (3.40)$$

$U$  and  $V$  are real quantities. Hence equation 3.40 indicate that imaginary part of  $2 \langle \tilde{E}_x \tilde{E}_y^* \rangle$  is Stokes  $V$ , and instrumental phase causes misestimation of Stokes  $V$  and Stokes  $U$  components. Additionally, phase difference of cross correlation during integration times result in decorrelation. As shown in section 5.4, we can estimate instrumental phase using strong artificial linearly polarized continuum source. Therefore if the instrumental phase is enough stable, these effects are negligible for Stokes  $V$  measurement. In case of using a processer for VLBI observation controlled by hydrogen maser clock, phases in the system will be enough stable.

### 3.5.4 Summary

Stokes V is affected by gain amplitude fluctuation, D-term and instrumental phases in cross-correlation. We can calibrate D-term and the instrumental phase however accurate calibration of the gain variation is difficult. Gain variation causes large error in an auto-correlation than a cross correlation. So in stokes V measurement, linear reception is better than circular reception.

## Chapter 4

# Polarization spectrometer, PolariS

### Abstract

We developed a software-based polarization spectrometer, ‘PolariS’, to acquire full-Stokes spectrum with a very high spectral resolution of 61 Hz. The primary aim of the PolariS is to measure the magnetic fields in dense star-forming cores using the Zeeman effect of molecular emission lines. The PolariS consists of a commercially available analog-to-digital converter (ADC) and a LINUX computer. The computer is equipped with a GPU (graphics processing unit) to process FFT (Fast Fourier Transform) and cross correlation using the CUDA (Compute Unified Device Architecture) library developed by NVIDIA. Thanks to the enough precision in the ADC quantization and arithmetic in the GPU, PolariS offers excellent performances in linearity, dynamic range, sensitivity, bandpass flatness and stability. The software has been released under the MIT License and is available to the public. In this chapter, we report the design of the PolariS and its performance verified through engineering tests and commissioning observations.

### 4.1 Introduction

#### 4.1.1 Polarization spectrometer

A polarisation spectrometer measures the polarimetric properties of the incident radiation as a function of frequency. The Stokes parameters,  $I$ ,  $Q$ ,  $U$  and  $V$  represent polarized light (see section 2.3.2). A typical astronomical receiving system is sensitive

to either linear or circular polarisation. In both cases, the receiving system will measure two products, either two orthogonal linear polarisations or two opposite circular polarisations. In order to obtain all four Stokes parameters from the two observables, both auto and cross-correlation products must be obtained from the received polarisations (see section 2.3.2).

In a modern radio telescope, the signal processing of the correlation is numerically handled with a digital spectrometer. For example, the XPOL correlation polarimeter system is installed on the IRAM30-m telescope [54] and the VESPA digital polarization spectrometer of the system yields a 40-kHz spectral resolution across a 120-MHz bandwidth. The ACS spectrometer is installed on the Green Bank Telescope (GBT) and offers a 49-kHz spectral resolution in a 12.5-MHz bandwidth. The WAPP correlator [11] is used in the Arecibo radio telescope mainly for pulsar observations, with a 0.195 MHz resolution. These digital spectrometers are composed of specific hardwares designed for certain fixed specifications. In this case, in order to obtain flexible and scalable performances such as finer spectral resolution, better sensitivity, or wider bandwidth, it is necessary to build different devices that meet the requirements.

Software implementations are often easier and cheaper to develop than hardware solutions to fulfill scalable specifications. The former is superior in some respects. The processing codes written in a programming language are readable, verifiable, and possible to open in public. The software is flexible and scalable for required modification of specifications. Processors are commercial off-the-shelf products allowing us to build the spectrometer at reasonable cost and easily replace each processor with a spare. Thus a software-based spectrometer for pulsar processing is built [3, 27] on GBT.

In this chapter, we report construction of the software-based polarization spectrometer, PolariS. The scientific requirement and the corresponding spectrometer specification to meet it which is described in section 4.1.2. The basic design and costs are presented in section 4.2. The verification is reported in section 4.3. And in section 4.4, results of test observations toward a radio source is described.

#### 4.1.2 Requirements

The primary aim of PolariS is to detect the Zeeman split of the molecular emission line of CCS  $J_N = 4_3 - 3_2$  transition at 45.379 GHz for the purpose of measurement of magnetic field strength in protostellar cores in molecular clouds. The expected magnetic field of  $\sim 100 \mu\text{G}$  will yield the Zeeman shift of  $\sim 64 \text{ Hz}$ [45] between two orthogonal circular polarizations. The Zeeman split will appear in the Stokes V (circular polarization)

spectrum as

$$V(\nu) \simeq \frac{dI(\nu)}{d\nu} \Delta\nu, \quad (4.1)$$

where  $I(\nu)$  is the Stokes  $I$  spectrum as a function of the frequency,  $\nu$ , and  $\Delta\nu$  is the Zeeman split. Our pilot observations of CCS molecules (see section 4.4) indicate that the line profile toward the Taurus Molecular Cloud 1 has  $\frac{dI}{d\nu} \sim 0.16 \text{ mK Hz}^{-1}$  that corresponds to  $V \sim 10 \text{ mK}$  assuming  $\Delta\nu = 64 \text{ Hz}$ .

In our project we use the Z45 receiver [33, 55] which is capable of receiving two orthogonal linear polarizations. The Stokes  $V$  component can be obtained via cross-correlations between two linear polarizations. To measure such a weak and narrow Stokes  $V$  feature with Z45, The combination of Z45 and PolariS is required to have specifications of (1) measurements of auto-correlation and cross-correlation, (2) spectral resolution better than the expected Zeeman shift of 64 Hz, (3) adequate sensitivity, and (4) frequency stability better than 60 Hz. The total cost was limited to our budget of JPY 2,000,000.

## 4.2 Design and Development

Fig. 4.1 shows the schematic diagram of the signal path to a polarization spectrometer. The functions of the digital FX-type polarization spectrometer are (1) to accept the received signal in two orthogonal polarizations in digital, (2) to calculate spectra of the real-time signal streams via FFT (fast-Fourier transform), (3) to produce power spectra and cross power spectra by multiplying the spectra, and (4) to integrate the power spectra and output them.

TABLE 4.1: Specifications of PolariS

Feature	Specification	Remarks
Number of IFs	4 ( $X_0, X_1, Y_0, Y_1$ )	2 pols., 2 IFs
Bandwidth	8 MHz / IF	4 MHz / IF
Quantization	4 bit/sample	8 bit/sample
Spectral resolution	131072 ch/IF	65536 ch/IF
Autocorrelation	4 real products	$\langle X_0 X_0^* \rangle, \langle X_1 X_1^* \rangle, \langle Y_0 Y_0^* \rangle, \langle Y_1 Y_1^* \rangle$
cross-correlation	2 complex products	$\langle X_0 Y_0^* \rangle, \langle X_1 Y_1^* \rangle$
Time resolution	1 sec	

$X, Y$  stands for two orthogonal polarizations. Suffix indicates basebands.  
Sample table notes.

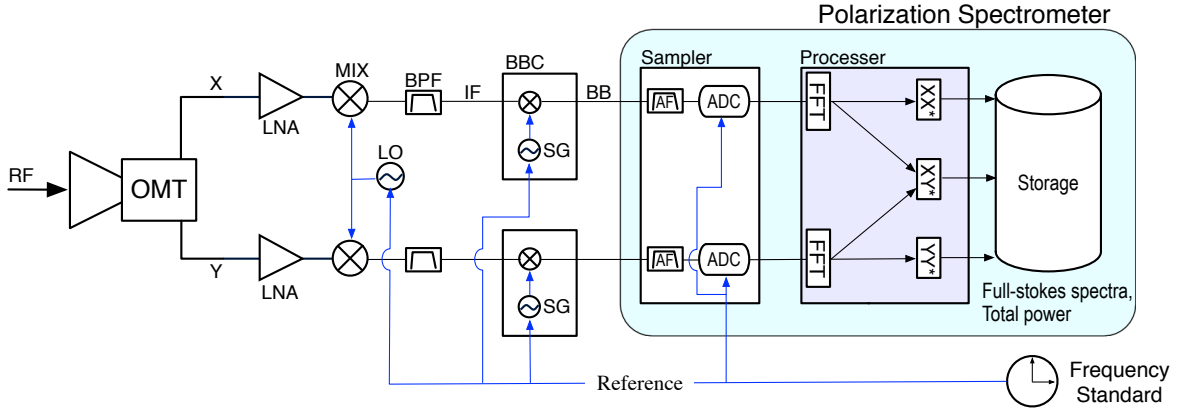


FIGURE 4.1: Schematic diagram of the signal flow of the polarization detection system. The RF (radio frequency) waves incident on the dual polarization receiver will be split into two polarizations (X and Y) in the OMT (ortho-mode transducer), amplified in the LNAs (low noise amplifiers), and downconverted in the MIXs (mixers) using the LO (local oscillator) signal referencing the frequency standard. The IF (intermediate frequency) signals through BPFs (bandpass filters) will be downconverted to basebands (BBs) with BBCs (baseband converters) at desired frequency of SGs (signal generator), and input to a polarization spectrometer. The polarization spectrometer consists of a sampler, a processor, and storage. The sampler consists of AFs (anti-alias filters) and ADCs (analog-to-digital converter). The digitized signals are converted into spectra though a FFT (fast-Fourier transform) process and then multiplications between them are taken to output power and cross spectra ( $XX^*$ ,  $XY^*$ , and  $YY^*$ ), which yield full Stokes spectra. Detailed signal processing inside the spectrometer is described in Fig. 4.2.

Table 4.1 lists the specification of PolariS. The specification of the 61-Hz resolution at 4 or 8 MHz bandwidth requires 65536 or 131072 spectral channels, respectively. To produce the spectrum in real time, 262144- or 131072-point FFT must be accomplished within less than 8 msec. This processing requires 1440 Mflops per IF or 5600 Mflops for all IFs. Adding 262 Mflops for autocorrelations cross products, at least  $\sim 6$  Gflops is necessary for real-time processing.

To meet the required specifications within the limited development cost of JPY 2,000,000, we decided to design PolariS as a software-based spectrometer that consists of a VLBI digitizer, K5/VSSP32 [21] for data acquisition, and a general-purpose personal computer (PC) with a graphic processing unit (GPU) for signal processing. Thanks to recent advances in digital technology, PCs have become capable of wide-bandwidth signal processing. Furthermore, recent GPUs for video games perform TFLOPS (tela floating operations per second) arithmetic with a low cost.

Fig. 4.2 shows the flow of signal processes in PolariS. The K5/VSSP32 VLBI sampler accepts four analog signal streams with the maximum bandwidth of 32 MHz; 64–96

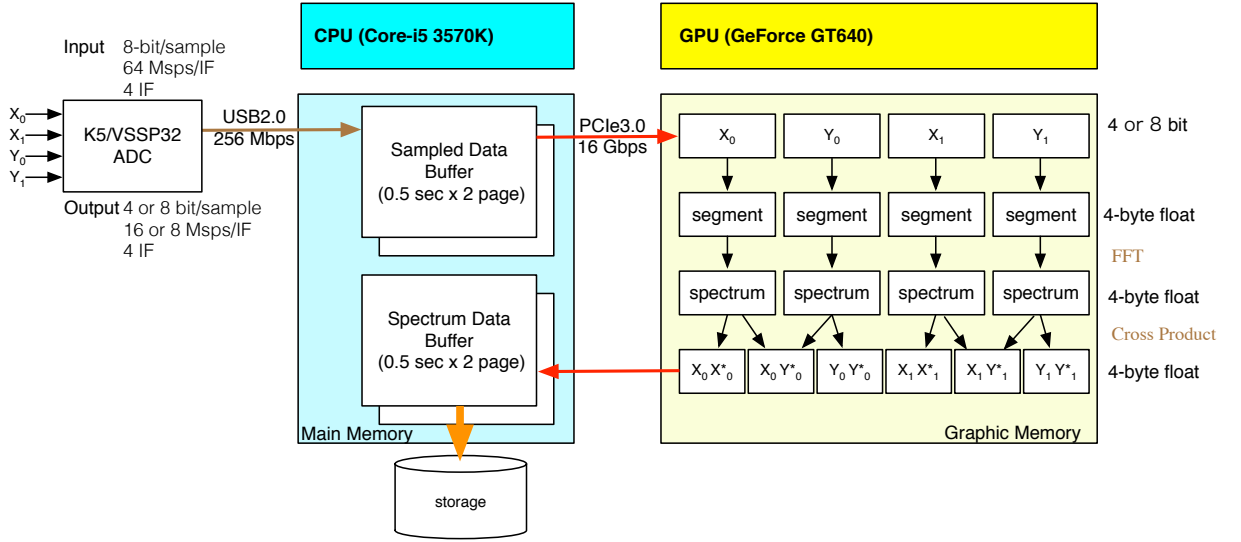


FIGURE 4.2: Schematic diagram of the PolariS system and signal flow inside.

PolariS consists of the K5/VSSP32 analog-to-digital converter (ADC) and the host computer including CPU, GPU, and storage. The ADC accepts four analog IF signals of 32-MHz bandwidth and digitizes with a sampling speed of 64 Msps/IF and quantization of 8 bit. The digitized signal will be output with 4-bit quantization when we need 8-MHz bandwidth (16 Msps/IF) after applying digital filtering to reduce the total data rate down to 256 Mbps to meet the USB2.0 bus. The CPU captures 32 MBytes data twice a second in the two-page buffer and sends them to GPU memory. The GPU processes data translation (4 or 8-bit integer to 4-byte float), segmentation, FFT, cross productions, and accumulation. Each segment contains 131072 or 262144 samples to produce 65536 or 131072 spectral channels. The (cross) power spectra will be transmitted to the main memory and stored in the file system.

MHz or 0 – 4 MHz signals using the NTK7638 or NTK7631 baseband converters for bandwidth selection of 8 or 4 MHz, respectively. The input of four baseband signals is digitized in the digitizer at 64 Msps, 8-bit quantization. Thus, harmonics sampling is employed for the input of 64–96 MHz signals. To accommodate the maximum output data rate of 256 Mbps in USB 2.0, digital filtering and quantization-level reduction are applied to the digitized signals [22]. The current PolariS system allows two modes: (1) 8-MHz (16 Msps) bandwidth, 4-bit quantization, and (2) 4-MHz bandwidth, 8-bit quantization.

The host computer of PolariS works on the Linux (Ubuntu 12.04 LTS) operating system. The control and signal-processing softwares are coded in GCC (GNU Compiler Collection) and NVCC (NVIDIA CUDA Compiler). The cuFFT library is employed for fast-Fourier transform (FFT) of time-domain signals to frequency-domain spectra. Total power of each IF signal is measured by histograms of digitized signals [57]. All of the source code is opened in the GitHub<sup>1</sup> repository. The computer is equipped with

<sup>1</sup><https://github.com/kamenoseiji/PolariS>

the Intel Core-i5 CPU, 4-GB memory, NVIDIA GT640 GPU. It costs JPY 70,000.

### 4.2.1 Measurement of the Stokes Parameters

The PolariS produces power spectra of  $\langle XX^* \rangle$  and  $\langle YY^* \rangle$ , and cross power spectra of  $\langle XY^* \rangle$ . Full Stokes spectra of  $I$ ,  $Q$ ,  $U$ , and  $V$  are derived using the productions in offline.

If  $X$  and  $Y$  stand for linear polarizations without any cross talk between them, the Stokes parameters are derived using the equation:

$$\begin{pmatrix} I \\ Q \\ U \\ V \end{pmatrix} = \frac{1}{2} \begin{pmatrix} 1 & 0 & 0 & 1 \\ \cos 2\psi_m & -\sin 2\psi_m & -\sin 2\psi_m & -\cos 2\psi_m \\ \sin 2\psi_m & \cos 2\psi_m & \cos 2\psi_m & -\sin 2\psi_m \\ 0 & -i & i & 0 \end{pmatrix} \begin{pmatrix} \frac{\langle XX^* \rangle}{G_X G_X^*} \\ \frac{\langle XY^* \rangle}{G_X G_Y^*} \\ \frac{\langle YX^* \rangle}{G_Y G_X^*} \\ \frac{\langle YY^* \rangle}{G_Y G_Y^*} \end{pmatrix} \quad (4.2)$$

where  $\psi_m$  is the parallactic angle ( $\pm$  elevation angle for Nasmyth optics) and  $G_X, G_Y$  are the voltage-domain complex gain of the receiving system. This conversion is carried out with off-line reduction software.

In a practical receiving system precision, polarization measurements are difficult and require careful instrumental calibration. The measurements are affected by cross-talk, or leakage, between orthogonal polarisations and fluctuations in the complex gain of the receiving system (see chapter 3). Detailed calibration schemes for Stokes  $V$  is presented in chapter 5.

## 4.3 Verification

We have tested the following aspects of the PolariS performance: spectral resolution (subsection 4.3.1), linearity (subsection 4.3.2), stability (subsection 4.3.3), sensitivity (subsection 4.3.4), and cross-correlation capabilities (subsection 4.3.5). We used the Z45 receiver and the H22 receiver, working at 45 and 22 GHz, respectively, installed on the NRO 45-m telescope.

### 4.3.1 Spectral Resolution Function

The spectral resolution function is the response of the system to a monochromatic input. It demonstrates the sensitivity of the system as a function of frequency and is an indicator of the coupling between adjacent spectral channels (also known as spectral sidelobes).

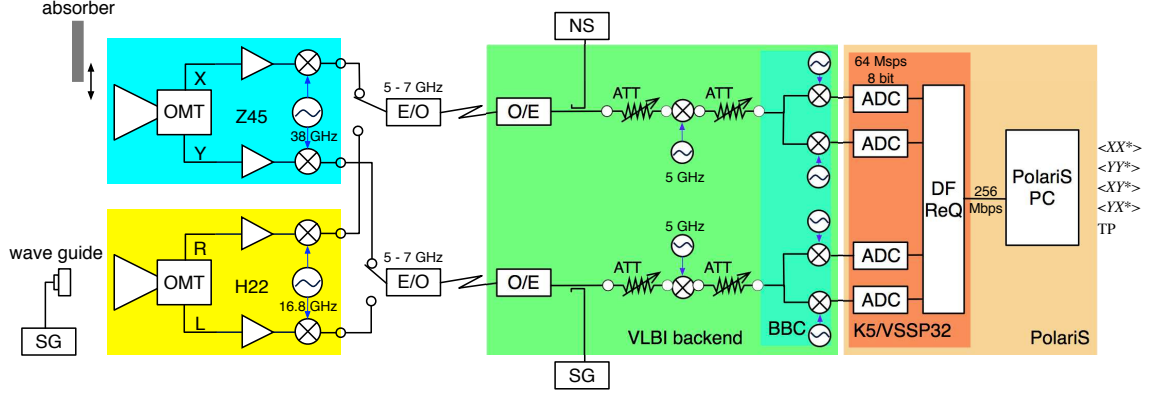


FIGURE 4.3: The verification configuration.

The PolariS receives baseband analog signals generated by the baseband converter (BBC) of the VLBI backend. Monochromatic wave generated by the signal generator (SG: Agilent E8257D) or white noise produced by the noise source (NS: NTK 9009ZR) were optionally coupled to measure the spectral resolution function and the linearity in line intensity and total power, respectively. Linear polarizations (X and Y) and circular polarizations (R and L) of the Z45 and H22 receivers, respectively, were selectively transmitted to the VLBI backend. An absorber was inserted on the feed horn of the Z45 receiver during noise temperature measurement. Linearly polarized monochromatic waves at 22 GHz were injected to the H22 receiver through the feed, generated with a signal generator (Agilent 83650L) and a transducer with a rectangular waveguide to verify the cross-correlation capability of the PolariS.

Any spectral feature measured by the spectrometer is the convolution of the true line shape and this spectral resolution function. The spectral resolution function of PolariS is determined by the FFT process where input data stream is truncated in finite-length segments. PolariS employs a rectangular window function. This makes the spectral response after FFT the Sinc function. Thus, the spectral resolution function formed by the cross-multiplication of these FFT products (see Fig. 4.2) will be a  $\text{Sinc}^2$  function with the FWHM of 0.886 channel (54.07 Hz for 8-MHz bandwidth). A desired apodization window function can be applied offline to reduce the spectral sidelobes. To minimize the information loss through the FFT process, we do not apply apodization in PolariS. We also employed a 50-% overlap of adjacent FFT segments to save sensitivity for very narrow spectral feature by keeping the number of correlation measurements at longer time lags [50].

We confirmed that the measured spectral resolution function is consistent with the theoretically expected one through the following tests, whose configuration is shown in Fig. 4.3. A monochromatic wave was generated by the signal generator (Agilent E8257D) and was injected to the PolariS. Its frequency was swept with a 4-Hz step over a 400-Hz range across the reference spectral channel at 68 MHz. Since the bandwidth of

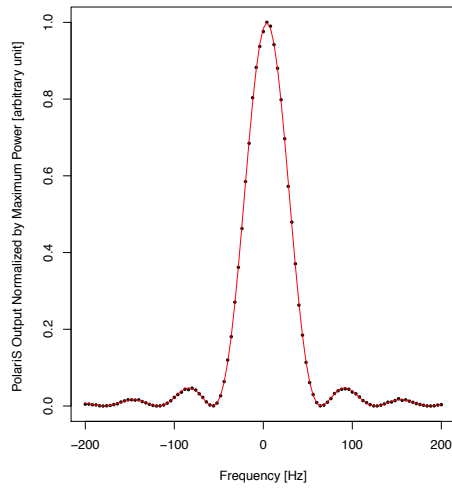


FIGURE 4.4: The spectral resolution of the PolariS. Measurements (dots) and best-fit  $\text{Sinc}^2$  curve with the FWHM of 54.02 Hz (solid line) are displayed.

the monochromatic wave was sufficiently narrow, the response to the reference channel as a function of the frequency separation expressed the spectral resolution function.

To characterize the measured spectral resolution function, we removed the continuum noise level determined by line-free channels. The calibrated power,  $P_{\text{ref}}$ , as a function of frequency separation of the monochromatic wave is shown in Fig. 4.4. We applied the least-squares fit with the  $\text{Sinc}^2$  function as  $P_{\text{ref}} \sim a_0 \left( \frac{\sin(\pi(a_1\nu - a_2))}{\pi(a_1\nu - a_2)} \right)^2$ , where  $a_0$ ,  $a_1$ , and  $a_2$  were free parameters that related to amplitude, resolution, and the center frequency, respectively. The best-fit  $\text{Sinc}^2$  function is displayed in the red line in Fig. 4.4. The results corresponded to the spectral resolution of  $\text{FWHM} = 54.02 \pm 0.06$  Hz, which is consistent with the ideal expectation.

### 4.3.2 Linearity

For an ideal spectrometer, the measurement values of spectral power must be proportional to the input power.

We verified the linearity performance in two aspects of measurements: the total power and the spectral line intensity. The former is required to measure system noise temperature and flux densities of continuum sources, while the latter is necessary to measure accurate line intensities and profiles.

#### 4.3.2.1 Line Intensity

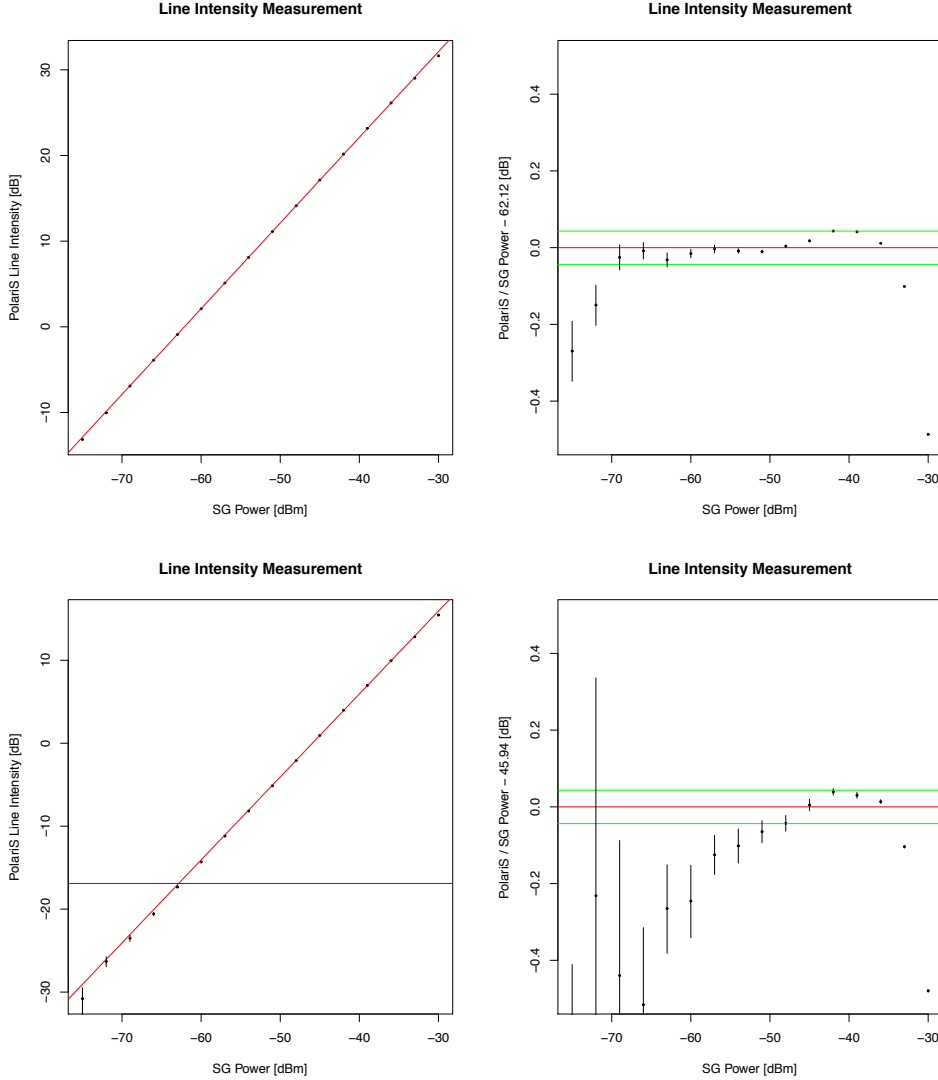


FIGURE 4.5: Linearity of PolariS for line observation.

Top and bottom panels stand for ‘high-power’ and ‘low-power’ injection of a monochromatic wave produced in the signal generator. The ‘low-power’ injection employs an additional 16-dB attenuator compared with the ‘high-power’ circumstance. (Left): Line strength measured by the PolariS as a function of input power (dots) and fitted result (red line). The blue horizontal line indicates the standard deviation of the system noise level. (Right): Departure from the linear regression (dots). Horizontal green lines indicate the  $\pm 1\%$  error range.

We used the Z45 receiver pointing to the blank sky and injected a monochromatic wave generated by the signal generator (Agilent E8257D) into the IF signals (see the configuration in Fig. 4.3) to simulate astronomical spectral-line observations. The frequency of the injected signal was fixed at 5449 MHz, corresponding to 1 MHz in the PolariS base band, and the signal power was changed between  $-30$  dBm and  $-75$  dBm with

a 3-dB step. To cover a wider power range, we used two additional attenuators of 20 dB ('high power') and 36 dB ('low power') for the injected waves. We set the PolariS at the 4-MHz bandwidth, 8-bit quantization and 65536-channel mode. To measure the line power, we integrated the acquired spectrum for 60 sec at each SG power level and subtracted the continuum baseline as well as the verification of the spectral resolution function (section 4.3.1). The line power at the reference channel ( $P_{\text{ref}}$ ) was compared with the power of injected monochromatic wave,  $P_{\text{in}}$ .

Fig. 4.5 shows the results, together with the linear regression of  $P_{\text{ref}} = bP_{\text{sg}}$ , where  $b$  is the proportional coefficient. The proportional coefficients at 'high-power' and 'low-power' circumstances were 62.12 dB and 45.94 dB, respectively. The residuals from the linear regression,  $\frac{P_{\text{ref}} - bP_{\text{in}}}{bP_{\text{in}}}$ , are also displayed in Fig. 4.5. The results indicated that the departure from the linear regression was less than 1% within the power range of 33 dB and 12 dB in 'high-power' and 'low-power' circumstances, respectively.

#### 4.3.2.2 Total Power

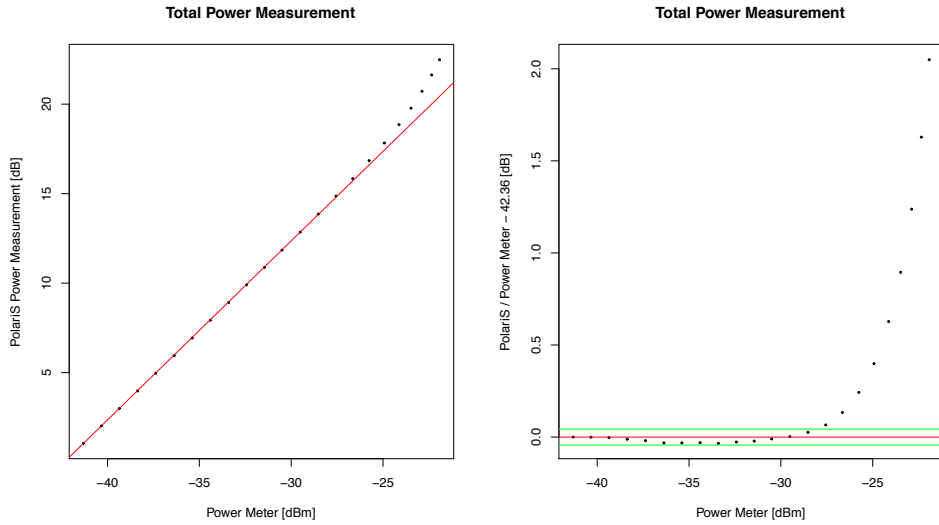


FIGURE 4.6: Linearity of PolariS for continuum observation.  
(left) Power measured by the PolariS as a function of input power. (right) Departure from the linear trend. Green horizontal lines indicate the  $\pm 1\%$  error range.

To verify the linearity of total power measurements, we injected the white noise generated by the noise source (NTK 9009ZR) and adjusted the power level using a combination of two step attenuators (ATTs) covering a 22-dB range by a 1-dB step. We employed the power measurement scheme using the bit distribution of digitized signals in the analog-to-digital converter [35]. The input analog power was monitored using the power meter

(HP E4419A) with the power sensor (HP 8481D). The test configuration is shown in Fig. 4.3.

The measurement results are shown in Fig. 4.6 together with the linear regression of  $\log P_{\text{PolariS}} \sim \log P_{\text{in}} + c$ , where  $c$  is the sensitivity coefficient that corresponded to 42.46 dB. Relative departure from the linear regression,  $\frac{\log P_{\text{PolariS}} - (\log P_{\text{in}} + c)}{\log P_{\text{in}} + c}$ , was within 1% in the range of  $> 13$  dB.

### 4.3.3 Stability

Time stability in sensitivity is required for accurate measurements in radio astronomy observations that take a long integration time. Instability of a spectrometer can cause systematic errors when scans for calibrator and target sources are not simultaneous. In the case of radio spectroscopy, a spectrum acquired toward the blank sky (off-source) is used to calibrate the bandpass shape and to subtract the system noise [57]. Stability of the bandpass shape is essential for weak-spectral-line detectability.

To evaluate the bandpass stability, we measured the time-based Allan variance (TAV) and estimated the stable timescale. We employed the SBC (Smoothed Bandpass Calibration) method [57] to distinguish the systematic bandpass variation from random noise. The spectral-smoothing window was determined by the spectral flatness evaluated using the spectral Allan variance (SAV).

To evaluate the TAV and SAV, we conducted spectroscopy of the noise-source signals for 54000 s. The configuration is shown in Fig. 4.3. Note that the measured instability involves not only PolariS but also the whole system.

#### 4.3.3.1 Time-based Allan Variance (TAV)

For the evaluation of time stability, we calculated the TAV,  $\sigma_y^2(\tau)$  at the reference spectral channel near the band center, as a function of time lag,  $\tau$ , defined as:

$$\sigma_y^2(\tau) = \frac{\langle [P_{\text{ref}}(t + \tau) - 2P_{\text{ref}}(t) + P_{\text{ref}}(t - \tau)]^2 \rangle}{2\tau^2}. \quad (4.3)$$

The TAV will follow  $\sigma_y^2(\tau) \propto \tau^{-2}$  while the systematic variation is not significant compared with the white random noise. We defined the timescale of stability when the excess of  $\sigma_y^2(\tau)$  from the  $\propto \tau^{-2}$  relation is identical to the expectation.

Fig. 4.7 shows the total power variation and the TAV measurement. The total power in the first 1000 s gradually increased. The variation can be ascribed to warming up of the

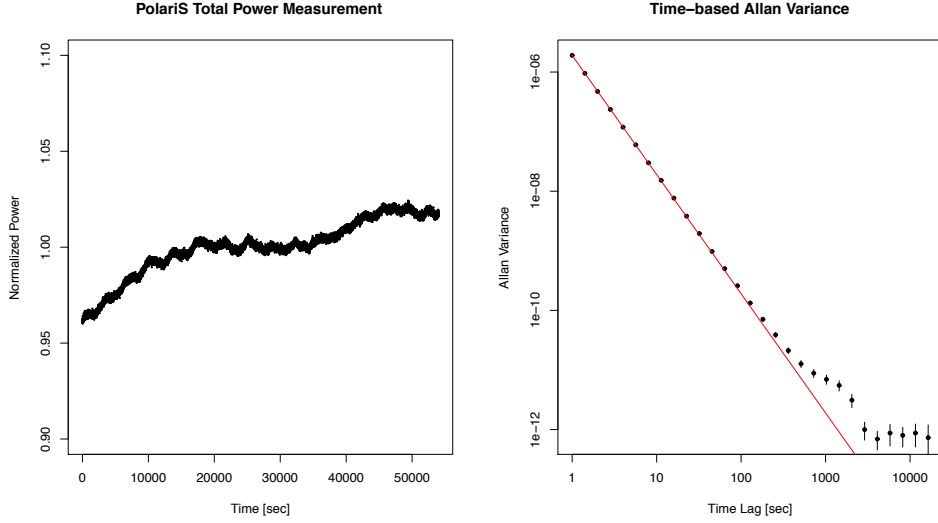


FIGURE 4.7: Total power variation and the time-based allan variance.

(Left): Time variation of the total power measured by the histogram of digitized signals for 54000 s with a 1-s time resolution. The total power was scaled by the mean value. (Right): Time-based Allan variance (TAV) of the total power measurement. The red solid line indicates the power law with the power index of  $-2$ , expected for white noise. The departure of TAV from the power law became significant at the time lag  $\geq 512$  s.

noise source. The TAV followed the  $\propto \tau^{-2}$  relation for  $\tau \leq 256$  s and the timescale of stability was 512 s. Note that the TAV included not only variations of PolariS but also the analog devices such as the noise source, the IF downconverter, and the baseband converter. The stability of solo PolariS must be better than the measured TAV.

#### 4.3.3.2 Bandpass stability

The stability of bandpass shape was examined with the same configuration of the TAV, shown in Fig.4.3. The overall bandpass table,  $H(\nu)$  was obtained by integrating the spectrum for 54000 s and then applying spline smoothing with a 128-ch width except for 6% band edges at both ends as shown the red line in Fig. 4.9. Time series of 1800-s integrated bandpass variation,  $\hat{H}_k(\nu) = \frac{H_k(\nu)}{G_k H(\nu)}$ , were shown in Fig. 4.8 to evaluate the bandpass stability. Here,  $k = 1 \dots 30$  is the index of 1800-s integration periods, and  $G_k$  is the gain table obtained by 1800-s integration of the total power,  $P_{\text{Polaris}}$ . To reduce random error in the bandpass variation, we averaged  $\hat{H}_k(\nu)$  for 256 spectral channels (15.625 kHz). The mean and standard deviation (SD) values of each bandpass variation are attached in Fig. 4.8 and their time variation are plotted in Fig. 4.9.

We did not find any significant systematic variation of the bandpass shape which exceeded the random-noise SD which was expected as  $\frac{1}{\sqrt{\Delta\nu T}} = 2.6 \times 10^{-4}$ .

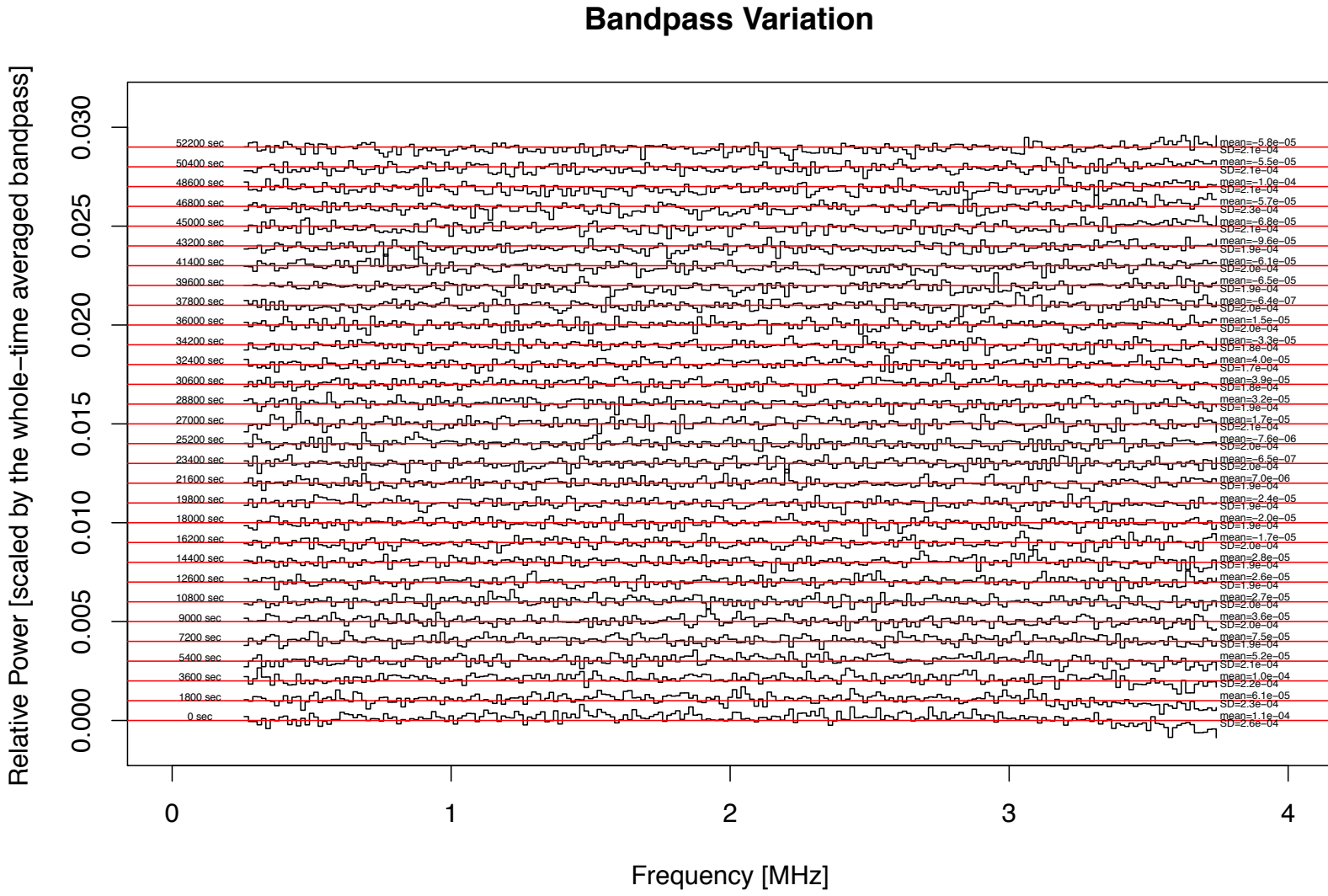


FIGURE 4.8: Time variation of bandpass shape.

The series of bandpass-corrected spectra,  $\hat{H}_k(\nu)$  ( $k = 1 \dots 30$ ), are plotted with the offset baselines by the red horizontal lines. The scale of the vertical axis is relative to the 54000-s averaged bandpass,  $H(\nu)$ . Relative time from the start is labeled at the left of each spectrum, together with the mean and SD values at the right.

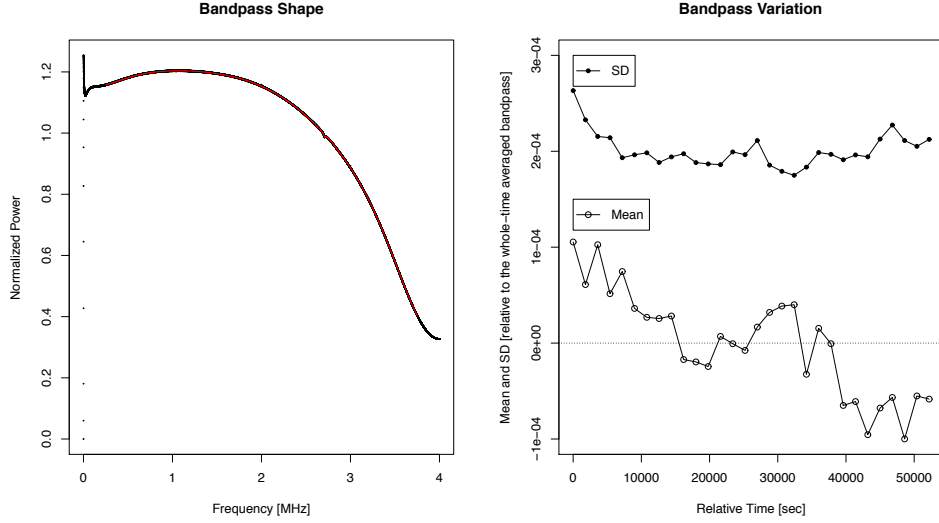


FIGURE 4.9: Whole 54000-s integrated bandpass, and variation of mean and SD values of 1800-s integrated bandpass.

(Left): Whole-bandwidth spectrum integrated for 54000 s. The red solid line indicates spline-smoothed bandpass shape without 6% band edges at both ends. (Right): Mean and SD values of calibrated spectra shown in figure 8, as a function of relative time from the start.

We found a decline of the mean value through the entire period in Fig. 4.9, and will discuss about it in section 4.5.

#### 4.3.3.3 Spectral Allan Variance (SAV)

The spectral Allan variance, SAV, defined by equation 4.4, is an indicator of bandpass flatness as a function of frequency separation,  $\Delta\nu$ .

$$\sigma_y^2(\Delta\nu) = \frac{\langle [H(\nu + \Delta\nu) - 2H(\nu) + H(\nu - \Delta\nu)]^2 \rangle}{2\Delta\nu^2}. \quad (4.4)$$

While a spectrum is dominated by white noise, the SAV is given by the SD of bandpass-corrected spectrum,  $\sigma = \sqrt{\langle H^2(\nu) \rangle - \langle H(\nu) \rangle^2}$ , and the frequency separation as  $\sigma_y^2(\Delta\nu) = \frac{3\sigma^2}{\Delta\nu^2}$  and it follows the power law of the frequency separation with the power index of  $-2$ . When systematic distortion of the bandpass shape exceeds the white noise, on the other hand, the SAV shows a greater power index than  $-2$ .

Fig. 4.10 (right) shows the SAVs, together with corresponding bandpass shapes (left). With a short integration time (1 s), the SAV was dominated by white noise and showed the power index of  $-2$ . The overall SAV got reduced after 1800-s integration. The systematic bandpass shape significantly appeared at  $\Delta\nu \geq 4$  ch and became dominant at

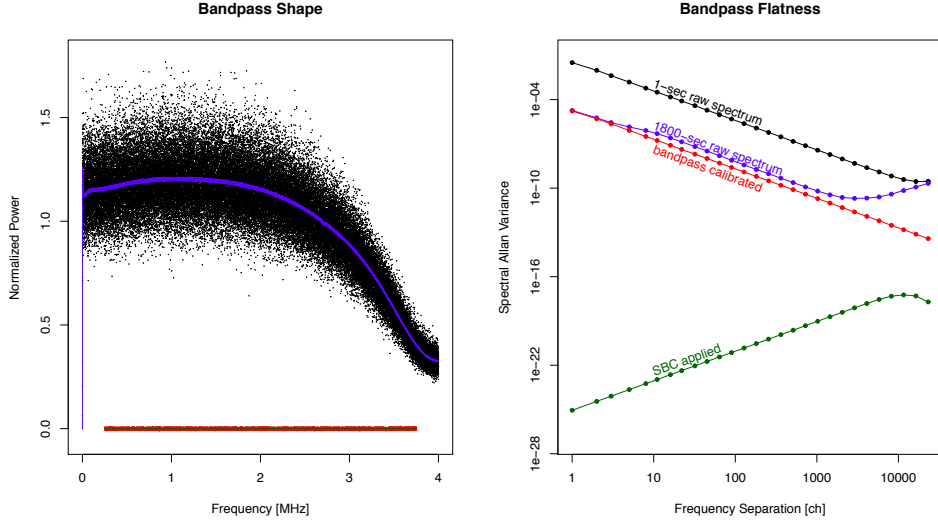


FIGURE 4.10: Bandpass shapes and the spectral Allan variances.

(Left): Bandpass shapes. Black and blue dots indicate the raw spectra with time integration of 1 s and 1800 s, respectively. The red dots indicate the bandpass-calibrated spectrum. Application of the smoothed bandpass calibration (SBC) is plotted in the green line. (Right): Spectral Allan variances (SAVs). Color indices are the same with the spectra in the left panel.

$\Delta\nu \geq 2048$  ch. The systematic component eliminated from the SAV after bandpass calibration was applied. The random noise component in the bandpass-calibrated spectrum was efficiently reduced by applying the SBC.

#### 4.3.4 Sensitivity

The sensitivity of a spectrometer is determined by the standard deviation (SD) of flux densities in line-free spectral channels measured after bandpass calibration and system-noise subtraction because detection of emission (or absorption) lines is judged by the signal-to-noise ratio (SNR), which is the ratio of line intensity to the SD. When the SD is dominated by random noise, the SD will be reduced by long time integration as  $\sigma(T) \propto T^{-1/2}$ , where  $\sigma$  is the SD with respect to the system noise and  $T$  is the integration time.

To evaluate the sensitivity, we used the same dataset for the SAV, bandpass stability, and TAV evaluations and measured the SD using the PolariS for time integration up to 54000 s. The bandpass calibration table was generated from the spectrum integrated for 1800 s and applied the SBC. The SD of the spectrum was calculated in the frequency range of 1 – 2 MHz where the bandpass shape was flat and no significant spurious signals were detected.

Fig. 4.11 shows the results of the measurements. The SD at 1-s integration, scaled by the system noise, was 0.110, which was 13.8% as small as the theoretical value of  $\sigma = \frac{1}{\sqrt{\Delta\nu T}}$ . At 54000-s integration, the SD decreased down to  $4.82 \times 10^{-4}$  which was still 12.5% as small as the theoretical expectation. If we use the SD at 1 s as the reference (see the right of Fig. 4.11), the SD follows the  $\propto T^{-1/2}$  law up to the integration of 18000 s. within 1% excess.

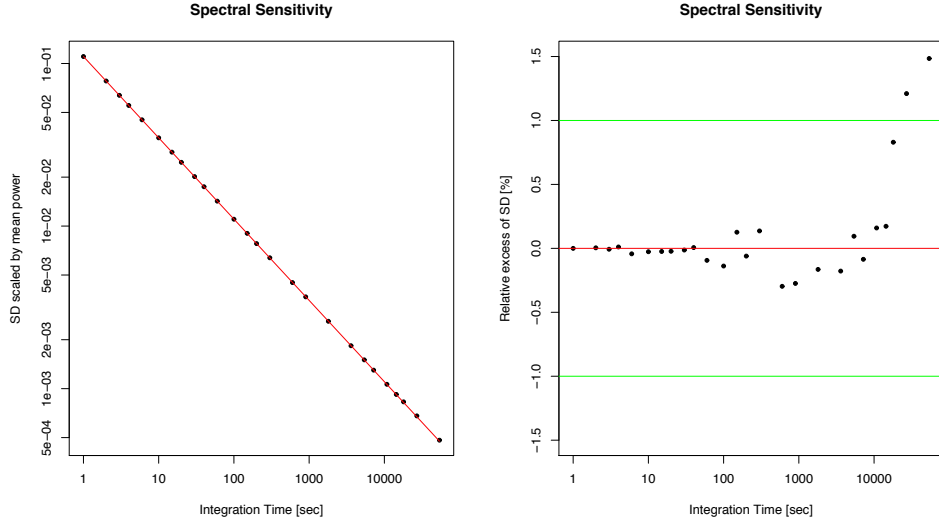


FIGURE 4.11: Variation of the root-mean-square with integration time.

(Left): The root-mean-square (RMS) of bandpass-corrected spectra in the frequency range of 1 – 2 MHz with various integration time,  $T$ , ranged 1 – 54000 s. The red solid line indicates extrapolation from the RMS at 1 s with the  $\propto 1/\sqrt{T}$  law. (Right): Relative excess of the RMS from the  $\propto 1/\sqrt{T}$  law. The green horizontal lines indicate  $\pm 1\%$  range from the expectation.

#### 4.3.5 Cross-correlation

The cross-correlation function between two orthogonal polarizations is necessary to obtain full Stokes spectra, as stated in section 4.2.1. To verify the cross products of the PolariS, we used the H22 dual circular polarization receiver and injected a linearly polarized monochromatic wave at 22.233 GHz through the feed, generated with a signal generator (Agilent 83650L) and a transducer with a rectangular waveguide. The received two circular polarization signals which must correlate each other were transmitted to the VLBI backend, and acquired with the PolariS. The whole configuration is shown in Fig. 4.3. The cross-correlation products of the PolariS were tested in terms of the correlation coefficient and relative phase for 94 s with the time resolution of 1 s. The results are shown in Fig. 4.12. The correlation coefficient was  $97.6 \pm 0.2\%$  and the standard

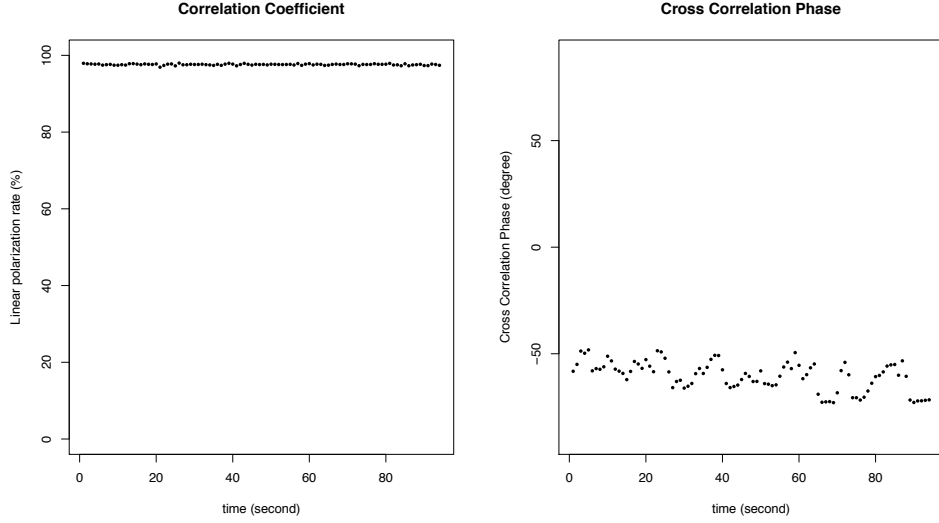


FIGURE 4.12: Variation of correlation coefficients and the phase taken by the PolariS. (Left): Correlation coefficient between two circular polarization signals. The input signal was the linearly polarized monochromatic wave, which was expected to perfectly correlate. (Right): Phases of the correlation function, which corresponds to relative phase between two circular polarization signals. The standard deviation of the phase was  $-60^\circ.4 \pm 6^\circ.8$ .

deviation of phase was  $6.8^\circ$  during the observation of 94 s. We discuss the reason why the correlation differs from 100% in section 4.5.

#### 4.4 Field Test Observations

For the purpose of commissioning and science verification, we tried test observations of SiO maser lines toward the Mira variable star, R Leo, and the CCS molecular line toward the star-forming molecular core in the Taurus Molecular Cloud 1 (TMC-1) using the Z45 receiver on the Nobeyama 45-m radio telescope.

For R Leo, two transitions of SiO  $J = 1 - 0$ ,  $v = 1$  (43.122 GHz) and  $v = 2$  (42.821 GHz) were simultaneously observed with the dual linear polarizations on March 16, 2014. Spectroscopy was originally carried out with 16384 channels across 4-MHz bandwidth (244-Hz resolution) and bunched into 3.9-kHz resolution. The integration time for on- and off-source were 41 s and 65 s, respectively, and the off-source spectra were subtracted from the on-source ones. The power spectra and cross power spectra are shown in Fig. 4.13. The power spectra of  $\langle XX^* \rangle$  and  $\langle YY^* \rangle$  were significantly different and the cross power spectra were significantly detected.

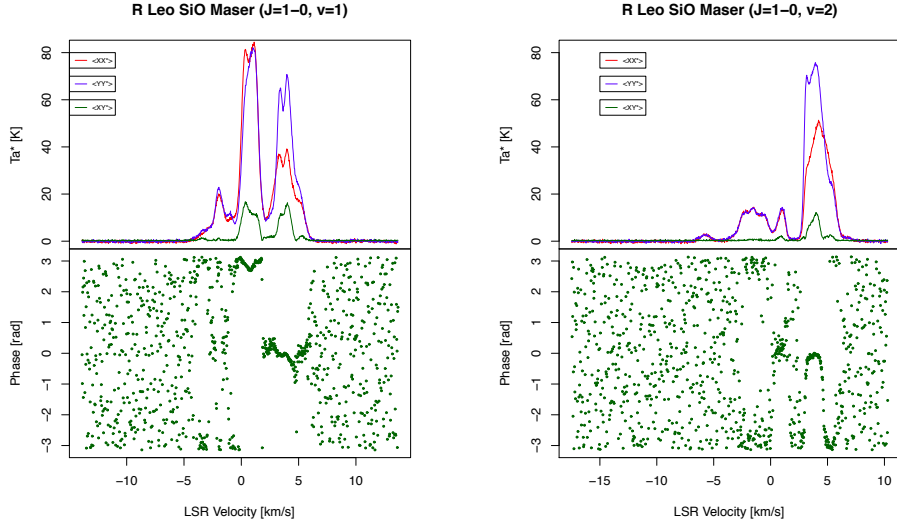


FIGURE 4.13: Power spectra and cross power spectra of SiO maser ( $J = 1 - 0$ ) emission lines toward R Leo.

Left and right panels indicate the vibration state of  $v = 1$  and  $v = 2$  at 43.122 and 42.821 GHz, respectively. Red and blue solid lines in the top stand for the power spectra of  $X$  and  $Y$  linear feeds, respectively. Green solid line and filled circles indicate the amplitude and phase of the cross power spectrum between  $X$  and  $Y$  polarizations.

For the TMC-1, the CCS  $J_N = 4_3 - 3_2$  transition at 45.379 GHz was observed on December 23, 2013. We pointed to  $(\text{RA}, \text{DEC})_{\text{J}2000} = (04^h 41^m 42^s.47, +25^\circ 41' 27''.1)$ , which was close to ‘b7’ clump of TMC-1 core D region [38]. Spectroscopy with integration of 252 s and 375 s for on- and off-source was carried out with 131072 channels across 8-MHz bandwidth (61-Hz resolution) and bunched into 1.95-kHz resolution. Since a relatively strong spurious signal appeared in one spectral channel near the center of CCS line profile, we flagged the channel before bunching. The power spectra and cross power spectra are shown in Fig. 4.14.

## 4.5 Discussion

The engineering tests of the PolariS presented here demonstrate compliance with specifications

The spectral resolution perfectly coincided with the theoretical expectation, as shown in section 4.3.1. The current software employs the boxcar window function in the time-domain FFT segments, which result in a  $\text{Sinc}^2$  spectral resolution function. This treatment causes subtle sidelobe associated with narrow and strong emission lines. PolariS is a software spectrometer, which is flexible for applying other window functions, such as Hamming, Hanning, and Blackman windows, to reduce sidelobe levels in the spectral

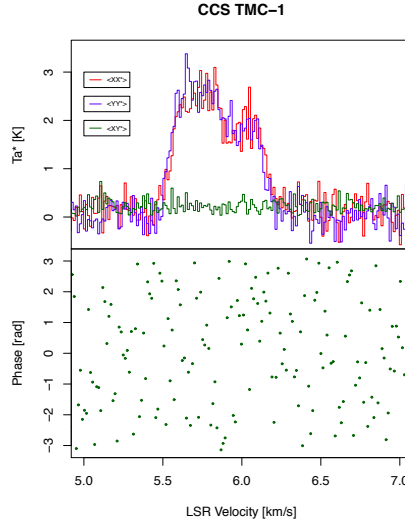


FIGURE 4.14: Power spectra and cross power spectra of CCS emission line toward TMC-1 at the spectral resolution of 1.95 kHz.

Color assignments are the same with Fig. 4.13.

resolution function. However, we keep the boxcar window, because sidelobe mitigation with a relevant window function can be applied in post processing. Observers can apply desired apodization function or spectral bunching to reduce spectral sidelobes.

The system showed linearity in total power measurements to within 1% over an input power range of 13dB. The total power measurement is used to estimate the receiver noise temperature and the system noise temperature by comparing powers in two or more circumstances where the feed horn points to the absorber at ambient temperature ( $\sim 293$  K), to the cold load ( $\sim 77$  K), and to the blank sky ( $\sim 20$  K). Since the typical receiver noise of the Z45 is  $\sim 50$  K, the power range between the cold load, the blank sky and the ambient load will be  $\frac{293 + 50}{77 + 50} = 2.7$  (4.3 dB) and  $\frac{293 + 50}{20 + 50} = 4.9$  (6.9 dB). Thus, the dynamic range of  $> 13$  dB is sufficient for the system noise measurement, if we set the power level adequately. The power meter we employed for this experiment has a maximum rated input power of  $-20$  dBm. We note that the departure from linearity displayed in Fig. 4.6 could therefore in part be due to saturation of the power meter, and that the linear range of the PolariS system could be wider than presented here.

The dynamic range of 33 dB in line intensity is also enough for astronomical spectroscopy. The departure from the linear trend in high-power ends can be ascribed to inaccuracy of the signal generator, because the sensitivity profiles above  $-40$  dBm are very similar in both ‘high-power’ and ‘low-power’. The underestimation in low-power ends, especially in the ‘low-power’ attenuator setting can be caused by uncertainty in baseline subtraction because the departure from the linear trend was significant where the line intensity is

identical to the standard deviation ( $= \frac{1}{\sqrt{\Delta\nu T}}$ ) of the system noise. The performance of weak line detectability is verified with the SD of the spectrum at long integration time. As is shown in section 4.3.4, the sensitivity is ideally maintained for the timescale of 54000 s. The field-test observations of CCS molecular line toward TMC-1 also indicate that the system shows no significant departure in the linearity range down to  $T_a^*/T_{\text{sys}} = 1.7\%$ .

As shown in subsection 4.3.3, the bandpass shape is very smooth and stable, allowing us to apply SBC to reduce off-source scans efficiently. This indicates that the analog system (baseband converters and analog-to-digital converter) performs sufficiently stably and the digital system (in software) works perfectly. The SAV (see Fig. 4.10) indicates a very good flatness in the bandpass-corrected spectrum. The systematic error of bandpass shape after SBC application will be less than  $\sqrt{\frac{2\Delta\nu^2 \text{SAV}}{3}} = 2.3 \times 10^{-5}$  at the maximum channel separation of 11585 ch for broad line detection, even if we employ a single bandpass table for 15-hour observations.

The mean values of the bandpass-corrected spectra were decreasing while the increasing total power (see Fig. 4.7). We consider that this is ascribed to increase of power in band edges caused by bandpass distortion. Because the gain table,  $G(t)$ , is derived from bit distribution that includes power in band edges, increase of power in band edges makes  $G(t)$  greater and lets the mean power without band edges decreased after gain calibration. We can also see convex and concave distortion at the beginning and ending periods, respectively, in Fig. 4.8. This behavior supports the explanation above.

The stability in bandpass shape is also confirmed by the sensitivity shown in subsection 4.3.4. As shown in Fig. 4.11, the SD of bandpass-corrected spectra follows the  $\propto T^{-1/2}$  law for the integration time shorter than 18000 s. The excess of SD at the longest integration time can be caused by the bandpass error, related with variation in total power as discussed in the last paragraph, because the distortion of bandpass shape after SBC is estimated to  $\sim 10^{-5}$  and non-negligible for integration longer than 18000 s. Note that the SD value at the longest integration time is still smaller than the expectation of  $\frac{1}{\sqrt{\Delta\nu T}}$ . This is probably because the effective bandwidth is narrower than 4 MHz due to the antialias filter (see Fig. 4.10) and thus the sampling frequency of 8 MHz is slightly higher than the Nyquist rate.

The cross-correlation capability is confirmed by the engineering test with the artificial source (subsection 4.3.5) and the field test (subsection 4.4). With the injection of the linearly polarized artificial monochromatic wave into a dual circular feed, we got  $97.6 \pm 0.2$  % of correlation. The departure from 100 % could be due to system noise that yields

relative phase fluctuation between LHCP and RHCP caused by differences in signal path taken by the two polarisations.

The measured cross power spectra of the SiO maser in the observation toward R Leo (see Fig. 4.13) demonstrates the potential of this instrument to perform high precision polarimetric observations. In both  $v = 1$  and  $v = 2$  transitions, the velocity components within  $0 \leq V_{\text{LSR}} \leq 7 \text{ km s}^{-1}$  shows highly polarized emission with a significant amplitude in cross power spectra, small phase dispersion, and difference between  $\langle XX^* \rangle$  and  $\langle YY^* \rangle$  spectra. The large gap in phase between velocity components of  $0 \leq V_{\text{LSR}} \leq 2 \text{ km s}^{-1}$  and  $2 \leq V_{\text{LSR}} \leq 7 \text{ km s}^{-1}$  in  $v = 1$  suggests that the EVPAs (electric vector position angles) are significantly different between these two components. The blueshifted components in  $-7 \leq V_{\text{LSR}} \leq 0 \text{ km s}^{-1}$  show much weaker polarization than the redshifted components.

The CCS molecular emission is expected to be unpolarized, because it is a thermal emission in the dark cloud. No significant detection in cross power spectrum and no significant difference between  $\langle XX^* \rangle$  and  $\langle YY^* \rangle$  spectra (see Fig. 4.14) are consistent with this expectation. The phases of the cross power spectra, randomly distributed in  $[-\pi, \pi]$ , also suggest non-detection. Note that the amplitude of cross power spectrum is biased from 0, because it is always positive and follows the Rayleigh distribution when the expectation of cross power spectrum is 0. The line peak intensity of  $T^*a = 2.57 \pm 0.04 \text{ K}$  with 1.95-kHz resolution is slightly higher than the results of  $T^*a = 2.23 \pm 0.09 \text{ K}$  with 37-kHz resolution using the acousto-optical spectrometer (AOS) on the Nobeyama 45-m radio telescope. If we apply spectral bunching to set the same spectral resolution of 37 kHz, the PolariS spectrum results in  $T^*a = 2.47 \pm 0.04 \text{ K}$  and close to the AOS measurement. The line profile from the mapping observation of TMC-1 [38] showed a somewhat different profile, depending on the position of the molecular cloud. Because of the difference of beam size and pointing position, it is difficult to evaluate the difference of line profiles.

## 4.6 Summary

We have developed a software-based polarization spectrometer, ‘PolariS’ using commercial-based devices of the K5/VSSP32 digitizer and the Linux computer, at the cost of JPY 500,000 and JPY 70,000, respectively. Using the GPU for FFT and cross-correlation processes, spectroscopy for 4-IF 4- or 8-MHz bandwidth with a 61-Hz spectral resolution can be carried out in real time.

Through the engineering tests, we have verified the basic performance of the PolariS. The spectral resolution function was consistent with the theoretical prediction of Sinc<sup>2</sup> profile with a FWHM of  $54.02 \pm 0.06$  Hz. The linearity between input signal power and measured power has been confirmed within 1% accuracy for the range of  $> 13$  dB and 33 dB for continuum total power and emission line, respectively. The bandpass shape was flat and stable enough to apply SBC with 125-kHz frequency width. No significant bandpass variation exceeding  $2.6 \times 10^{-4}$  with respect to the system noise was found for the time span of 15 hours. The standard deviation of the spectrum was 12.5% as small as the expectation of  $\frac{1}{\sqrt{\Delta\nu T}}$  at 54000-s integration and follows the  $\propto T^{-1/2}$  law between 1 s and 54000 s. The cross power spectra were verified by injection of a linearly polarized artificial signals into a dual circular feed and their cross-correlation of them.

The field test observations were carried out toward the strongly polarized maser source, R Leo, and unpolarized CCS emission of TMC-1. We verified the performance of the power spectra that will yield full Stokes spectra crucial to our primary aim of the Zeeman effect measurements.

All the PolariS software code is open in the GitHub repository and anyone can download and use it or review the signal processing inside.

## Chapter 5

# Polarization calibration for Stokes V measurement

### Abstract

We have developed polarimetry device to estimate a magnetic field strength of pre star-forming cores using Zeeman shift measurement in CCS molecules at the Nobeyama 45m radio telescope. The science goal is to measure  $100 \mu\text{G}$  magnetic field with a accuracy of  $5\sigma$  and to achieve the goal we need to measure of 64 Hz Zeeman shift in Stokes  $V$  with a r.m.s. noise level of 12.8 Hz. Our polarimetry device consists of PolariS and Z45 receiver. We examined following 3 aspects to mesure the Stokes  $V$  through observations; (1) the instrumental configuration, (2) instrumental phases in cross correlation and (3) a D-term effect. We could estimate (1) and (2), and we applied to Stokes parameter determination. We could estimate an upper limit of the calibration value of (3). Additionally we observed a pre star-forming core toward TMC-1 in the CCS molecular line to detect the Zeeman shift for 7 hours observations. The result is  $-68.0 \pm 35.4$  Hz which indicate an observation time of 54 hours to achieve 12.8 Hz rms level.

### 5.1 Introduction

To mesure magnetic fields using Zeeman shift measurement in CCS molecules are important to examine a role of magnetic field in star-formation. However it has not been measured yet. Our research aim is to estimate  $100\mu\text{G}$  magnetic field with a accuracy of  $5\sigma$  and to achieve the goal we need to measure of 64 Hz Zeeman shift in Stokes  $V$  with

the rms noise level of 12.8 Hz (see Chapter 1). To measure the Zeeman shifts, we need to measure Stokes  $V$  with high sensitivity and high spectral resolution ( $< 64$  Hz). A linear reception is desirable to accurate Stokes  $V$  measurement (see section 3.5). And we can spatially resolve pre star-forming cores in nearby star forming regions at 45 GHz using the NRO 45m (Nobeyama Radio Observatory 45m telescope) [33]. Hence we installed a polarimetry device consist of Z45 and Polaris with linear reception, high resolution (61 Hz) and 45 GHz band at the NRO 45m.

To estimate Stokes  $V$ , We need calibrations of (1) instrumental phases in cross correlation and (2) a D-term effect. Calibration schemes of linear polarization reception is introduced in [54]. They showed configurations of the estimation and calibrators; (1) and (2) calibrate using an artificial linearly polarized continuum source using a wire grid and an unpolarized source, respectively. However the theory and method of these calibrations are not written clearly and thus we clarified it and estimated these values.

In this chapter, we aim to show the configuration of the polarization device, the calibration results and a performance. Firstly, we summarize the configurations. Secondly we show configuration verifications using SiO maser observations. Thirdly we show the calibrations; (1) the instrumental phase and (2) the D-term effect. Finally we discuss a capability to the Zeeman shift measurements using TMC-1 (Taurus Molecular Cloud-1) observations.

## 5.2 Schematic view of the system

### 5.2.1 Signal processing

We show a schematic view of our polarimetry device in Fig. 5.1. Each processer in the device refers stable hydrogen maser clock. The signal processing flow is as follow.

1. Radio signals are collected at the dish and are propagated to Z45 receiver though Nasmyth optics with mirrors [31].
2. In Z45 receiver the signals are separated two linear polarizations; we denote the polarizations as H and V. The separated polarizations are amplified and down converted individually on Z45 receiver; the Lo (local) signal for downconversion (Lo1) is controlled by COSMOS which is the NRO 45m control system and continually vary during observation to remove doppler effect (e.g orbital motion, rotation of the earth).

3. The polarizations are transported across optical fiber cables into a observation building using E/O (electric optical) and O/E (optical to electric) converter in 7752TX.
4. The downconverter (7631B) convert the polarizations with Lo signals (Lo2, Lo3) of 5 GHz.
5. In 7641B, the polarizations (H and V) are divided into two signals. Here after we denote these divided signals as  $H_0$  and,  $H_1$  for H polarization, and  $V_0$  and  $V_1$  for V polarization. They are same frequency range and four signals are downconverted individually with four Lo signals (Lo4, Lo5, Lo6, Lo7 for  $H_0$ ,  $H_1$ ,  $V_0$ ,  $V_1$ , respectively); we set Lo4 and Lo6 are same frequency, and Lo5 and Lo7 are same frequency. And then the four signals are through bandpass filters of 0–4 MHz, individually.
6. Each analog signal is converted to digital signal in K5VSSP32, and then auto correlation of 4 signals ( $H_0H_0^*$ ,  $H_1H_1^*$ ,  $V_0V_0^*$ ,  $V_1V_1^*$ ) and two cross correlation of  $H_0$  and  $V_0$  ( $H_0V_0^*$ ),  $H_1$  and  $V_1$  ( $H_1V_1^*$ ) are calculated in PolariS. Auto correlation spectra for  $H_0H_0^*$ ,  $H_1H_1^*$ ,  $V_0V_0^*$  and  $V_1V_1^*$  are recorded in files named A00, A01, A02 and A03, respectively. Cross correlation spectra for  $H_0V_0^*$  and  $H_1V_1^*$  are recorded in files named C00 and C01, respectively. We denote the signal pass for  $H_0$ ,  $V_0$  is IF0 and for  $H_1$ ,  $V_1$  is IF1.

### 5.2.2 Observation method using our polarimetry device at the NRO 45m

To analyze data, we need the antenna status for example when is at ON and OFF positions. However the current PolariS output contain only time and signal information (auto- and cross- correlation spectra and bit distribution) because PolariS isn't connected to COSMOS [28] (see Fig.5.2). The output data of SAM45 [20] which is a digital spectrometer at the NRO 45m contains the antenna status and spectra, and Z45 can simultaneously output to the PolariS and SAM45. Since we use two spectrometers, SAM45 and PolariS, simultaneously and we combine the status from SAM45 and data from PolariS in off line (see Fig. 5.2).

## 5.3 Verification of instrumental configuration

We matched observation data to components of Stokes paramater formula in equation A.1,  $\xi$ ,  $E_x$ ,  $E_y$ , to measure the Stokes parameters. If we mistakably label observed

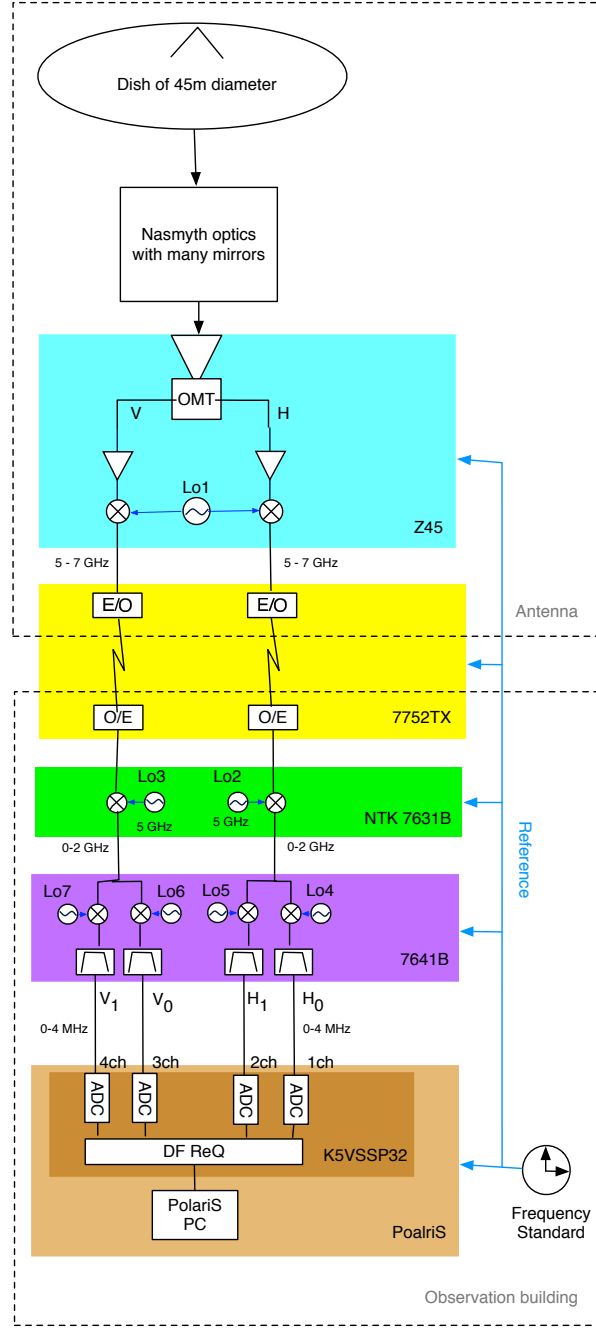


FIGURE 5.1: Schematic view of our polarimetry device

two linear polarization to  $E_x$ ,  $E_y$ , Stokes  $V$  will be obtained in a reverse sign. The NRO 45m is Nasmyth optics so  $\xi$ , which the angle between the celestial north and the receiver axis, is depends on  $EL$  (elevation angle),  $PA$  (parallactic angle), and  $RA$  (receiver angle which is defined as the angle between receiver coordinates and horizontal coordinates);  $\xi = EL + PA + RA$  or  $\xi = EL - PA + RA$ . The calibration angle  $EL + PA + RA$  or  $EL - PA + RA$  is dependent on the optics configuration. The optics of the NRO 45m is complex, so we need to verify it.  $EL$  and  $PA$  vary during an observation and

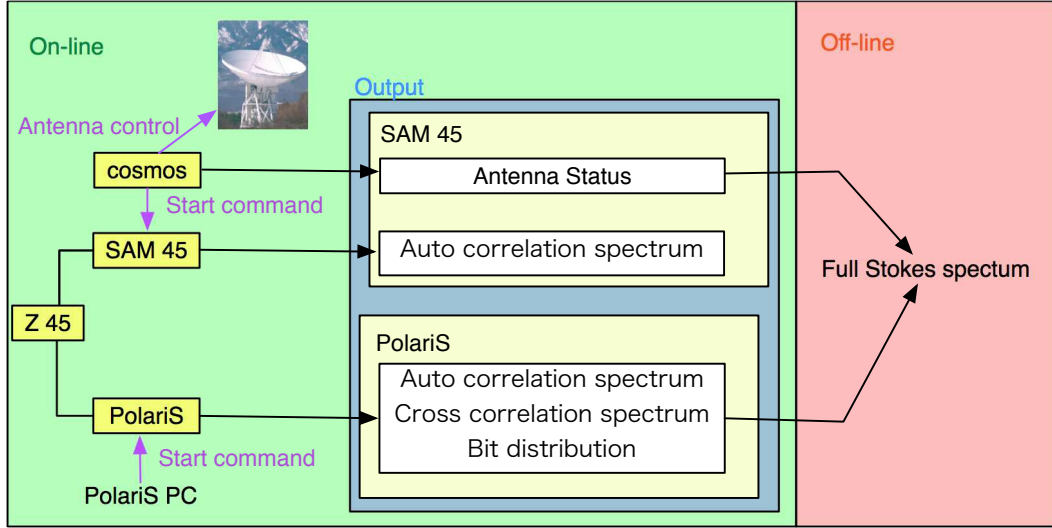


FIGURE 5.2: Observation flow using PolariS at the NRO 45m

$RA$  is constant. Therefore, if we observe a linearly polarized source without correction for  $\xi$ , the polarization angle will rotate smoothly with  $-\xi$  which is  $-(EL + PA)$  or  $-(EL - PA)$ . Then, we observed a strongly polarized source, SiO maser, and then we verified it.  $RA$  was estimated using observations of Crab Nebula which is the linearly polarized source known a polarization angle in section A.2.

### 5.3.1 Observations

We observed the SiO maser line at 43.12 GHz ( $v=1$ ) toward NML-Tau four times on April 17, 2014. Table 5.3 shows the  $PA$ ,  $EL$ , and scan number in every observation. Every scan, the integration time of ON and OFF position is 5 sec.

TABLE 5.1: Observation information of NML-Tau

Observation number	EL	PA	Scan number
1	$38^\circ$	$-53^\circ$	3
2	$52^\circ$	$-44^\circ$	8
3	$65^\circ$	$4^\circ$	2
4	$53^\circ$	$44^\circ$	6

### 5.3.2 Results and discussion

We denoted receiver polarizations as H and V (see section 5.2.1). We calculated Stokes parameters without calibration of  $\xi$  with two methods;  $H = E_x$ ,  $V = E_y$  and  $H = E_y$ ,  $V = E_x$ . Example of full Stokes spectra and a polarization angle spectrum with  $H = E_x$ ,  $V = E_y$  for one scan are shown in Fig. 5.3. We chose polarization angles at the peak frequency of Stokes  $I$  spectrum (see Fig. 5.3) and which are compared with  $EL + PA$  and  $EL - PA$  (see Fig. 5.4). The combination  $H = E_x$ ,  $V = E_y$  and  $EL - PA$  is closer to the inverse proportional relation (see Fig. 5.4) and the polarization angles are supposed to inverse proportional to  $\xi$ . Hence we adopt this setting to estimate Stokes parameters.

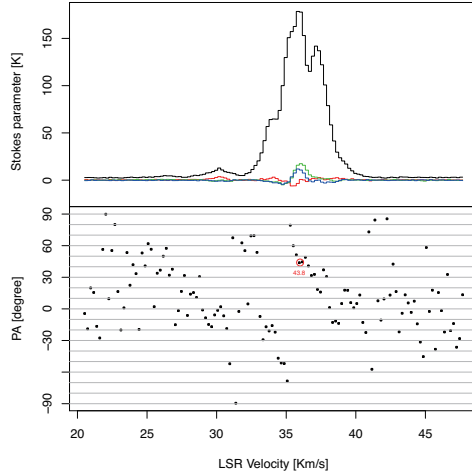


FIGURE 5.3: Full stokes spectra toward NML-Tau with  $H = E_x$ ,  $V = E_y$  without linearly polarized angle calibration.

(top):Full stokes spectra. The black, red, green and blue lines indicate Stokes  $I$ ,  $Q$ ,  $U$  and  $V$ , respectively. (Bottom):Black points indicate polarization angle Spectrum. The red open circule point the polarization angle at the frequency which is the peak of Stokes  $I$  spectrum and the red number right under the circle is the polarization angle value.

## 5.4 Phase calibration

### 5.4.1 Method

Calibration of instrumental phases in cross correlation,  $-\psi_{g,x} + \psi_{g,y}$  is crucial to estimation of Stokes  $V$ , because Stokes  $V$  is imaginary part of cross correlation. The instrumental phases are described with  $-\psi_{g,x} + \psi_{g,y} = \psi_a + 2\pi\nu\tau_{\Delta L} + \psi_{b,\nu}$  (see section 3.3.1). We estimated  $-\psi_{g,x} + \psi_{g,y}$  using artificial continuum linear polarization

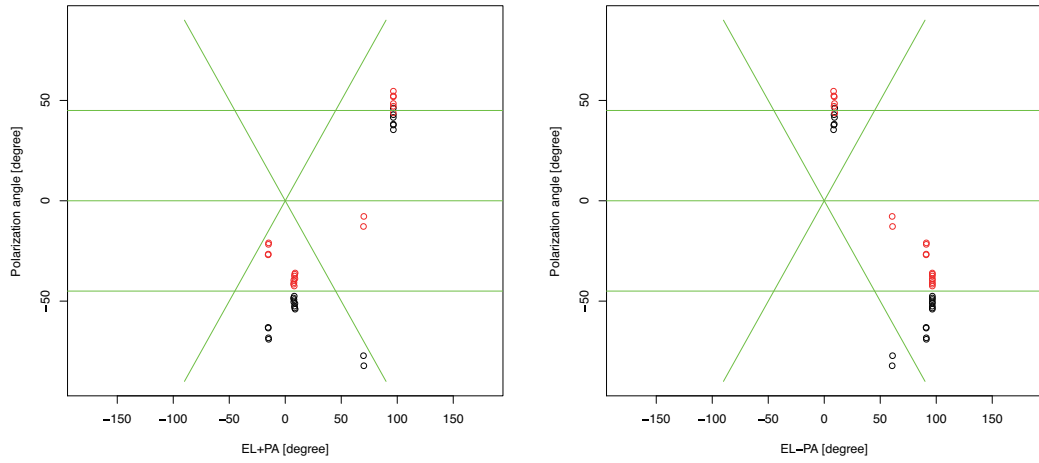


FIGURE 5.4: Polarization angle variation

The red and black open circles indicate polarization angles estimated with  $H = E_x$ ,  $V = E_y$  and  $H = E_y$ ,  $V = E_x$ , respectively. The green lines indicate line of  $y = \pm x$ . (Left):Relation of polarization angles and  $EL + PA$ . (Right):Relation of polarization angles and  $EL - PA$

spectra. As shown in equation 3.40, the relation of  $\langle \tilde{E}_x \tilde{E}_y^* \rangle$  and Stokes  $U$ ,  $V$  is described as

$$2 \langle \tilde{E}_x \tilde{E}_y^* \rangle = U + iV.$$

$U$  and  $V$  are real quantities. Hence in case of  $V = 0$ , phase of  $\langle \tilde{E}_x \tilde{E}_y^* \rangle$  is equal to 0. As shown in equation 3.7, cross correlation affected by D-term is given by

$$\langle \tilde{F}'_x \tilde{F}'_y^* \rangle \sim A_x A_y \exp(-i\psi_{g,x} + i\psi_{g,y}) (\langle \tilde{E}_x \tilde{E}_y^* \rangle + \tilde{D}_y^* \langle \tilde{E}_x \tilde{E}_x^* \rangle + \tilde{D}_x \langle \tilde{E}_y \tilde{E}_y^* \rangle).$$

Auto correlation terms with D-terms ( $\tilde{D}_y^* \langle \tilde{E}_x \tilde{E}_x^* \rangle + \tilde{D}_x \langle \tilde{E}_y \tilde{E}_y^* \rangle$ ) will change the phase because D-terms are complex numbers. Therefore the phase of  $\langle \tilde{F}'_x \tilde{F}'_y^* \rangle$  is different from  $-\psi_{g,x} + \psi_{g,y}$ . In case of  $|\langle \tilde{E}_x \tilde{E}_y^* \rangle| \gg |\tilde{D}_y^* \langle \tilde{E}_x \tilde{E}_x^* \rangle + \tilde{D}_x \langle \tilde{E}_y \tilde{E}_y^* \rangle|$ , D-term effect is negligible and phase of  $\langle \tilde{F}'_x \tilde{F}'_y^* \rangle$  is nearly equal to instrumental phases.  $\langle \tilde{E}_x \tilde{E}_x^* \rangle$  is large in the case of a strongly linearly polarized signal whose polarization angle is  $\pm 45^\circ$  with respect to  $x$  axis of the receiver. We introduce such a signal to the receiver using a wire grid (see Fig. 5.5). Radiation from sky and the absorber are passed through and reflected by the wire grid, respectively (see Fig. 5.5). Sky and the absorber are unpolarized. Hence there are no correlation between the absorber- and sky- radiation. Radiation from the absorber is stronger than that from sky. Therefore the polarization angle is same as the wire's alignment which is the vibration angle of the absorber component. Signal

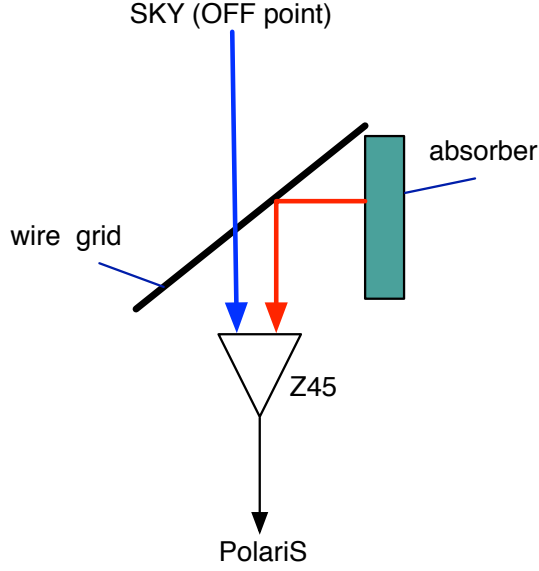


FIGURE 5.5: Configuration to introduce artificial linear continuum source to the receiver using wire grid.

The wire grid is placed with the direction of the wires is parallel to  $+45^\circ$  or  $-45^\circ$  with respect to the x axis of receiver. Radiation from sky and the absorber are passed through and reflected by the wire grid, respectively.

from sky is  $\sim 50$  K, the absorber temperature is 270 K and  $T_{RX} \sim 50$  K in each  $H$ ,  $V$  polarization system for Z45, so the polarization rate is  $\frac{270}{(50+50)+(270+50)} \sim 57\%$ ;  $H$  and  $V$  polarization correspond to polarization along x and y, respectively (see section 5.3).

The method is as follows. We assume  $\psi_{b,\nu}$  is constant over time and define a mean value of  $\psi_a$  as  $\langle \psi_a \rangle$ . The order of estimation is (1)  $\langle \psi_a \rangle + \psi_{b,\nu}$ , (2)  $\tau_{\Delta L}$  by time, and (3) time variation of  $\langle \psi_a \rangle$ ,  $\Delta \psi_a = \psi_a - \langle \psi_a \rangle$ .

1. We define a mean value of cross correlation of an artificial linearly polarized source and it is  $\tilde{S}_{\nu,mean} = \frac{1}{t_1-t_0} \int_{t_0}^{t_1} \left\langle \tilde{F}'_x \tilde{F}'_y^* \right\rangle dt$ , where  $t_0$  and  $t_1$  are start and end time of the observation. We estimate cross correlation function of  $\tilde{S}_{\nu,mean}$  like

$$C(\tau) = \int_0^{chnm} \tilde{S}_{\nu,mean} \exp(i2\pi\nu\tau) d\nu, \quad (5.1)$$

where  $chnm$  is channel number of the spectrometer and  $\tau$  is arrival time lag at the spectrometer between  $\tilde{F}'_x$  and  $\tilde{F}'_y$ . The peak value of the cross correlation function indicates the  $\tau_{\Delta L}$ .  $C(\tau)$  is discrete so we fit it with a quadratic function and estimate the peak value. And then we calibrate the  $\tau_{\Delta L}$  of  $\tilde{S}_{\nu,mean}$  and we define the spectrum as  $\tilde{S}_{\nu,mean,\tau cal}$ ;

$$\tilde{S}_{\nu,mean,\tau cal} = \frac{\tilde{S}_{\nu,mean}}{\exp(i2\pi\nu\tau_{\Delta L})}. \quad (5.2)$$

The phase of  $\tilde{S}_{\nu,mean,\tau cal}$  is equal to  $\langle \psi_a \rangle + \psi_{b,\nu}$ . Hence we calibrate the phase,  $\langle \psi_a \rangle + \psi_{b,\nu}$  using the cross correlation spectrum in fixed time as

$$\tilde{S}_{\nu,t,Bcal} = \frac{\langle \tilde{F}'_x \tilde{F}'_y^* \rangle}{\tilde{S}_{\nu,mean,\tau cal}}. \quad (5.3)$$

2. We estimate  $\tau_{\Delta L}$ s of  $\tilde{S}_{\nu,t,Bcal}$  using the same method of (1) and calibrate. We define the calibrated spectrum as  $\tilde{S}_{\nu,t,Bcal,\tau cal}$ .
3. Phase of  $\tilde{S}_{\nu,t,Bcal,\tau cal}$  indicates  $\Delta\psi_a$ .

#### 5.4.2 Verification result

We introduce a linearly polarized continuum signal to the receiver over  $\sim 1$  hour using the configuration in Fig. 5.5. The Lo signals (see section 5.2.1) is tuned frequencies for observation of CCS toward TMC-1 (see section 5.6). We estimated  $\tau_{\Delta L}$  and  $\Delta\psi_a$  every 1 second. We show the result in Fig. 5.6.

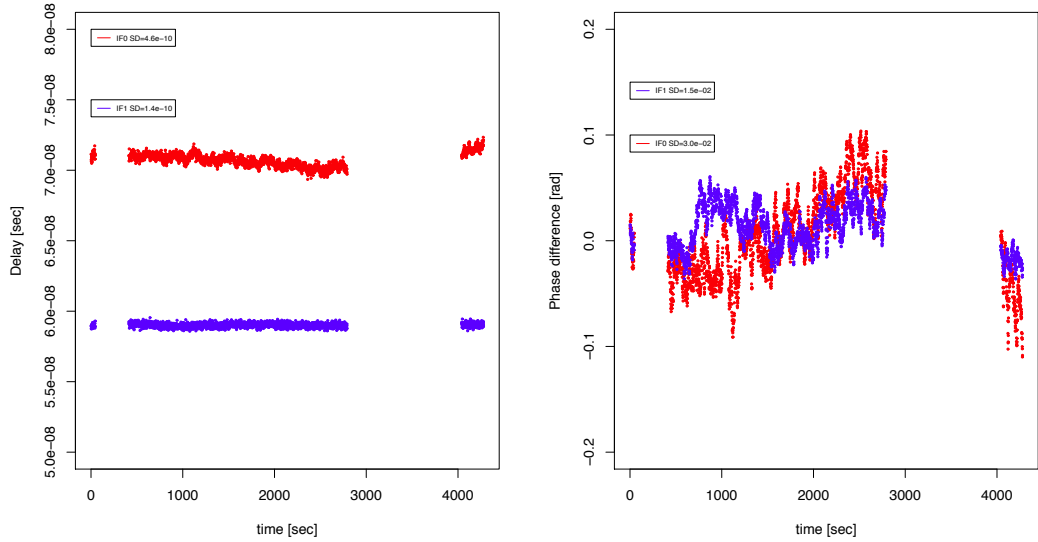


FIGURE 5.6: Delay and phase difference during for 1 hour  
(Left):Delay difference; time variation of  $\tau_{\Delta L}$ . (Right):Phase difference; time variation of  $\Delta\psi_a$ .

Standard deviations (SDs) of  $\Delta\psi_a$  describe SDs of  $\psi_a$ s, and the values for IF0 and IF1 are  $1.5 \times 10^{-2}$  rad and  $3.0 \times 10^{-2}$  rad, respectively. SDs of  $\tau_{\Delta L}$  for IF0 and IF1 are  $4.8 \times 10^{-10}$  sec and  $1.4 \times 10^{-10}$  sec, respectively.

We show the correlation between  $\Delta\psi_a$  and  $\tau_{\Delta L}$  in Fig. 5.7. P-value of  $\Delta\psi_a$  and  $\tau_{\Delta L}$  correlation is  $< 0.03$ .

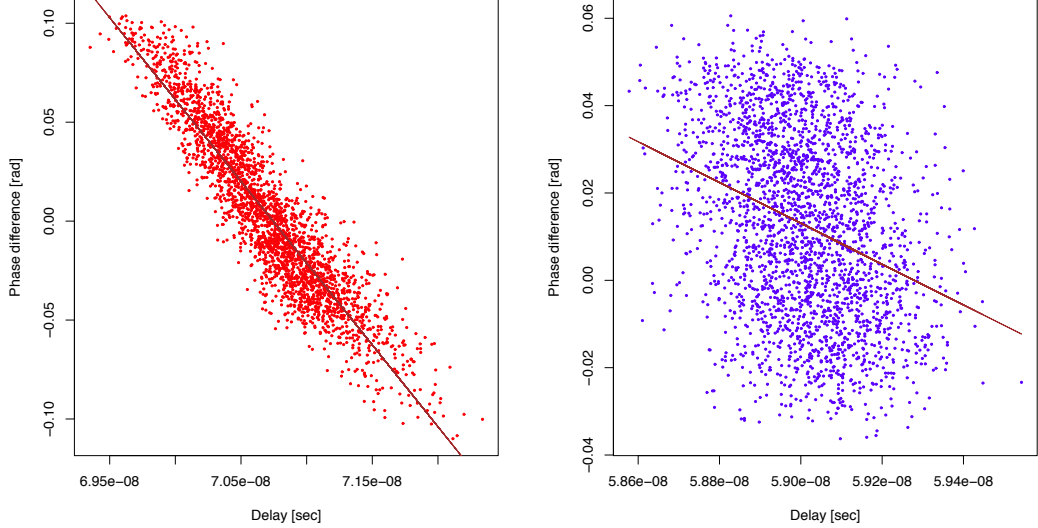


FIGURE 5.7: Correlation between phase and delay difference  
(Left):Red points describe relation between  $\Delta\psi_a$  and  $\tau_{\Delta L}$  of IF0. Brown line is linear regression for  $\Delta\psi_a$  and  $\tau_{\Delta L}$ . (Right):Relation between  $\Delta\psi_a$  and  $\tau_{\Delta L}$  of IF1. Brown line is linear regression for  $\Delta\psi_a$  and  $\tau_{\Delta L}$ .

### 5.4.3 Discussion about phase verification

We discuss about the variation of  $\Delta\psi_a$  and  $\tau_{\Delta L}$  over  $\sim 1$  hour.

1. Phase difference during integration times result in coherence. The relation between coherence loss and the SD,  $\phi_{rms}$  is

$$100 \times (1 - \exp(-\frac{\phi_{rms}^2}{2})). \quad (5.4)$$

$\phi_{rms} = 3 \times 10^{-2}$  rad for having the greatest SD, so that, coherence loss is  $< 0.05\%$  over 1 hour in cross correlations. The coherence loss decrease Stokes  $V$  up to 0.05% and it is enough negligible.

2. Phase difference causes misestimation of Stokes  $V$  and Stokes  $U$  components. Modulus of  $\langle \tilde{E}_x \tilde{E}_y \rangle$ ,  $| \langle \tilde{E}_x \tilde{E}_y \rangle |$  is equal to  $|V| + |U|$ . And  $\langle \tilde{E}_x \tilde{E}_y \rangle$  is decomposed into two components in  $U$  and  $V$  with phase of  $\langle \tilde{E}_x \tilde{E}_y \rangle$  like

$$U = \tilde{E}_x \tilde{E}_y \cos(-\phi_x + \phi_y - \psi_{g,x} + \psi_{g,y} + \Delta\psi_{g,y}), \quad (5.5)$$

$$V = \tilde{E}_x \tilde{E}_y \sin(-\phi_x + \phi_y - \psi_{g,x} + \psi_{g,y} + \Delta\psi_{g,y}). \quad (5.6)$$

Standard deviation phase,  $\phi_{rms}$  causes errors in sin and cos function up to  $2 \sin\left(\frac{\phi_{rms}}{2}\right)$  and  $\phi_{rms} = 3.0 \times 10^{-2} \ll 1$  so  $2 \sin\left(\frac{\phi_{rms}}{2}\right) \sim \phi_{rms}$ . Hence in case of using mean value of  $\langle \psi_a \rangle$  for 1 hour observation, the estimated  $U$  and  $V$  can be consider to be

$$U' = U \pm U\phi_{rms} \mp V\phi_{rms},, \quad (5.7)$$

$$V' = V \pm U\phi_{rms} \mp V\phi_{rms},, \quad (5.8)$$

$\phi_{rms} = 3.0 \times 10^{-2}$  rad, so Stokes  $V$  will decrease by 3% and increased by 3% of Stokes  $U$ . The decrease of 3% of Stokes  $V$  is enough small for Zeeman shift estimations. In CCS Zeeman observation, Stokes  $U$  has an order of magnitude weaker than Stokes  $V$  (see section 1.3). Hence the effect of Stokes  $U$  is negligible.

3. We estimate the effect of delay variation (the variance of  $\tau_{\Delta L}$ ). The greatest delay SD of IF0 is  $\sim 5.0 \times 10^{-10}$  sec. Between IF bandwidth from 0 MHz to 4 MHz,  $\sim 5.0 \times 10^{-10}$  sec causes a difference of  $\sim 5.0 \times 10^{-10} \times 2\pi \times 4 \times 10^6 \sim 0.001$  rad. It make a decrease in Stokes  $V$  up to 0.1%; the coherence loss  $< 0.008$  (see (1)) and the misestimation for Stokes  $U$  is  $< 0.1\%$  (see (2)) and it is enough negligible Stokes  $V$  measurement.
4.  $\Delta\psi_a$  and  $\tau_{\Delta L}$  show correlation since the P value  $< 0.05\%$ .  $\tau_{\Delta L}$  variation can cause  $\Delta\psi_a$  variation. We show the example in Fig. 5.8. Variance of  $\tau_{\Delta L}$  in RF (radio frequency which is not down-converted), that result in variation of  $\tau_{\Delta L}$  and  $\psi_a$  in IF (intermediate frequency). Hence we consider that variation of  $\Delta\psi_a$  is caused by  $\tau_{\Delta L}$  which depends on length difference between orthogonal polarization. Variation of  $\tau_{\Delta L}$  means the variation of signal propagation length. The reason can be considered to be the ambient temperature fluctuation.

## 5.5 D-term calibration

A D-term causes instrumental polarization (see section 3.3.2, 3.5). A D-term due to antenna optics is caused by the asymmetry of antenna optics e.g.[4]. The asymmetry of a dish varies with elevation (EL) angle e.g.[23]. Additionally, because of Nasmis optics, the beam of the NRO 45m with respect to receiver direction rotate due to EL change. So the D-term due to the dish rotate with respect to the D-term owing to processes after dish. Hence if the dish D-term is dominant, the D-term of the whole system may vary with EL. EL range in observation is typically  $30^\circ$ – $80^\circ$  at the NRO 45m. And optics of the NRO 45m is optimized at  $50^\circ$ . So we measured the D-term effect for Stokes  $V$  at around higher and lower EL and discuss the values and variation. We can

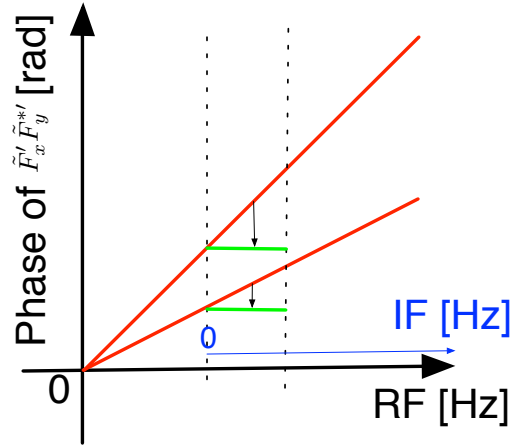


FIGURE 5.8: An example of a phase difference caused by a delay variation. Vertical axis indicates phase of  $\tilde{F}'_x \tilde{F}'_y^*$ . Horizontal axes of black and blue indicate RF and IF, respectively. The two red lines are phase spectra affected by different  $\tau_{\Delta L}$  in propagation path of RF. We calibrate the  $\tau_{\Delta L}$  in IF, then red lines are calibrated to green lines. The green lines have different  $\psi_a$ .

define the measurement method of the D-term effect for Stokes  $V$  using observation results of unpolarized source. At first, we describe the method below and then show the measurement results.

### 5.5.1 Theory of D-term effect measurement to Stokes $V$

D-term effect for Stokes  $V$  in equation 3.39 is

$$V'_{\text{src},x,y} = V + 2\text{Im}(\tilde{D}_x)T_{A,yy^*,\text{src}}^* - 2\text{Im}(\tilde{D}_y)T_{A,xx^*,\text{src}}^*,$$

In observation of Zeeman splitting in the CCS molecular line, linear polarization is negligible compared to the unpolarized component, so we can define  $T_{\text{src},A,x}^* \sim T_{\text{src},A,y}^*$ . Therefore in observation of CCS,

$$\begin{aligned} V'_{\text{CCS},x,y} &= V + \frac{2\text{Im}(\tilde{D}_x)T_{A,yy^*,\text{src}}^* - 2\text{Im}(\tilde{D}_y)T_{A,xx^*,\text{src}}^*}{2} I \\ &= V + \text{Im}(\tilde{D}_x)T_{A,yy^*,\text{src}}^* - \text{Im}(\tilde{D}_y)T_{A,xx^*,\text{src}}^* I. \end{aligned} \quad (5.9)$$

So if we estimate  $\text{Im}(\tilde{D}_x)T_{A,yy^*,\text{src}}^* - \text{Im}(\tilde{D}_y)T_{A,xx^*,\text{src}}^* = D_V$ , we can calibrate D-term effect.

In observation of an unpolarized source  $\frac{I}{2} = T_{src,A,x} = T_{src,A,y}$  and  $V = 0$ . So the the Stokes  $V$  of the unpolarized source is

$$V'_{unpol,x,y} = D_V I \quad (5.10)$$

And Stokes I affected by D-term is written as

$$I' = H_{xx} + H_{yy} = I + \tilde{D}_x^* \tilde{T}_{src,C}^* + \tilde{D}_x \tilde{T}_{src,C} + \tilde{D}_y^* \tilde{T}_{src,C}^* + \tilde{D}_y \tilde{T}_{src,C} \quad (5.11)$$

In unpolarized source,  $\tilde{T}_{src,C} = 0$ , then

$$\frac{V'_{unpol}}{I'_{unpol}} = D_V, \quad (5.12)$$

where  $I'_{unpol}$  is observed Stokes  $I$  toward the unpolarized source. So we estimate D-term effect observation of unpolarized source in equation 5.12.

### 5.5.2 Observation and Results

We observed the unpolarized source, Jupiter and we estimate  $D_V$ . To examine the EL dependence, we carried out observations at upper ( $37.5^\circ$ ) and lower ( $75.7^\circ$ ) EL. One scan time for ON point and OFF point is 10 s. Each EL, we acquired two scan and the observation time is 60 s. We show the summary of the observations in table 5.2.

TABLE 5.2: Observation of Jupiter

Feature	Remarks	
Date	April 17, 2014	
Center frequency	45.379 GHz	CCS line emission frequency at $J_N = 4_3 - 3_2$
Bandwidth	4 MHz	
Object	Jupiter	Unpolarized source
EL angle	$37.5^\circ, 75.7^\circ$	
Integration time of Jupiter	20 s	
Observation time	60 s	

Here we show the analysis of  $D_V$ . We assumed  $D_V$  is stable over 4 MHz bandwidth that is total bandwidth obtained in our polarimetry device. Firstly we obtained  $D_V$  spectrum each observation with equation 5.12. Secondly we estimated the frequency averages and the SDs, and the mean values and the SDs indicate  $D_V$  and error of  $D_V$ , respectively. We showed the results in table 5.3, 5.4.

TABLE 5.3: Calibration value of  $V$  for IF0

EL angle	$D_V$	error of $D_V$
37.5°	-0.018	0.056
75.7°	0.043	0.057

TABLE 5.4: Calibration value of  $V$  for IF1

EL angle	$D_V$	error of $D_V$
37.5°	-0.0021	0.056
75.7°	0.019	0.057

### 5.5.3 Discussion about D-term calibration

As shown in these tables,  $D_V$  varies with ELs but it is consistent within its uncertainty. The error is larger than the estimated  $D_V$  so to define the EL dependence of  $D_V$  we need more observation time; in order to reduce the error to 0.01 from 0.06, we need an integration time of 36 minutes. The upper limit was estimated to be  $\leq 0.1$ .

## 5.6 Test observation of CCS molecule

We observed our science target of a molecular core and predicted the observation time to achieve our goal: to detect a magnetic field of  $100 \mu\text{G}$  with an accuracy of  $5 \sigma$ . We applied phase and delay calibration and measured Zeeman shift,  $-68.0 \pm 35.4 \text{ Hz}$ .

### 5.6.1 Observations

We carried out polarization observation of our science target, CCS molecular line at 45.3 GHz of a molecular core of TMC-1 (Taurus Molecular Cloud-1) with 61 Hz frequency resolution. The observation coordinate is 04h41m42s.47,  $+25^\circ 41' 27''$ .1 (J2000) and the core labeled b7 clump of core D region in [38] (see Fig. 5.9). The spectral line in this region is narrow (see 5.9) and intense with  $T_A^* = 2.23 \pm 0.09 \text{ K}$  using the NRO 45m [49], so it is good for estimating Zeeman split.

We observed TMC-1 for 7 hours at 2014 Apr. 17. Between the TMC-1 observation we also observed calibrators (SiO maser, artificial linear continuum source); NML-tau of

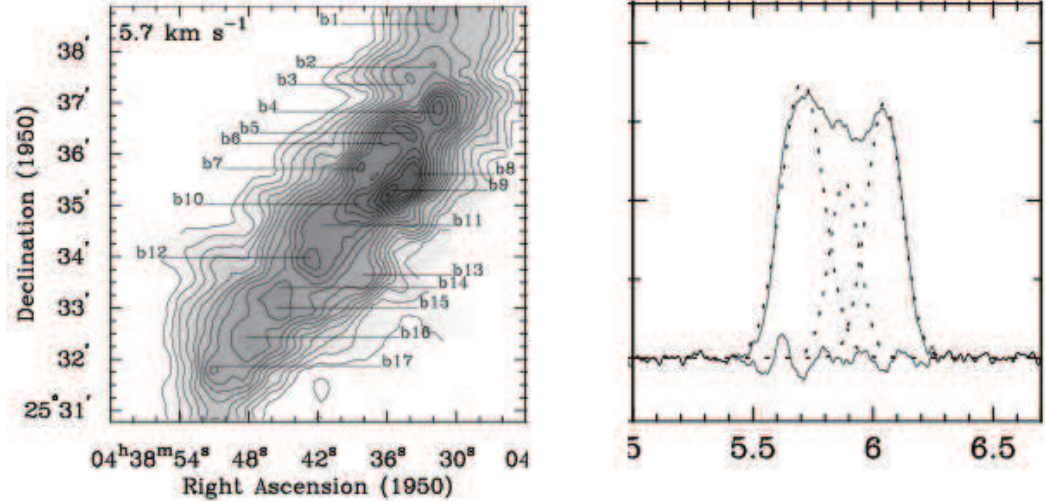


FIGURE 5.9: Map and the spectrum of CCS molecule at TMC-1  
(Left):Map of CCS molecular line of 5.6 km/s component. (Right):Spectrum line of CCS molecule at 45 GHz at center region of the left map.

SiO maser was observed for the pointing source and the artificial liner continuum source using wire grid was observed for delay and phase calibrator.

We confirmed Smoothing Bandpass Calibration (SBC) [57] with PolariS (see section 4.3.3.3). Therefore in TMC-1 observation, one scan time for OFF point is short compared to ON point (OFF:ON=10 s:120 s for 1 scan) so the total scan time for ON point is increased to reduce r.m.s efficiently.

### 5.6.2 Phase calibration

We estimate phase and delay using the same method as in section 5.4. We insert a wire grid by 1 hour for  $\sim 30$  s because variation of instrumental phase for 1 hour is negligible (see section 5.4). We show the results in Fig. 5.10. We smoothed the delays and phases (see Fig 5.10), and calibrate using the predicted values just at the observing time for calibration.

### 5.6.3 Result

We show the spectrum of Stokes  $I$  and  $V$  in figure 5.11. Tsys are 168–181 K and 142–157 K for each orthogonal linear polarizations. The rms noise level for both Stokes  $I$  and  $V$  reached 100 mK at 61 Hz resolution for 7 hours integration time and it is consist with predicted value based on the Tsys. And no significant linear polarization was detected.

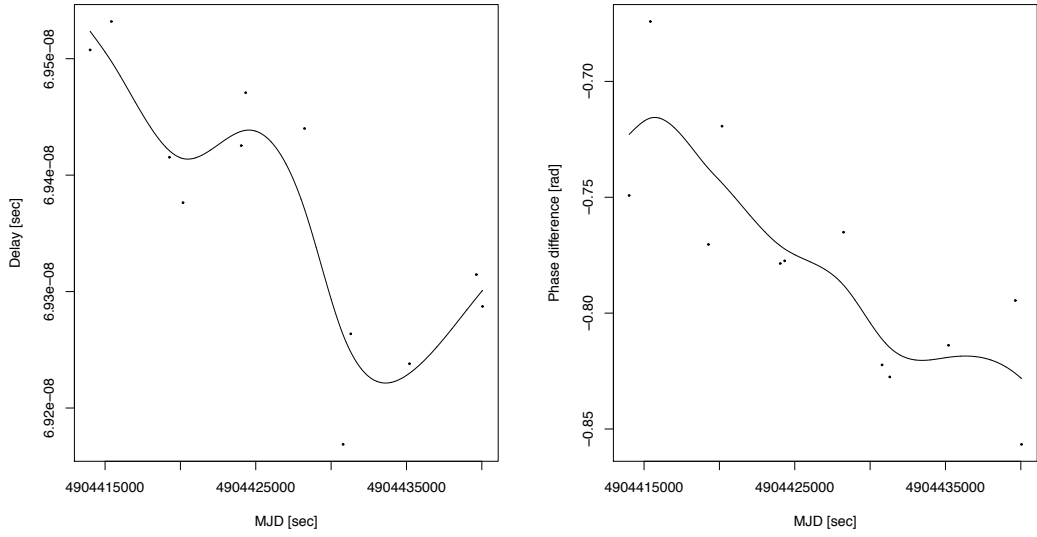


FIGURE 5.10: Delay and phase difference during TMC-1 observation  
Dots indicate measurements and lines indicate results of smoothed the measurements.  
(Left): Delay. (Right): Phase.

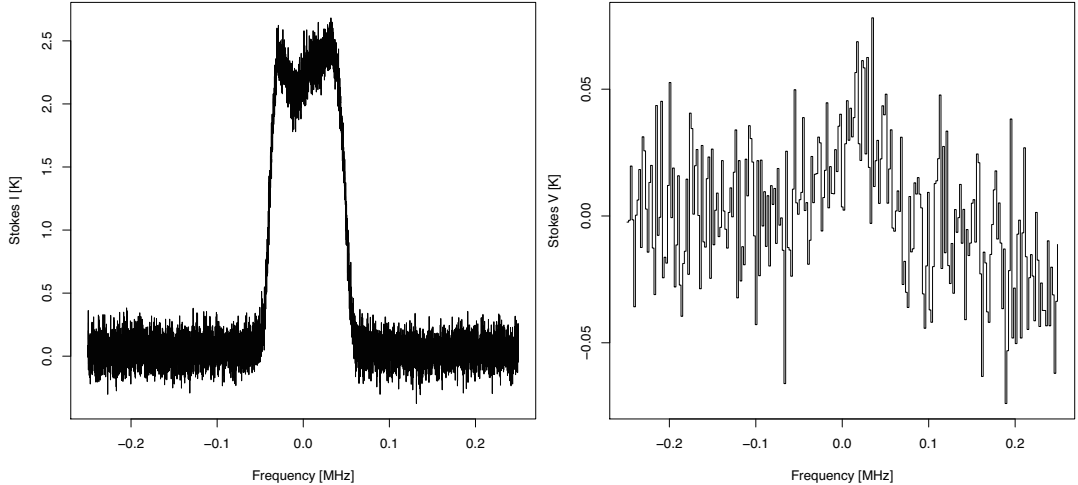


FIGURE 5.11: Stokes  $I$  and  $V$  of CCS molecular line toward TMC-1  
The center of the vertical axes indicate the center frequency of the line profile of Stokes  $I$ . (Left):Stokes  $I$  with 61 Hz spectrum resolution. (Right):Black line show Stokes  $V$  with spectrum resolution with 1 kHz.

#### 5.6.4 Evaluation of Stokes $V$

We estimate the Zeeman shift using the Stokes  $V$  and  $I$ . We fitted the spectrum with the equation defined in [42],

$$V(\nu) = \frac{dI}{d\nu} \Delta\nu + a, \quad (5.13)$$

where  $V$  is observed Stokes  $V$  spectrum,  $\frac{dI}{d\nu}$  is differential calculus of observed Stokes  $I$ ,  $\Delta\nu$  is Zeeman shift and  $a$  is an arbitrary constant which describe spill-over effect. The estimation method of  $\Delta\nu$  is as follow.

- We apply spline smoothing to observed Stokes  $I$  with 61Hz resolution to reduce noise (see Fig. 5.12).
- We estimate frequency derivative of smoothed Stokes  $I$  (see Fig. 5.12).
- We fitted the  $\Delta\nu$  and  $a$  using observed Stokes  $V$  with 61Hz resolution and the derivation of smoothed Stokes  $I$  with equation 5.13.

We show the fitting result,  $\frac{dI}{d\nu}\Delta\nu + a$ , over observed Stokes  $V$  with 1 kHz resolution in Fig 5.13. The Zeeman shift,  $\Delta\nu$  was  $-68.0 \pm 35.4$  Hz.

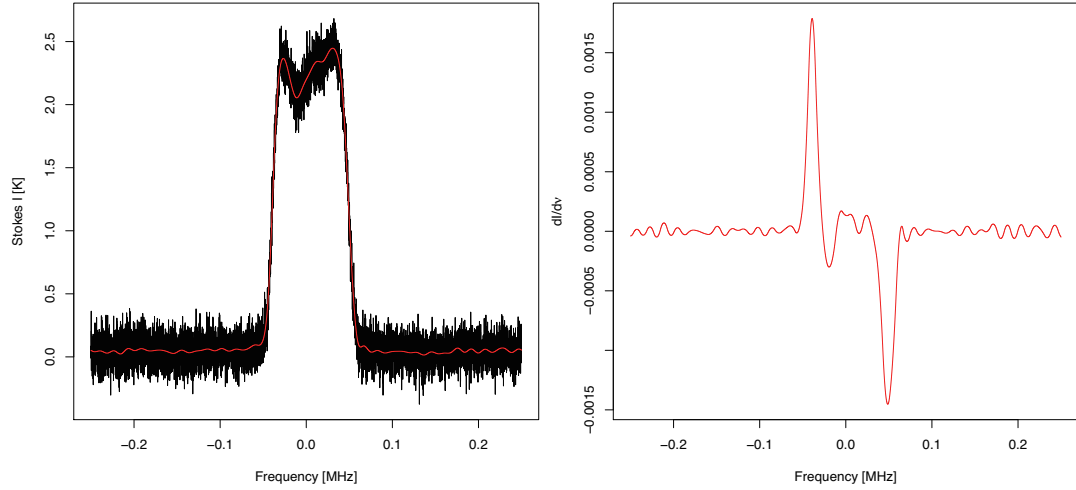


FIGURE 5.12: Smoothed Stokes  $I$  and frequency derivative of the smoothed  $I$ . The center of the vertical axes indicate the center frequency of the line profile of Stokes  $I$ . (Left):Black line indicate Stokes  $I$  with 61 Hz spectrum resolution. Red line show the smoothed the Stokes  $I$  spectrum. (Right):Red line indicates frequency derivative of the smoothed Stokes  $I$ .

### 5.6.5 Discussion about Zeeman test observation

The rms noise level of Stokes  $I$  and  $V$  is consistent with the predicted value from Tsys. So the measurement is thought to be going well. We did not applied D-term calibration. As shown in equation 5.9, due to D-term, an additional component in terms of Stokes  $I$  is added to Stokes  $V$ . Stokes  $V$  spectrum shape due to Zeeman effect is significantly different with Stokes  $I$ . So we thought the D-term effect is small for Zeeman fitting. The standard error of Zeeman shift reached 35.4Hz for 7 hours. To estimate  $100\mu$  G

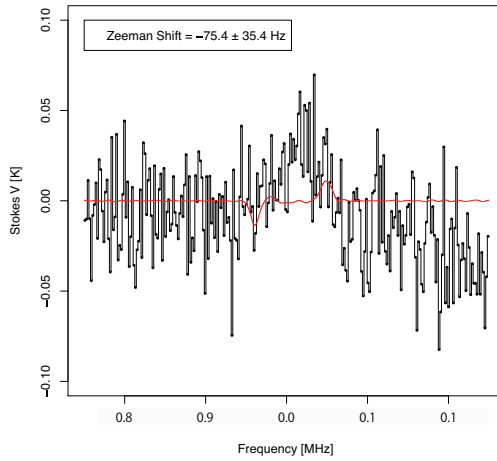


FIGURE 5.13: Observed Stokes  $V$  toward TMC-1 and the fitting result.

The center of the vertical axis indicate the center frequency of the line profile of Stokes  $I$ . Black line indicate observed Stokes  $V$  with 1 kHz spectrum resolution. Red line indicate predicted Stokes  $V$  spectrum by fitting with equation 5.13.

with  $5\sigma$  level, we need to reduce the rms noise level to 12.8 Hz ( $64\text{ Hz}/5$ ). We predicted observation time to achieve the required rms level, 12.8 Hz using the obtained rms, 35.4 Hz as  $(\frac{35.4}{12.8})^2 \times 7\text{ hours} = 54\text{ hours}$

## 5.7 Summary

We have established polarimetry device and calibration method for a measurement of Zeeman shift in CCS molecular lines. To measure the Zeeman shift, we need accurate measurement of Stokes  $V$ . We matched observation data to components of Stokes parameter formula using SiO maser observations and we confirmed that the calibration angle,  $\xi$  is equal to  $EL - PA + RA$  and relations of the receiver polarizations ( $H, V$ ) and the polarizations in Stokes parameter formula ( $E_x, E_y$ ) are  $H = E_x$  and  $V = E_y$ . Stokes  $V$  has instrumental polarization due to (1) instrumental phases in cross correlation and (2) D-term effect. We clarified the theory and method of these calibrations, and estimated these values. We measured components of the instrumental phases ( $\tau_{\Delta L}, \psi_a$ ) using an artificial linearly polarized continuum source and discussed the variations. The variations are thought due to ambient temperature fluctuation. The variations will decrease Stokes  $V$  up to 4%; the coherence loss  $< 0.06$  and the misestimation for Stokes  $U < 3\%$ , and it is enough negligible in the measurement of the Zeeman shift. We estimated  $D_V$ , which represents D-term effect to Stokes  $V$ , using Jupiter observations which described  $D_V \sim -0.01\text{--}0.04 \pm 0.05$ . The random error is larger than estimated  $D_V$  so we

need more longer observation time to derive  $D_V$ . We carried out test observations of a pre star-forming core toward TMC-1 for 7 hours, and we estimated a observation time of 54 hours to achieve our goal; to measure Zeeman shift of 64 Hz with an accuracy of  $5\sigma$ . However to discuss this result more clearly, we need to calibrate D-term. Hence we will observe Jupiter with more longer integration time and discuss the Zeeman shift more clearly.

# Chapter 6

## Conclusions and remarks

This thesis mainly addresses the development of the software polarization spectrometer, PolariS and the optimization of the polarization calibration procedure to detect the Zeeman splitting of CCS molecular lines for the purpose of magnetic field measurement in pre star-forming cores.

As shown in chapter 1, The magnetic field of a pre star-forming core has not been estimated yet although it is important to examine the role of magnetic fields in star-formation. Using the measurement of Zeeman splitting toward CCS molecular lines, we can estimate the magnetic field of pre star-forming cores. To examine its role we need to confirm whether a magnetic field strength of  $100 \mu\text{G}$  exists in the core. With  $100 \mu\text{G}$ , we expect a Zeeman shift of only  $\sim 64 \text{ Hz}$  in Stokes  $V$  and the expected Stokes  $V$  is weak (only a few mK). Hence we developed the high resolution spectrometer ( $< 64\text{Hz}$ ), PolariS and polarimetry device for accurate Stokes  $V$  measurement to measure the small Zeeman shift. Our science goal is to detect the 64 Hz Zeeman splitting toward the CCS molecular line with an accuracy of  $5 \sigma$ .

### 6.0.1 What Was Revealed?

#### [1] Accurate Stokes $V$ measurement method

There are two methods of Stokes  $V$  measurement. One is dual linear polarization reception and the other is dual circular polarization reception. In Chapter 3 we showed the systematic error with equations which indicated dual linear polarization reception is better than dual circular polarization reception. In early studies, Zeeman shift in CCS molecules were observed with circular polarization reception. But we established that a polarimetry device with linear polarization reception can detect Stokes  $V$  more effectively.

## [2] Development and test of PolariS

To detect a Zeeman shift of 64 Hz with linear polarization reception, we need a polarization spectrometer with high resolution (< 64Hz). We built a polarization spectrometer, PolariS with 61 Hz frequency resolution (see chapter 4). In modern radio telescopes, polarization spectrometers composed of specific hardware designed for fixed specifications. Software based spectrometers yield some advantages; eg, a reasonable cost and flexible specification. Hence we developed a software based polarization spectrometer, PolariS. PolariS consists of a VLBI digitizer, K5/VSSP32 for data acquisition, and a PC equipped with GPU. Thanks to a high degree of precision in quantization of the analog-to-digital converter and arithmetic in the GPU, PolariS offers excellent performance in linearity, dynamic range, sensitivity, bandpass flatness and stability. The software has been released under the MIT License and is available to the public.

## [3] Calibration method for Stokes $V$ measurement

We installed a polarimetry device equipped with PolariS and a dual linear receiver Z45 at the Nobeyama 45m radio telescope (NRO45m) (see chapter 5). At first, we verified the relation of obtained polarizations and polarizations defined in Stokes parameter equation A.1 using SiO maser observations. Additionally we needed two calibrations to estimate Stokes  $V$ ; (1) instrumental phase in cross correlation (2) the D-term effects to Stokes  $V$ . In earlier study, the theory and method of these calibrations were not written clearly. So we clarify it and optimize these calibrations. We estimated the instrumental phase over 1 hour. The variation of instrumental phase is sufficiently stable over 1 hour for Stokes  $V$  measurement due to the Zeeman effect and it is enough to meet a requirement of phase stability. We estimate  $D_V$ ; term of Stokes  $I$  and  $D_V I$  is added to Stokes  $V$ .  $D_V$  is smaller than the error,  $\sim 0.06$  and we estimate an upper limit of  $D_V > 0.1$ .

## [4] Measurement of Zeeman split in CCS molecule without D-term calibration

We observed the CCS molecule toward a molecular core in TMC-1 using our polarimetry device with 61 Hz frequency resolution for 7 hours (see chapter 5). The rms of Stokes  $I$  and Stokes  $V$  spectrum reached 100 mK and the value is consistent with Tsys and the integration time. We estimate the Zeeman shift using these spectra without D-term calibration and then we estimated that an observation time, 54 hours is required to achieve our science goal using our system.

### 6.0.2 What Are Uncompleted?

#### [1] Measurement of $D_V$

We couldn't derive  $D_V$  because of the large ramdom error. We need to estimate  $D_V$  to measure the Zeeman shift more clearly. The error of  $D_V$  reached 0.06 for a 60 s observation. Hence the error will reduce to 0.01 with a reasonable observation time of 36 minutes. Therefore we will estimate it with more longer integration time.

## 6.1 Future Prospects

### 6.1.1 Measurement of magnetic field strength of molecular cores using our polarimetry device

We established a polarimetry divice optimized for a measurement of Zeeman splitting in CCS molecules in order to measure the magnetic field strength of molecular cores. We estimated a required observing time of 57 h to estimate  $100 \mu G$  magnetic field with accuracy of  $5\sigma$  level. Therefore we may successfully determine whether a magnetic field of  $100 \mu G$  exist in molecular cores for the first time in the world. If we can mesure and examine it, we can confine star-forming models.

### 6.1.2 Use of PolariS and our polarimetry in another radio telescopes

PolariS program is free to distribute, and the components to build PolariS can be bought at a reasonable price (JPY  $\sim 570,000$ ). Hence it's easy to make a copy of PolariS. Therefore PolariS can enable high resolution spectroscopy and polarimetry in other radio telescopes. Anyone can edit the PolariS code because of the MIT licence. So anyone is free to change the specifications.

Our calibration methods for Stokes  $V$  measurement can be used in radio telescopes equipped with dual linear polarization receivers and a polarization spectrometer. Hence it will improve the Stokes  $V$  measurement in such a telescope.

# Appendix A

## Feed alignment

### A.1 Relation of Stokes parameter and the angle between feed direction and north pole

As shown in Fig. 2.1, linear polarization angle is defined with respect to the north celestial pole. Stokes parameter measurement in equation 2.28, direction of x and north pole is assumed in same direction. Hence to measure the linear polarization angle, we need to rotate receiver polarization direction of x to North pole. Here the direction of the north pole and the west denote  $X_0$  and  $Y_0$ ; that are the axis for general polarization description (see Fig. A.1), and the direction of receiver polarization of x- and y- denote  $X$  and  $Y$  (see Fig. A.1). We additionally define the angle between  $X_0$  and  $X$  is  $\xi$  (see Fig. A.1).  $\xi$  is equal to  $EL - PA + RA$  in case of NRO 45m (see section 5.3). We show the equation for Stokes parameters using the electric vector along to X- and Y-direction,  $\tilde{E}_Y$  and  $\tilde{E}_Y^*$ , as

$$\begin{pmatrix} I \\ Q \\ U \\ V \end{pmatrix} = \begin{pmatrix} 1 & 0 & 0 & 1 \\ \cos 2\xi & -\sin 2\xi & -\sin 2\xi & -\cos 2\xi \\ \sin 2\xi & \cos 2\xi & \cos 2\xi & -\sin 2\xi \\ 0 & -i & i & 0 \end{pmatrix} \begin{pmatrix} \langle E_x^2 \rangle \\ \langle \tilde{E}_X \tilde{E}_Y^* \rangle \\ \langle \tilde{E}_Y \tilde{E}_X^* \rangle \\ \langle E_y^2 \rangle \end{pmatrix}. \quad (\text{A.1})$$

The central  $4 \times 2$  submatrix is a rotation matrix.

### A.2 Estimation of feed direction

We estimate the receiver angle,  $RA$  which is the angle between receiver polarization coordinate and horizontal coordinates. The calibration angle for linear polarization

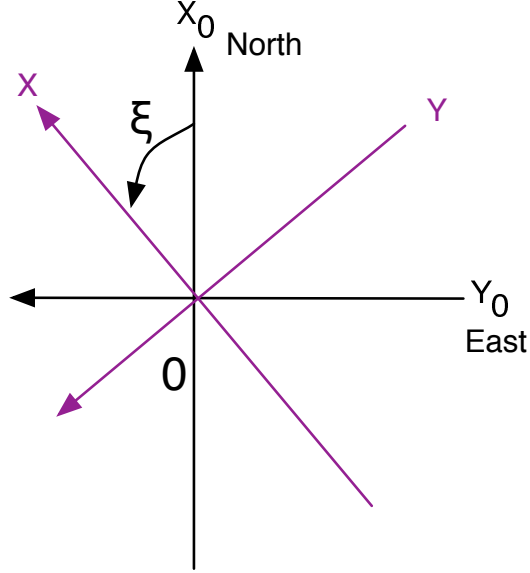


FIGURE A.1: Relation between the basis for general Stokes parameter and for detected electric field.

$X_0$  and  $Y_0$  are bases for general description of Stokes parameter.  $X$  and  $Y$  are bases for detected electric fields.

direction,  $\xi$  is define as  $EL - PA + RA$  (see section 5.3). Calibration of  $RA$  is need to estimate linear polarization angle. We can estimate  $RA$  using a linear polarized source known polarization angle. Because if we estimate the polarization angle about such a source with no calibration of  $RA$ , the angle will be summation of  $RA$  to the known polarization angle. Crab Nebula is know as linear polarized continuum source and the polarization angle is stable and the angle is  $152.13^\circ \pm 0.34^\circ$  [1]. Hence we observed Crab Nebula to estimate  $RA$ .

### A.2.1 observation

We observed the source 3 times at April 17, 2014. The integration time of ON and OFF scan are 10s. We show the information EL, PA, scan number in table A.1.

TABLE A.1: Observation information of NML tau

Observation number	EL angle	PA angle	Scan number
1	$38^\circ$	$-61^\circ$	3
2	$73^\circ$	$-33^\circ$	3
3	$63^\circ$	$62^\circ$	3

### A.2.2 Results and discussion

We show the received total power variation (which is not applied any calibration) of 3 scan for x- and y- polarizations in Figure A.2. As you can see the power at OFF point vary between 2 polarizations. The variation will come from gain instability because of sky is unpolarized source. Linear polarization estimate by  $\sqrt{Q^2 + U^2} =$

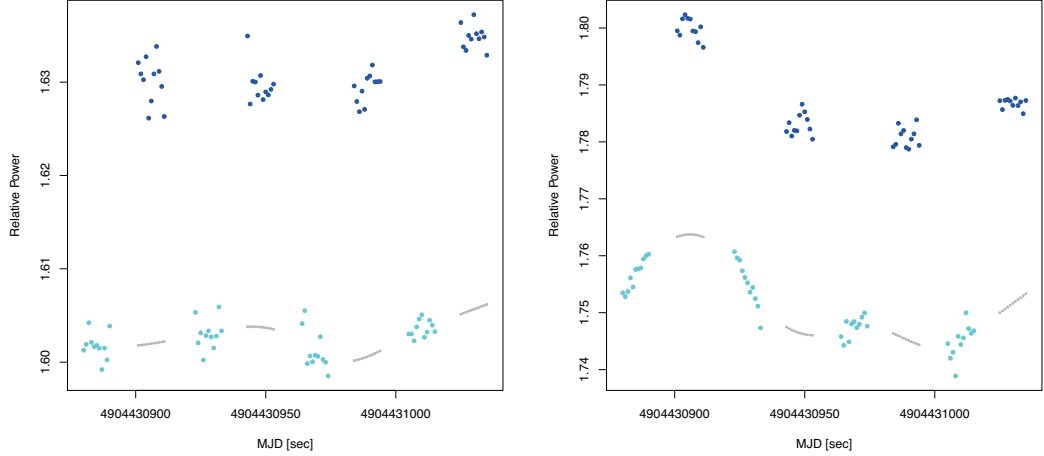


FIGURE A.2: Received total power variations during Crab Nebula observation  
Blue and light blue points indicate ON and OFF points. Gray lines indicate smoothed power of OFF points. (left):Received total power for x- polarization. (Right):Received total power for y- polarization.

$\sqrt{\left(\langle \tilde{E}_x \tilde{E}_x^* \rangle - \langle \tilde{E}_y \tilde{E}_y^* \rangle\right)^2 + \left(\text{Re} \left( \langle \tilde{E}_x \tilde{E}_y^* \rangle \right)\right)^2}$ . Hence gain variation between 2 polarizations cause error to the component of  $\langle \tilde{E}_x \tilde{E}_x^* \rangle - \langle \tilde{E}_y \tilde{E}_y^* \rangle$ . During the 1 scan of OFF point 1% gain variation between x- and y- polarization was found. 1% gain variation will cause  $\sim 1.7$  K instrumental polarization because of Tsys 170K during the observation. Linear polarization of Crab Nebula is  $\sim 0.7$  K with NRO45 beam so the effect is too large. To reduce the the effect we smoothed OFF point power and we predict the Off power at the ON point.(see Fig A.2). And we estimate Stokes parameter using predicted OFF without RA calibration. We show the Full Stokes parameter and polarization angle for each scan in Fig A.3. The SDs of Stokes Q and U are 0.1 K and 0.1 K, respectively. The values is enough smaller then 1.7 K. So the smoothing procedure seems to go well and we can discuss the RA. And we estimate the RA using mean value of the polarization angle, and that is  $92^\circ \pm 4^\circ$ .

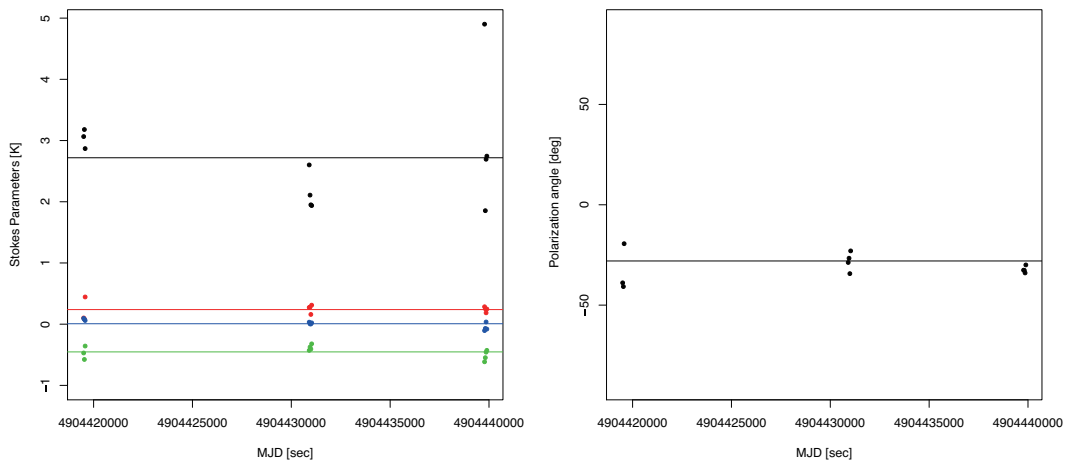


FIGURE A.3: Full Stokes parameter and polarization angle of Crab nebula without *RA* calibration.

Points and line indicate estimation values and the mean value, respectively. (Left): Colors of black, red, green and blue indicate Stokes  $I$ ,  $Q$ ,  $U$  and  $V$ , respectively. (Right): Polarization angles.

# Bibliography

- [1] Aumont, J., Conversi, L., Thum, C., et al. 2010, *AAp* **514**, AA70
- [2] Baart, E. E., Cohen, R. J., Davies, R. D., Rowland, P. R., & Norris, R. P. 1986, *MNRAS* **219**, 145.
- [3] Barsdell, B. R., Bailes, M., Barnes, D. G., & Fluke, C. J. 2012, *MNRAS* **422**, 379
- [4] Cenacchi, E., Kraus, A., Orfei, A., & Mack, K.-H. 2009, *A&A*, **498**, 591
- [5] Chandrasekhar, S., & Fermi, E. 1953, *ApJ* **118**, 113
- [6] Crutcher, R. M., Troland, T. H., Goodman, A. A., et al. 1993, *ApJ* **407**, 175.
- [7] Crutcher, R. M., Troland, T. H., Lazareff, B., Paubert, G., &azès, I. 1999, *ApJL* **514**, L121.
- [8] Crutcher, R. M. 1999, *ApJ* **520**, 706
- [9] Crutcher, R. M. 2004, The Magnetized Interstellar Medium, 123
- [10] Crutcher, R. M. 2012, *ARAA* 50, 29
- [11] Dowd, A., Sisk, W., & Hagen, J. 2000, *IAU Colloq. 177: Pulsar Astronomy - 2000 and Beyond* **202**, 275.
- [12] Elmegreen, B. G. 2000, *ApJ* **530**, 277
- [13] Falgarone, E., Troland, T. H., Crutcher, R. M., & Paubert, G. 2008, *AAp* **487**, 247
- [14] Ferrière, K. M. 2001, *Reviews of Modern Physics* **73**, 1031
- [15] Yasuo Fukui et al. 2008, Printed in Japan ISBN978-4-535-60726-2, p.169–170
- [16] Gaume, R. A., & Mutel, R. L. 1987, *ApJS* **65**, 193.
- [17] Goodman, A. A., Crutcher, R. M., Heiles, C., Myers, P. C., & Troland, T. H. 1989, *ApJL* **338**, L61.
- [18] Heiles, C., & Troland, T. H. 2004, *ApJS* **151**, 271

- [19] Horiuchi, S., &ameya, O. 2000, *PASJ* **52**, 545.
- [20] Iono, D., Hatsukade, B., Kohno, K., et al. 2012, *PASJ* **64**, L2
- [21] Kondo, T., Koyama, Y., Takeuchi, H., &imura, M. 2006, *IVS 2006 General Meeting Proceedings*, 195.
- [22] Kondo, T., Koyama, Y., Takeuchi, H., & Ichikawa, R. 2006, *IVS NICT-TDC News* **27**, 5.
- [23] Levin, S. M., Langer, W. D., Velusamy, T., Kuiper, T. B. H., & Crutcher, R. M. 2001, *ApJ* **555**, 850.
- [24] Lo, K. Y., Walker, R. C., Burke, B. F., et al. 1975, *ApJ* **202**, 650.
- [25] Mac Low, M.-M., Smith, M. D., Klessen, R. S., & Burkert, A. 1998, *ApSS* **261**, 195
- [26] Mac Low, M.-M., &lessen, R. S. 2004, *Reviews of Modern Physics* **76**, 125.
- [27] Magro, A., Karastergiou, A., Salvini, S., et al. 2011, *MNRAS* **417**, 2642
- [28] Morita, K.-I., Nakai, M., Takahashi, T., et al. 2003, *Astronomical Data Analysis Software and Systems XII* **295**, 166
- [29] Electricity and Magnetism, Munir H. Nayfeh and Morton K. Brussel, John Wiley & Sons, 1986, ISBN 0-471-82985-4
- [30] Naomasa Nakai et al. 2009, Printed in Japan ISBN978-4-535-60736-1
- [31] Nakajima, T., Sakai, T., Asayama, S., et al. 2008, *PASJ* **60**, 435
- [32] Nakamura, F., & Li, Z.-Y. 2005, *ApJ* **631**, 411
- [33] Nakamura, F., Ogawa, H., Kameno, S., et al. 2013, *Astronomical Society of the Pacific Conference Series* **476**, 239.
- [34] Nakano, T., & Nakamura, T. 1978, *PASJ* **30**, 671
- [35] Nakatake, A., Kameno, S., & Takeda, K. 2010, *PASJ* **62**, 1361.
- [36] Norris, R. P. 1984, *MNRAS* **207**, 127.
- [37] Onishi, T., Mizuno, A., Kawamura, A., Tachihara, K., & Fukui, Y. 2002, *ApJ* **575**, 950.
- [38] Peng, R., Langer, W. D., Velusamy, T., Kuiper, T. B. H., & Levin, S. 1998, *ApJ* **497**, 842.
- [39] Reid, M. J., Haschick, A. D., Burke, B. F., et al. 1980, *ApJ* **239**, 89.

- [40] Rohlfs, K., & Wilson, T. L. 1996, Tools of Radio Astronomy, Printed in Germany, ISBN 3-540-60981-4
- [41] Sandstrom, K. M., & Goodman, A. 2001, **Bulletin of the American Astronomical Society** **33**, #149.04
- [42] Sault, R. J., Killeen, N. E. B., Zmuidzinas, J., & Loushin, R. 1990, *ApJS* **74**, 437
- [43] Jon, Schiller., 2009, Printed in the United States of America ISBN1-4392-4156-2
- [44] Shinnaga, H., Tsuboi, M., & Kasuga, T. 1999, Star Formation 1999, 175
- [45] Shinnaga, H., & Yamamoto, S. 2000, *ApJ* **544**, 330.
- [46] Shu, F. H., Adams, F. C., & Lizano, S. 1987, *ARA&A* **25**, 23.
- [47] Spitzer, L. [1968], *New York: Interscience Publication.*
- [48] Sugitani, K., Nakamura, F., Watanabe, M., et al. 2011, *ApJ* **734**, 63.
- [49] Suzuki, H., Yamamoto, S., Ohishi, M., et al. 1992, *ApJ* **392**, 551.
- [50] Thompson, A. R., Moran, J. M., & Swenson, G. W., Jr. 2001, "Interferometry and synthesis in io astronomy by A. Richard Thompson, James M. Moran, and George W. Swenson, Jr. 2nd ed. New York : Wiley, c2001.xxiii, 692 p. : ill. ; 25 cm. "A Wiley-Interscience publication." Includes bibliographical references and indexes. ISBN : 0471254924".
- [51] Tilley, D. A., & Pudritz, R. E. 2007, *MNRAS* **382**, 73
- [52] Tinbergen, J. 1996, Astronomical Polarimetry, by Jaap Tinbergen, pp. 174. ISBN 0521475317. Cambridge, UK: Cambridge University Press, September 1996.
- [53] Troland, T. H., & Crutcher, R. M. 2008, *ApJ* **680**, 457.
- [54] Thum, C., Wiesemeyer, H., Paubert, G., Navarro, S., & Morris, D. 2008, *PASP* **120**, 777.
- [55] Tokuda, K., Kozu, M., Kimura, K., et al. 2013, *Astronomical Society of the Pacific Conference Series* **476**, 403.
- [56] Troland, T. H., & Heiles, C. 1986, *ApJ* **301**, 339.
- [57] Yamaki, H., Kameno, S., Beppu, H., Mizuno, I., & Imai, H. 2012, *PASJ* **64**, 118.
- [58] Zweibel, E. G. 1988, *ApJ*, 329, 384



# Acknowledgment (謝辞)

本研究において、亀野誠二教授には大変お世話になり、また多大なご迷惑をおかけ致したこと、この場を借りてお詫び申し上げます。学部四年生の卒業論文から博士過程までの間、内容の大変充実した生活を過ごさせていただきまして、誠にありがとうございました。

国立天文台 野辺山宇宙電波観測所長の久野成夫教授と斎藤正雄准教授には野辺山観測所での受け入れ・指導教官として、私の野辺山電波観測所での研究を支えていただきました。日々、貴重な意見を頂きありがとうございました。電波天文の観測所である現場を通じて、得たことは非常に大きく公私ともに充実した日々を過ごせました。

鹿児島大学の研究スタッフの皆様、学生の皆様には公私ともに大変お世話になりました。とりわけ今井裕准教授には研究に関する多くの助言を頂きました。

博士2年から3年にかけて中西裕之准教授には鹿児島大学での指導教員として遠方での研究で不自由な面を親切に対応してくださいました。

鹿児島大学の事務局の皆様には遠方での手続きに関する配慮をいただきました。

Z45のプロジェクトメンバーには偏波観測のサポートや基本的な受信機の性能の計測方法、観測方法を教えていただくとともに、私的な部分でも親切に接していただき心の支えとなりました。プロジェクトリーダーの中村文隆准教授には星形成における磁場の役割について丁寧に教えていただきました。東京学芸大学の土橋一仁教授、下井倉ともみ様、落合哲様、米谷夏樹様には偏波観測の面で非常にお世話になりました。

名古屋大学の中島拓助教、茨城大学の米倉覚則准教授にはZ45の受信機の立ち上げの際に多くの指導をいただき大変勉強になりました。

大阪府立大学の小川英夫教授と研究室の学生の皆様にはいつも暖かく接していただきました。木村公洋様、岡田望様、高津湊様、徳田一起様、長谷川豊様にはZ45受信機関係で大変お世話になりました。また、ここで紹介していない他の大阪府立大のスタッフや、学生の方が、偏波観測の要求を達成するために尽力していただききました。

名古屋大学の金工室の河合さんには偏波較正に用いる wire grid の製作手法等について教えていただき、wire gridの扱いに関する注意点等を学ぶことができました。

国立天文台 野辺山宇宙電波観測所では、2年間に渡りお世話になりました。技術職員の神澤富雄様、岩下浩幸様、宮澤和彦様、御子柴廣様、斎藤泰文様、半田和幸様、宮沢千栄子様、和田拓也様には45mの観測システムや、私の研究を進める上でいつも相談に応じてくれて有益な情報交換が出来、大変お世話になりました。専門研究職員の大矢正明様、高橋茂様、畠谷仁男様、前川淳様には、計算機関連の専門的な意見を頂きましてありがとうございました。梅本

智文助教には、VLBIバックエンドの接続に関する疑問を親切に教えていただきました。ありがとうございました。大島泰助教、高野秀路助教、南谷哲宏特任助教、研究員の諸隈佳菜様、竹腰達哉様、西村淳様、岩井一正様、研究支援員の佐藤立博様、西谷洋之様、荒井均様からは、多くの貴重なアドバイスを頂きました。また、広報担当の衣笠健三様、内藤明彦様、西岡真木子様からは、宇宙ガールでの講演させていただき、忘れられない貴重な機会を得ました。また、事務員や食堂の皆様に心身ともに支えていただきこの2年間を乗り切ることができました。ありがとうございました。

東邦大学の谷口琴美様には、光伝送系システムの線形性の確認のときなど、一人では難しい実験の際にサポートしていただきました。

国立天文台 水沢VLBI観測所の皆様には、VLBIバックエンドの関係で大変お世話になりました。VLBIグループで野辺山観測を担当されている特任研究員の永山匠様にはVLBI観測のため、PolariSで観測するconfigurationから接続を変更する際などに丁寧に連絡をいただきました。また、PolariSの観測の日程間近にVLBIバックエンドの調整を行っていただきました。

河野裕介准教授には、VLBIバックエンドの不具合時に親切に対応していただき、問題の解決を円滑に行うことができました。

またここにあげられなかった多くの皆様に多くの助言をいただききました。深く感謝致しております。

最後に、これまでの自分の思う道を進むことに対し、暖かく見守り、そして辛抱強く支援をしてくれた父と母に深い感謝の意を表して謝辞と致します。